Universidade do Minho
Escola de Engenharia

Ana Catarina da Silva Guise

Development of fibrous structures for brain phantoms

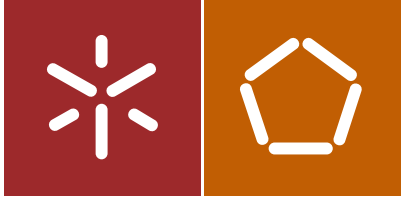
FCT Fundação para a Ciência e a Tecnologia
MINISTÉRIO DA CIÊNCIA, TECNOLOGIA E ENSINO SUPERIOR

POPH QUALIFICAR É CRESCER.
QREN QUADRO DE REFERÊNCIA ESTRATÉGICO NACIONAL PORTUGAL 2007.2013
GOVERNO DA REPÚBLICA PORTUGUESA
UNIÃO EUROPEIA Fundo Social Europeu

Ana Catarina da Silva Guise Development of fibrous structures for brain phantoms

UMinho | 2017

fevereiro de 2017



Universidade do Minho
Escola de Engenharia

Ana Catarina da Silva Guise

Development of fibrous structures for brain phantoms

Tese de Doutoramento
Programa Doutoral em Engenharia Biomédica

Trabalho efectuado sob a orientação de
Professor Doutor Raul Manuel Esteves Sousa Fangueiro
Professor Doutor João Miguel de Amorim Novais da Costa Nóbrega
Professor Doutor Walter Schneider

fevereiro de 2017

STATEMENT OF INTEGRITY

I hereby declare having conducted my thesis with integrity. I confirm that I have not used plagiarism or any form of falsification of results in the process of the thesis elaboration.

I further declare that I have fully acknowledged the Code of Ethical Conduct of the University of Minho.

University of Minho, February 2017

Full name: Ana Catarina da Silva Guise

Signature: Ana Catarina da Silva Guise

Ao meu anjo da guarda: a minha avó

Aos meus pais

À minha irmã

Ao Marco

Acknowledgements / Agradecimentos

A conclusão desta etapa só foi possível graças a diversos contributos de pessoas e instituições a quem gostaria de deixar o meu sincero agradecimento:

Em primeiro lugar, agradeço ao meu orientador, Professor Raul Fangueiro, por me ter desafiado a concorrer a uma bolsa de doutoramento com este tema tão inovador. Agradeço, igualmente, o apoio dado ao longo destes 4 anos de doutoramento e ao longo dos 6 anos de trabalho em conjunto.

Ao meu co-orientador, Professor Miguel Nóbrega pela disponibilidade que sempre mostrou ao longo destes 4 anos.

Now, in english, I would like to thank to my co-supervisor Professor Walter Schneider for his enthusiasm during all the PhD. Also, I would like to thank to all members of Schneider Lab for having received me so well in Pittsburgh during 3 months. Finally, I would like to thank to Psychology Software Tools which opened the door for me without any restriction.

À tia Nara e ao Paul por terem sido como pais nos 3 meses que estive nos Estados Unidos.

À equipa Fibrenamics, não só por estes 4 anos, mas pelos 6 anos que já faço parte. À Juliana e ao Fernando pela imprescindível ajuda, disponibilidade e por todos os ensinamentos que me passaram. Igualmente, agradeço à Margarida pela sua preciosa ajuda nestes últimos meses de trabalho. E como não poderia deixar de ser, um obrigada especial à Rita ... por tudo! Obrigada Ritinha.

À Sílvia pelo incentivo tão característico dela, principalmente, quando eu me inscrevi na pós graduação. Obrigada Silvinha.

Aos técnicos Joaquim Jorge, Maurício, João Paulo, Anabela pela disponibilidade que demonstraram sempre que eu lhes bati à porta.

Ao professor João Paulo Borges pela ajuda durante as semanas que passei na Faculdade de Ciências e Tecnologia da Universidade Nova de Lisboa.

Às empresas: Multicol, especialmente Drº António, Drª Luz, Vítor e Dona Marília; Bordados M. A. & Filhos, Lda, em especial à Dona Armanda; Endutex - Revestimentos Têxteis S.A.; e, Mundo Têxtil – Indústrias Têxteis S.A, em especial à Drª Marisa. Also, thanks to Nylstar company.

Por fim, agradeço, também, à Fundação para a Ciência e Tecnologia pelo financiamento da bolsa individual de doutoramento SFRH / BD / 90324 / 2012.

A todos, muito obrigada! Thank you all!



Abstract

In Europe, 75,000 people die each year from traumatic brain injuries, mainly caused by traffic accidents. In the United States, 1.7 million/year cases of traumatic brain injuries occur and only in 5-30% of these cases the damages are detected by current imaging techniques, as computed tomography and magnetic resonance imaging. High-Definition Fiber Tractography is a novel modality of magnetic resonance imaging, based on diffusion technology of water molecules through brain tissue, which provides highly detailed images of the brain. This imaging technique allows detecting the exact local of damage in an axon as X-Ray allows identifying the local where a bone is broken.

The inexistence of a phantom that rigorously mimics the human brain hinders the possibility of testing, calibrating and validating these medical imaging techniques. Most research in this area suffers from a huge gap in key points, such as the size limit and geometry used to mimic the human brain axons. The aim of this PhD project was to assess the application of synthetic fibrous materials, which mimic human axons of brain white matter in terms of geometry, on the development of an anisotropic brain phantom, as similar as possible to the human brain white matter, which could be employed on the validation and calibration of brain diffusion imaging, based on magnetic resonance imaging, including the novel neuroimaging technique: the High-Definition Fiber Tractography imaging.

To this end, hollow multifilament yarns made of polypropylene and polyamide and coaxial polycaprolactone fibers, produced by electrospinning, were chosen for the undertaken studies, due to its tube-like geometry, with dimensions close to the human axons. To obtain the desired dimensions, comparable to human axons, three different technologies were tested: polypropylene and polyamide hollow multifilament commercial yarns obtained by melt spinning technique; post-production stretching of the previously mentioned hollow yarns using a laboratorial filament extrusion line; and, production of coaxial polycaprolactone fibers by electrospinning. Characterization of the hollow multifilament yarns regarding physical, chemical and mechanical properties was performed. In order to achieve the different configuration that human axons present in white matter of the human brain, fibrous structures were developed based on polypropylene hollow multifilament yarns due to some of their interesting properties comparatively to polyamide. Braided structures, narrow fabrics and embroidery technology showed to be a good choice to mimic the parallel configuration of the human axons, crossing

zones and complex patterns existing in the white matter. The different types of water motion that occur in the axons of human white matter were verified in the fibrous materials by fluorescence microscopy. At the end, the yarns were scanned in magnetic resonance equipment and analyzed using High-Definition Fiber Tractography.

Polypropylene hollow multifilament yarns showed to be an outstanding option to mimic white matter human axons in the development of anisotropic brain phantoms to validate and make the quality control of the neuroimaging techniques. Furthermore, High-Definition Fiber Tractography presented highly detailed images of the polypropylene yarns. The results presented in this work are novel and promising since there is no literature that focuses on the study of material properties that mimic properly the human axons of brain white matter.

These works have been performed in the framework of the project: “High-Definition MRI Fiber Tracking and Computational Phantom Quality Measurement and Assessment” coordinated by Walter Schneider, at University of Pittsburgh, USA, whose research was devoted to the development of the first phantom for the validation of the novel High-Definition Fiber Tractography imaging.

Resumo

Na Europa, 75.000 pessoas morrem, anualmente, devido a traumatismos cranioencefálicos, principalmente, causados por acidentes rodoviários. Nos Estados Unidos, ocorrem, por ano, 1.7 milhões de casos e, apenas, em 5 a 30% destes casos, os danos são detetados pelas técnicas de neuroimagem mais utilizadas, como a tomografia computorizada e a ressonância magnética. *High-Definition Fiber Tractography* (Tractografia de fibras em alta definição) é uma nova modalidade de imagem por ressonância magnética, baseada na difusão das moléculas de água através do tecido cerebral, que fornece imagens altamente detalhadas do cérebro. Esta ferramenta de imagem permite detetar o local exato de um dano num axónio tal como o Raio-X identifica o local onde um osso está fraturado.

A inexistência de um modelo adequadamente aproximado ao cérebro humano impede a possibilidade de testar, calibrar e validar estas técnicas de imagem médica. A maioria das pesquisas nesta área sofre uma enorme lacuna em pontos-chave, como o limite de tamanho e geometria utilizada para imitar os axónios do cérebro humano. O objetivo deste projeto foi avaliar a aplicação de materiais fibrosos sintéticos, que imitam os axónios humanos da matéria branca do cérebro em termos de geometria, para o desenvolvimento de um fantoma anisotrópico, o mais semelhante possível à matéria branca do Homem, que poderá ser utilizado na validação e calibração de técnicas de neuroimagem baseadas na difusão das moléculas de água no cérebro, com base em imagens de ressonância magnética, incluindo a nova técnica de neuroimagem: *High-Definition Fiber Tractography.*

Para tal, foram utilizados fios multifilamento ocos de polipropileno e poliamida e fibras coaxiais de policaprolactona, produzidas por electrospinning, devido à sua geometria tubular, com dimensões próximas aos axónios. Para obter as dimensões desejadas, comparáveis aos axónios humanos, três tecnologias foram testadas: fios multifilamento ocos comerciais de polipropileno e poliamida obtidos por melt spinning; estiramento pós-produção dos fios ocos mencionados anteriormente, utilizando uma linha laboratorial de extrusão de filamentos; e, a produção de fibras de policaprolactona coaxiais através de electrospinning. Os fios multifilamento ocos foram caracterizados a nível físico, químico e mecânico. Com o objetivo de reproduzir as diferentes configurações dos axónios na matéria branca, foram desenvolvidas estruturas fibrosas utilizando os fios multifilamento ocos de polipropileno, uma vez que este material apresentou propriedades mais adequadas, comparativamente às da poliamida. Estruturas entrançadas, tecidos estreitos e

bordados mostraram ser uma boa escolha para mimetizar a configuração paralela e zonas de cruzamentos de axónios, assim como, certos padrões complexos que existem na matéria branca. Os diferentes tipos de movimento da água que ocorrem nos axónios humanos foram verificados nos materiais fibrosos, através de microscopia de fluorescência. No final, os filamentos foram mapeados, através de ressonância magnética, e, os dados foram, posteriormente, analisados através de *High-Definition Fiber Tractography*.

Os filamentos ocos de polipropileno mostraram ser uma excelente opção para mimetizar os axónios humanos da matéria branca, na materialização de modelos cerebrais anisotrópicos para validação e controlo de qualidade das técnicas de neuroimagem. Igualmente, a nova modalidade de imagem *High-Definition Fiber Tractography* apresentou imagens altamente detalhadas dos fios de polipropileno. Os resultados apresentados neste trabalho são novos e promissores, pois não há literatura focada no estudo das propriedades dos materiais que mimetizam, adequadamente, os axónios humanos da matéria branca do cérebro.

Estes trabalhos foram realizados no âmbito do projeto "*High-Definition MRI Fiber Tracking and Computational Phantom Quality Measurement and Assessment*", coordenado pelo professor Walter Schneider, da Universidade de Pittsburgh, EUA, cuja pesquisa foi dedicada ao desenvolvimento do primeiro fantoma para a validação da nova modalidade de neuroimagem *High-Definition Fiber Tractography*.

Contents

Acknowledgements / Agradecimentos iii

Abstract v

Resumo vii

Contents ix

List of Figures xiii

List of Tables xix

Nomenclature and acronyms xxi

Structure of the thesis xxiii

CHAPTER I: Introduction 1

1. Brain imaging techniques by diffusion: High-Definition Fiber Tractography 3

1.1. Diffusion in brain white matter 5

1.2. Diffusion tensor imaging 8

2. Validation and quality control of brain imaging techniques: brain phantoms 10

2.1. Isotropic phantoms 11

2.2. Anisotropic phantoms 12

3. Synthetic fibrous materials 17

3.1. Melt spinning 19

3.2. Molecular orientation 21

3.3. Hollow fibers 23

4. Final Remarks 24

CHAPTER II: Fibrous materials for development of brain phantom 25

1. Introduction 27

2. Materials and methods 31

2.1. Hollow multifilament yarns 31

2.1.1. Characterization of hollow multifilament yarns 32

2.2. Post-production stretching 34
2.3. Electrospun fibrous materials 35
3. Results and discussion 36
3.1. Characterization of hollow yarns 36
3.2. Characterization of electrospun fibers 42
4. Conclusions 44
CHAPTER III: Characterization of the fibrous materials 47
1. Introduction 49
2. Materials and methods 51
2.1. Chemical analysis 51
2.1.1. Structure: FTIR and XRD 52
2.1.2. Crystallinity: DSC and XRD 52
2.2. Contact angle 53
2.3. Moisture content 53
2.4. Friction coefficient 53
2.5. Tensile tests 53
2.6. Vertical wicking 54
3. Results and discussion 54
3.1. Chemical analysis 54
3.1.1. Structure: FTIR and XRD 54
3.1.2. Crystallinity: DSC and XRD 56
3.2. Contact angle 58
3.3. Moisture content 59
3.4. Friction coefficient 61
3.5. Tensile properties 62
3.6. Vertical wicking 67

4. Conclusions 73

CHAPTER IV: Development and characterization of fibrous structures 75

1. Introduction 77

2. Materials and methods 82

2.1. Braided structures 82

2.1.1. Braiding conditions 82

2.1.2. Characterization of the braided structures: structural properties 84

2.1.3. Tensile test 85

2.1.4. Vertical wicking 85

2.2. Narrow fabrics 85

2.2.1. Characterization of the narrow fabrics: structural properties 87

2.2.2. Tensile tests 88

2.2.3. Vertical wicking 88

2.3. Embroidered structures 88

3. Results and discussion 90

3.1. Braided structures 90

3.1.1. Structural properties 90

3.1.2. Tensile properties 92

3.1.3. Vertical wicking 94

3.2. Narrow fabrics 95

3.2.1. Structural properties 96

3.2.2. Tensile properties 96

3.2.3. Vertical wicking 98

3.3. Embroidered structures 100

4. Conclusions 101

CHAPTER V: Development and validation of the brain phantom 103

1. Introduction 105

2. Material and methods 106

2.1. Water diffusion in hollow multifilament yarns 106

2.2. Phantom development 107

2.3. HDFT phantom validation 109

3. Results and discussion 109

3.1. Water diffusion in hollow multifilament yarns 109

3.2. HDFT phantom validation 110

4. Conclusions 112

CHAPTER VI: Conclusions and work perspectives 113

1. Final conclusions 115

2. Work perspectives 117

References 119

Publications and Communications 139

List of Figures

Figure 1: Corona radiata fibers in a healthy control mapped using Diffusion Tensor Imaging and High-Definition Fiber Tractography [6]. It should be noted colored map of these diffusion neuroimaging modalities according orientation: green, anterior-posterior; red, lateral-medial; and, blue, inferior-superior. Other colors indicate mixed orientation of the fibers. 4
Figure 2: Brain structure (adapted from [14]). 5
Figure 3: Neuron structure: a) neuron where axon is subdivided b) neuron that unnerves a muscle cell (adapted from [14]). 6
Figure 4: Types of diffusion processes in white matter: (1) hindered diffusion; (2) restricted diffusion; (3) exchange between intracellular and extracellular space. 7
Figure 5: Free, hindered and restricted diffusion. 7
Figure 6: Diffusion can take place more easily in parallel to the white matter bundles than perpendicular to it. 8
Figure 7: Three diffusion ellipsoids represent the diffusion profile of 3 different structures: (a) isotropic diffusion ellipsoid; (b) anisotropic diffusion ellipsoid; (c) anisotropic diffusion ellipsoid, representing a white matter tract parallel to the x-axis. The axes represent the x- (left-right, red), y- (posterior-anterior, green), and z-(inferior-superior, blue) directions (adapted from [24]). 8
Figure 8: True diffusion and DT model of parallel and crossing axons. 9
Figure 9: Isotropic phantom: (a) vials of PVP in aqueous solution. The central vial is pure water, while darker solutions indicated higher concentrations of the polymer; (b) assembled first prototype phantom, with a diameter of 194 mm; (c) software-generated ADC map of the phantom [46]. 12
Figure 10: Cross-sectional photograph of the capillary arrays used by Yanasak and Allison [67]. The hash mark in the insert is 0.2 mm in length. 15
Figure 11: (a) Microscopic view of a rayon textile filament and (b) top view of the phantom [73]. 16
Figure 12: Different types of fiber cross-sections. 19
Figure 13: Scheme of melt spining process. 20
Figure 14: Orientation and order of fiber polymer system: (a) non-orientated non-crystalline; (b) non-orientated but sections ordered; (c) orientated and crystalline. 22
Figure 15: Cross-section of polypropylene hollow yarn. 23
Figure 16: Chemical reactions to obtain polyamide 6 and polyamide 6.6. 27

Figure 17: Polyethylene terephthalate reaction. 28
Figure 18: Propylene monomers and polypropylene chain. 28
Figure 19: Hollow polyester staple yarn. 29
Figure 20: Electrospinning apparatus. 30
Figure 21: Schematic representation of the spinneret used to produce polypropylene hollow multifilament yarns. 32
Figure 22: Cutting tool used to obtain the yarns cross-section for further visualization on SEM: (a) photograph of the cutting tool and (b) the same tool prepared inside SEM equipment. Red circle highlighted the hollow filaments already cut. 33
Figure 23: Prototype downstream equipment of a filament extrusion line. 34
Figure 24: Electrospinning apparatus used to produce aligned hollow fibers. 36
Figure 25: Cross-sectional of PP 1 filaments before (a) and after (b) post-production stretching. 37
Figure 26: Cross-sectional of PP 2 filaments before (a) and after (b) post-production stretching. 37
Figure 27: Cross-sectional of PP 3 filaments before (a) and after (b) post-production stretching. 37
Figure 28: Cross-sectional of PP 4 filaments before (a) and after (b) post-production stretching. 38
Figure 29: Cross-sectional of PP 5 filaments before (a) and after (b) post-production stretching. 38
Figure 30: Hollowness PP values before and after post-production stretching. 40
Figure 31: (a) Axon and respective myelin sheath (adapted by [137]) and (b) PP hollow filament axonal diameter: axonal diameter (ad) and myelin thickness (my). 41
Figure 32: Cross-sections of PA filaments. 41
Figure 33: SEM micrograph of longitudinal section of (a) human hair and (b) PP hollow filament, with respective diameters. Please note the different scales. 42
Figure 34: SEM images of (a) and (b) aligned electrospun fibers of PCL/PEO solution and respective cross-sections (c) and (d). 43
Figure 35: Schematic of experimental set up for capillary rise. 54
Figure 36: (a) FTIR spectra for PP 1; and (b) FTIR spectra for PP 5. 55
Figure 37: XRD diffraction pattern of PP 1. 55
Figure 38: (a) FTIR spectra of PA; and (b) XRD diffraction pattern of PA. 56
Figure 39: DSC curves: (a) PP 1, (b) PP 1S and (c) PA. 58
Figure 40: (a) Droplet on PP 1 filament surface; (b) droplet on PA filament surfaces. 59
Figure 41: Tenacity-extension curves in dry conditions at room temperature of PP yarns (a) before and (b) after post-production stretching; at human body temperature of PP yarns (c) before and

(d) after post-production stretching. Please note for different scales due different reached values. 64
Figure 42: Tenacity-extension curves in wet conditions at room temperature of PP yarns (a) before and (b) after post-production stretching; at human body temperature of PP yarns (c) before and (d) after post-production stretching. Please note for different scales due different reached values. 65
Figure 43: Characteristic points of tenacity-extension curve. 65
Figure 44: Tenacity-extension curves in dry and wet condition at room temperature (RT) and human body temperature (HB) of PA yarns. 67
Figure 45: Wicking height at room temperature of PP yarns (a) before and (b) after post-production stretching; at human body temperature of PP yarns (c) before and (d) after post-production stretching. 68
Figure 46: Wicking height at room temperature (RT) and human body temperature (HB) to PA hollow multifilament yarns. 69
Figure 47: Wicking height and respective linear fit curves of PP yarns at room temperature of (a) before and (b) after post-production stretching; at human body temperature (c) before and (d) after post-production stretching. 70
Figure 48: Wicking height and respective linear fit curves at room temperature (RT) and human body (HB) temperature to PA hollow multifilament yarns. 70
Figure 49: Slope values versus yarns: (a) PP yarns before post-production stretching; (b) PP yarns after post-production stretching; and (c) PA yarns. 72
Figure 50: Braiding scheme (left side image) and spindles representation (right side image). Odd spindles rotate in clockwise and even spindles rotate in counterclockwise (adapted from [198]). 78
Figure 51: Core reinforced braided structure (adapted from [199]) 78
Figure 52: Braided structure. 79
Figure 53: Weft and warp representation. 80
Figure 54: Tailored fiber placement [206]. 81
Figure 55: Schematic diagram of produced braided structures: (a) braids with axially reinforcing PP hollow yarns; (b) braids with axially reinforcing braids; (c) orientation of yarns/braids in the core of braided structures. 83
Figure 56: Scheme showing the production of different types of braided structures. 83

Figure 57: Braiding process of braided structures with PP yarns in the core: (a) vertical braiding machine TRENZ®; (b) braided structure; (c) PP hollow yarns (core of the braided structure). 84
Figure 58: Narrow weaving Müller® machine model NHJM2 53. 86
Figure 59: Weave patterns: (a) plain; (b) satin; (c) jacquard. Weave patterns have a double weft insertion. 87
Figure 60: Scheme showing the production of different types of narrow fabrics. 87
Figure 61: (a) Human visual tracts obtained by HDFT and (b) visual system of the human brain (Images provided by the Walt Schneider Lab, USA). 89
Figure 62: Multi-head automatic embroidery machine SFW/TA-WL 910-120 (Image provided by Bordados M.A. & Filhos Ltd., Portugal). 89
Figure 63: Examples of the braided structures produced: (a) 10 braids in the core -1- and 100 yarns in the core -2-; (b) 10 braids in the core (magnification); (c) 100 yarns in the core (magnification). 90
Figure 64: (a) Comparation between measured and predicted braiding angles: (a) braided structures with axially reinforcing braids; (b) braided structures with axially reinforcing yarns. 91
Figure 65: Force – extension curves for: (a) braided structures with axially reinforcing braids; (b) braided structures with axially reinforcing yarns (Please note the different graphic scales). 92
Figure 66: Force-extension curve of a core reinforced braided structure. 93
Figure 67: Relationship between breaking force and (a) number of axial braids and (b) number of axial yarns. 94
Figure 68: Wicking height of: (a) braided structures with axially reinforcing braids; (b) braided structures with axially reinforcing yarns. 94
Figure 69: Narrow fabrics produced with PP 1 (warp) and PES 2 (weft): (a) plain; (b) satin; (c) jacquard. Scale bars represent 1 cm. 95
Figure 70: Load – extension curves of: (a) plain; (b) satin; (c) jacquard. 97
Figure 71: Breaking force of narrow fabrics. 98
Figure 72: Wicking height of: (a) plain; (b) satin; (c) jacquard. 99
Figure 73: (a) Top view of optic chiasm layout; (b) embroidered textile coating mimicking the optic chiasm; (c) magnification of embroidered optic chiasm. Scale bars represent 1 cm. 100
Figure 74: Filling process apparatus: (a) filling hollow yarns with fluorescent dye (Rhodamine B R6626); (b) vacuum pump; (c) detail of PP hollow multifilament yarns. 106

Figure 75: Schematic representation of the developed brain phantom (a) constituents of brain phantom; (b) frames with different yarn density areas where yarns are oriented to 0°; (c) frame with yarns assembled with different crossing angles (Images provided by Walt Schneider Lab). 107
Figure 76: Filling process of the PP hollow multifilament yarns. Red circle highlighted the frame with yarns..... 108
Figure 77: (a) Brain phantom with different areas – (1) crossing yarns and (2) fiber density; and (b) brain phantom inside of a head coil prepared to be scanned in a MRI equipment (Images provided by Walt Schneider Lab). 108
Figure 78: Fluorescence images of PP yarns cross-sections (A, B, C, E). D) represents the model of water motion in the human axons already presented in Chapter I. In C) arrows indicate water marked with fluorescent dye inside filaments (restricted diffusion) that can be easily tracked on the overlap channel. In E) it is possible to observe fluorescent dye between filaments, representing hindered diffusion. Scale bar represents 100 μm. 109
Figure 79: Fiber tracking: yarn density areas (a); yarn crossing areas (b); and, yarns without water inside of the hollow part (c). Colors on the map according to their orientation: red, lateral-medial (x – axis); green, anterior-posterior (y - axis); blue, inferior-superior (z - axis). Other colors indicate mixed orientation of the yarns (Images provided by Walt Schneider Lab). 110

List of Tables

Table 1: Properties of polyamide, polyester and polypropylene fibers [95,123] 29
Table 2: Linear mass, outer and inner diameters, yarn diameter and hollowness of PP yarns ... 39
Table 3: Linear mass, outer and inner diameters, yarn diameter and hollowness of PA yarns ... 41
Table 4: Outer, inner diameter and hollowness of electrospun PCL/PEO fibers 43
Table 5: Cristallinity results in percentage according DSC and XRD analysis 57
Table 6: PP and PA hollow multifilament yarns moisture contents 60
Table 7: Friction coefficient of PP and PA hollow multifilament yarns 61
Table 8: Tensile properties of PP yarns in dry and wet conditions at room temperature 62
Table 9: Tensile properties of PP yarns in dry and wet conditions at human body temperature . 63
Table 10: Tensile properties of PA yarns in dry and wet conditions at room and human body (HB) temperature 67
Table 11: Regression values and correlation coefficient of the PP and PA yarns at room temperature (RT) and human body (HB) temperature 71
Table 12: Structural properties of braided structures according with the core 90
Table 13: Breaking force and extension at failure for different braided structures 92
Table 14: Regression values and correlation coefficient of the braided structures 95
Table 15: Structural properties of narrow fabrics 96
Table 16: Tensile results of the different narrow fabrics 97
Table 17: Regression values and correlation coefficient of the narrow fabrics 100
Table 18: Fractional anisotropy and mean diffusivity values for different five density zones and for fiber crossing 111

Nomenclature and acronyms

AD - Axial diffusivity

ADC - Apparent diffusion coefficient

CT - Computed tomography

DC - Direct current

DMF - N,Ndimethyl-formamide

DSC - Differential scanning calorimetry

DT - Diffusion tensor

DTI - Diffusion tensor imaging

ESEM - Environmental scanning electron microscope

FA - Fractional anisotropy

FTIR - Fourier transform infrared

HB - Human body (temperature)

HDFT – High-Definition Fiber Tractography

MD - Mean diffusivity

MRE - Magnetic resonance elastography

MRI - Magnetic resonance imaging

PA - Polyamide

PCL - Polycaprolactone

PEO - Polyethylene oxide

PES – Polyester

PET - Polyethylene terephthalate

PP - Polypropylene

PTFE - Polytetrafluoroethylene

PVC - Polyvinyl chloride

PVP - Polyvinylpyrrolidone

QC - Quality control

RD - Radial diffusivity

RT - Room temperature

SEM - Scanning electronic microscopy

TBI - Traumatic brain injury

XRD - X-Ray diffraction

L - Liquid front position or wicking length

γ - Surface tension of the liquid

η - Viscosity of the liquid

θ_a- Apparent contact angle

R - Effective hydraulic radius of the interfilament pores

t – Time

$\Delta \mathrm{Hm}$ - Melting enthalpy of the polymer

$\Delta \mathrm{H^{\circ}m}$ - Melting enthalpy of 100 % crystalline polymer

α - Braiding angle

W - Angular speed of bobbins

Rc- Core radius

V - Take-up speed

K_x – Warp/weft cover factor

K_1 – Warp cover factor

K_2 – Weft cover factor

Structure of the thesis

This thesis is divided in 6 chapters.

Chapter I encloses an introduction about the medical imaging techniques and current problems in this area. There is a need to continue studying and developing new modalities and High-Definition Fiber Tractography appears in that sense. Being a new brain imaging modality, there is the need to perform validation and quality control, procedures extremely important for clinical diagnostics. Brain phantoms that until now have been developed with the aim to approximate to the human brain, still limit the possibility of testing, calibrating and validating medical imaging techniques. Most research in this area suffers from a huge gap in key points such as the size limit reproduced of the brain fibers and the quick and easy reproducibility of phantoms. To provide a clear overview of the state for the art in this area, the first chapter describes current imaging techniques and its main limitations, explains new brain modality named High-Definition Fiber Tractography and, finally, the importance of fibrous materials in anisotropic brain phantoms construction and the need to develop a model that better approaches the human brain behavior.

Chapter II focuses on the analyses of fibrous materials for application in anisotropic diffusion phantoms, more specifically synthetic fibers, and presents their main properties. The choice of materials and the respective inherent motivation are referenced as well. Also, the post-production stretching technique and electrospinning, tested to obtain a range of yarn diameters, are explained in this chapter.

Chapter III includes detailed characterization of fibrous materials chosen for this purpose regarding chemical, physical and mechanical properties.

Chapter IV concerns to the development of textile structures to simulate specific human brain areas as well as to create a controlled development of the phantom and thus its reproducibility. Structure characterization tests as well as strength tests and wicking are presented in this chapter.

Chapter V presents the validation of fibrous materials chosen and studied by High-Definition Fiber Tractography. Moreover, the brain phantom development is explained.

Chapter VI provides the major conclusions of the thesis and presents proposals for future work.

CHAPTER I: Introduction

Brain imaging techniques are becoming an increasingly important tool in both research and clinical care. A range of noninvasive imaging technologies now provide unprecedented sensitivity to visualization of brain structure and function, ranging from the level of individual molecules to the whole brain. In order to assure that what it is seen with these imaging techniques correspond to reality, to further improve their quality a validation process is essential, followed by quality control procedures. This can be done using phantoms made by materials being able to mimic human brain, such as fibers. This first chapter presents the state of the art of the main topics covered by this research work.

1. Brain imaging techniques by diffusion: High-Definition Fiber Tractography

Traumatic brain injury (TBI) constitutes a major health and socioeconomic problem throughout the world. Although there was a decrease in TBI numbers in last decade due to traffic safety policies, they are still high and society is unaware of the TBIs impact. Due to this lack of knowledge and to the fact that the problems resulting are often not visible, TBI is usually designated by the "silent epidemic" [1]. It is estimated that in the European Union, approximately, 7.7 million people who have experienced a TBI have disabilities [2]. The number of cases concerning the incidence and prevalence of TBI in Portugal is difficult to estimate, especially due to issues inherent to the way the health system is organized. In the United States, 1.7 million/year cases occur and only in 5-30% of these cases the damages are detected by current imaging techniques, such as computed tomography (CT), magnetic resonance imaging (MRI) and diffusion tensor imaging (DTI) [3].

TBIs are, usually, detected and analyzed using CT and MRI. However, it should be noted that injuries detected both by MRI and CT are, typically, areas of hemorrhage that must be large enough to be detected. Taking into account that forces that brain is subjected to promote a TBI, are high enough to tear blood vessels, adjacent axons will be also torn, since blood vessels diameter is much larger than the axon diameters. In the cases that there is not bleeding, both CT as MRI only detect an abnormality if a large quantity of axons were injured, thus they are useful just for the diagnostic of severe cases [4,5].

MRI has shown a link to methods of diffusion images, which have an higher sensitivity to white matter integrity [6]. Diffusion MRI, also known as DTI, is an MRI technology which allows the non-invasively mapping of the molecules diffusion process, mainly water, in biological tissue.

Over the past decade, DTI has been widely used in brain traumatic injuries diagnostics, due to its higher resolution when compared to CT and MRI. DTI uses the motion of water molecules in tissue to generate contrast in MR images. Introduction of this technique represented a major step in what concerns to the knowledge of the human brain neuroanatomy. Despite this greater level of detailed images, DTI has still some shortcomings, such as the need for a finer resolution to distinguish the white matter tracts and, in addition, tends to provide false representations of the anatomy tract [6,7]. Specially, the diffusion tensor model has been shown to be inappropriate in regions that present crossing fibers [8]. Hence an imaging technique that corrects the current technical limitations is demanded.

The High-Definition Fiber Tractography (HDFT) method was developed to solve some of the limitations existing in neuroimaging area. It is a new technique that allows visualizing directly and quantifying the degree of axons damage, predicting functional deficits due to traumatic axonal injury and loss of cortical projections. The goals of the HDFT analysis approach are to classify and quantify white matter injury in individual patients, and provide correlations between injuries and clinical consequences [9]. Figure 1 shows a tracking done to corona radiate in a healthy control mapped using DTI and HDFT.

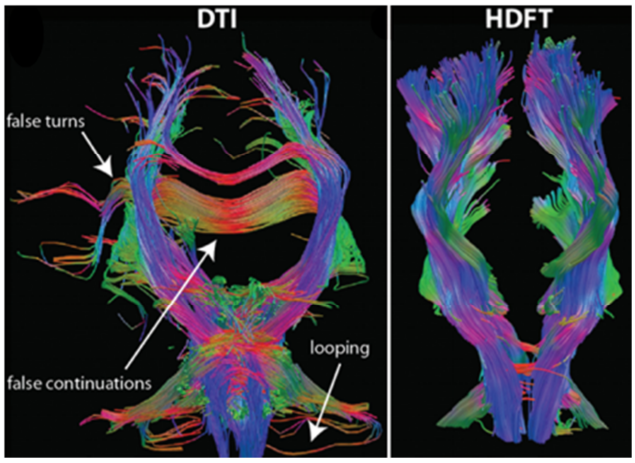


Figure 1: Corona radiata fibers in a healthy control mapped using Diffusion Tensor Imaging and High-Definition Fiber Tractography [6]. It should be noted colored map of these diffusion neuroimaging modalities according orientation: green, anterior-posterior; red, lateral-medial; and, blue, inferior-superior. Other colors indicate mixed orientation of the fibers.

It is possible to see that DTI shows connections and fiber tracks which do not correspond with real brain anatomy, including false turns (deviations from the pathway), false continuations (midline crossing), and looping (travel in random directions). On the other hand, HDFT scan does not show the same errors, being consistent with real brain anatomy [6].

HDFT has simplified accurate surgical planning and it has the ability on detection and respective treatment in brain injuries [7,9–13]. Being a useful tool for diffusion MRI, which is also based in motion of water molecules in brain, it is important to understand how occurs diffusion in brain and how it is measured.

1.1. Diffusion in brain white matter

The brain represents approximately 80% of encephalon mass and it is divided into two parts: telencephalon and diencephalon. Left and right hemispheres divide, symmetrically, the telencephalon through the interhemispheric fissure. At the bottom of this fissure is the corpus callosum that is the structure that connects the two hemispheres. The external layer that forms the hemispheres is the gray matter, known as the brain cortex and the innermost layer and most abundant is known as white matter. The cell bodies of the neurons are located in the cerebral cortex while bundles of neuronal axons, myelin-coated, are in the white matter (Figure 2).

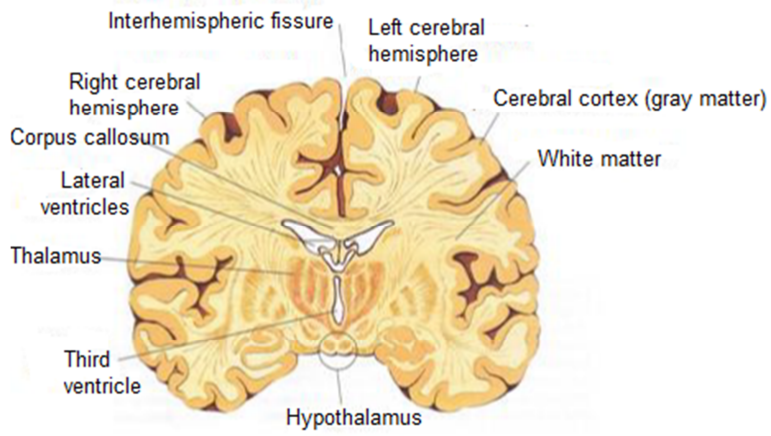


Figure 2: Brain structure (adapted from [14]).

Neurons and glial cells, also called nerve cells, are the two cell types that exist in the nervous system. The second cells (glial) play a key role for the first ones (neurons), protecting, isolating and nurturing them. In turn, the neurons have the function of generating and transmitting pulses from a zone of the body to another [15]. Figure 3 shows the typical structure of a neuron.

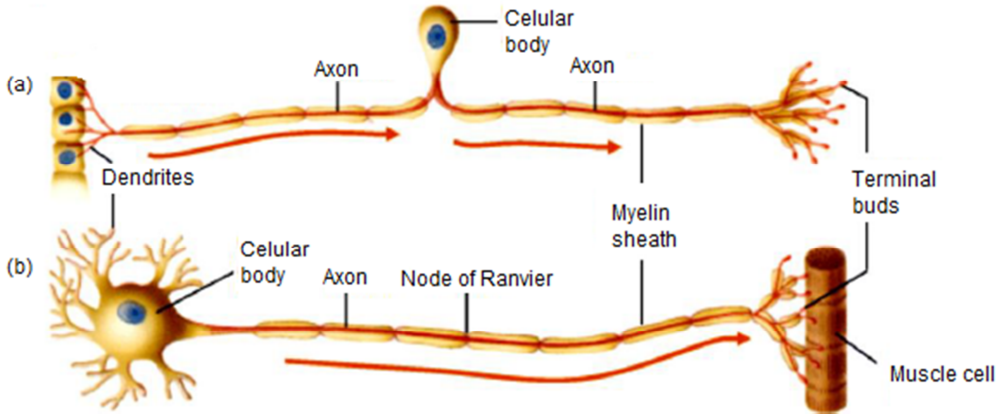


Figure 3: Neuron structure: a) neuron where axon is subdivided b) neuron that unnerves a muscle cell (adapted from [14]).

From the neuronal cell body, where the core is, there is an extension of axons and dendrites. The axons diameter, normally, ranges between less from 1 and around 25 μm [16]. Axons consist of microtubule and microfilaments and are wrapped by sheaths of myelin, produced by Schwann cells in peripheral nerve system. These sheaths of myelin are an insulating layer for the proper transmission of the electrical impulses along the axon. In some neurodegenerative diseases, as example of multiple sclerosis, demyelination occur and conduction of signals along the nerve can be impaired or lost [17]. A bundle of myelinated axons that run together is known as tract or fascicle.

Water molecules held in a container outside the body are in constant random Brownian motion, exhibiting a free diffusion motion. On the other hand, in biological tissues, the movement of water molecules is modified and limited by interactions with cell membranes and macromolecules, being restricted and this restriction of movement provides structural information of the tissue [18].

According to Assaf and Cohen [19] there are three types of diffusion processes in biological tissues: free, hindered and restricted (Figure 4).

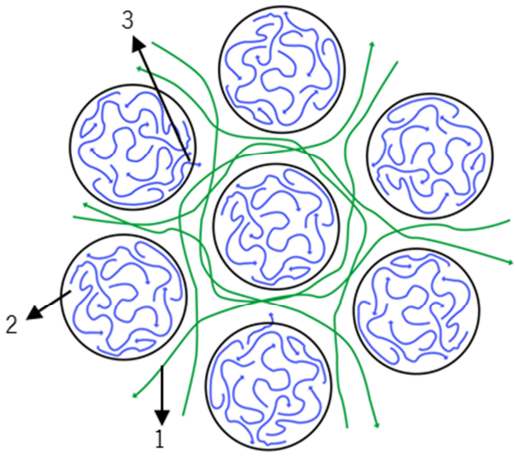


Figure 4: Types of diffusion processes in white matter: (1) hindered diffusion; (2) restricted diffusion; (3) exchange between intracellular and extracellular space.

The diffusion processes can be distinguished by the ratio between the mean displacement and diffusion time (Figure 5). In free and hindered diffusion, there is a linear relationship between displacement and the square root of the diffusion time. Regarding restricted diffusion or highly hindered diffusion (partially restricted) the dependency is nonlinear [20]

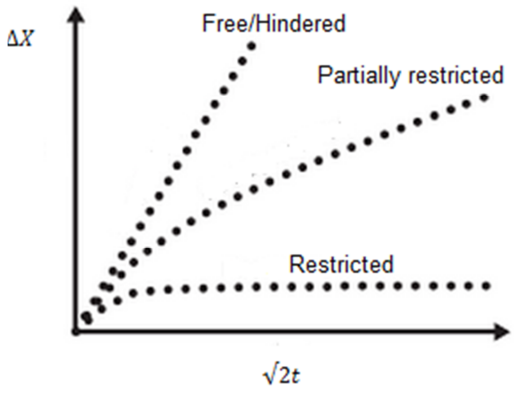


Figure 5: Free, hindered and restricted diffusion.

In general, non-neuro tissues present, approximately, isotropic water diffusion. However, cardiac and skeletal muscle, prostate and kidney tissues exhibit diffusion anisotropy, although the degree of anisotropy is not as strong as in highly ordered myelinated white matter [21].

Dense packing of axons and their inherent axonal membranes are responsible for this anisotropic water diffusion. The water diffusion is hindered significantly perpendicular to the axis of the fibers relative to the preferential parallel direction (Figure 6). The anisotropy may increase about 30% in the presence of a myelin sheath surrounding the axons [15]. This property is a measure often

used in diffusion imaging, where it is thought to reflect fiber density, axonal diameter and myelination in white matter [22].

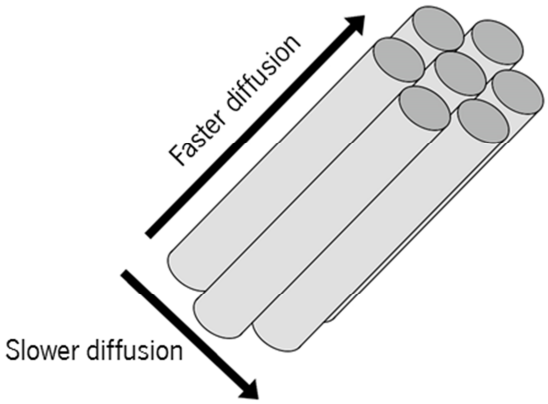


Figure 6: Diffusion can take place more easily in parallel to the white matter bundles than perpendicular to it.

1.2. Diffusion tensor imaging

The diffusion tensor (DT) expresses, quantitatively, the average displacement of water molecules in the various directions within tissue, using a Gaussian model. Technically, DT is a 3×3 symmetric, positive-definite matrix, and these matrix properties mean that it has three orthogonal (mutually perpendicular) eigenvectors and three positive eigenvalues, that give magnitude values. Diffusion tensor is best visualized as an ellipsoid (Figure 7). The long axis is parallel with the direction of greatest diffusion, known as the principal diffusion direction. The remaining vectors represent the rate of diffusion perpendicular to the principal diffusion direction [23,24].

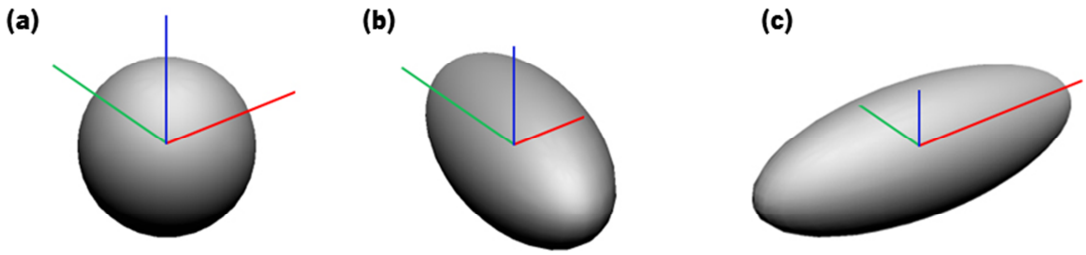


Figure 7: Three diffusion ellipsoids represent the diffusion profile of 3 different structures: (a) isotropic diffusion ellipsoid; (b) anisotropic diffusion ellipsoid; (c) anisotropic diffusion ellipsoid, representing a white matter tract parallel to the x-axis. The axes represent the x- (left-right, red), y- (posterior-anterior, green), and z-(inferior-superior, blue) directions (adapted from [24]).

Mean diffusivity (MD) and fractional anisotropy (FA) are important measures of diffusion tensor. MD is the average of the tensor's eigenvalues. Sometimes, this measure is called trace which is

the sum of eigenvalues. They are related to the amount of water in the extracellular space. MD in both gray and white matter decreases with age because increasing structure within cells impedes water diffusion. In turn, FA measures the fraction of the diffusion that is anisotropic, being a measure of the microstructural integrity [23,24]. Its value varies between 0 and 1. When is 0, diffusion is purely isotropic, indicating that there is no restriction of the movement of water molecules, i.e. water molecules environment is random, which occurs, for example, in gray matter and in case of loss of axonal diffusion. In turn, when this value is 1, diffusion is purely anisotropic, indicating that there is restriction on the movement of water molecules [25,26]. The FA values, typically, found in a health brain are around 0,7 [27]. The high FA values found in white matter is due to the structure of the axonal cell membranes and myelin sheath, which limits the diffusion of water molecules in all directions, but more significantly in the direction along the fiber tract [28] . Besides, axial and radial diffusivity (AD and RD) are important parameters. AD is the rate of diffusion in the principal diffusion direction and, on the other hand, RD the rate of diffusion perpendicular to the principal diffusion direction. Consequently, AD is related to axonal integrity and RD is related to myelin integrity [23,24].

The tensor model is only able to represent one major fiber direction in a voxel, and because of that, DTI can be misinterpreted by regions of crossing fibers, as seen before (Figure 1). A voxel that has a spherical diffusion tensor (apparently isotropic diffusion) can be a false representation of these crossing fibers (Figure 8) [23,24].

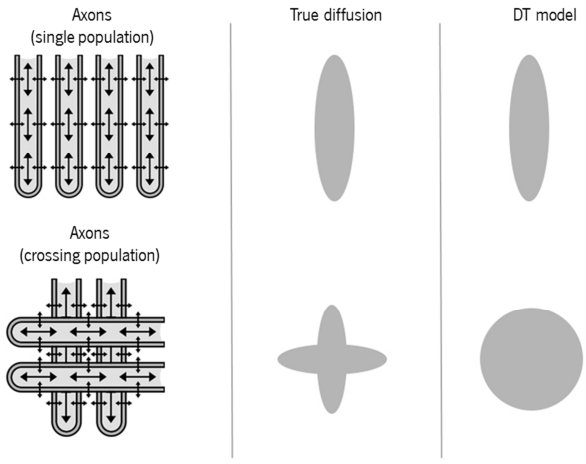


Figure 8: True diffusion and DT model of parallel and crossing axons.

Despite the development in MRI tools, validation of the imaging protocols, data acquisition, and postprocessing methods is still a challenge [29]. An important issue is to ensure the

reproducibility and accuracy of the data collected by these machines. It is crucial to know to what extent images obtained by the same equipment but with differences of months between them or taken on multiple different MRI machines are comparable [30,31]. Quality control (QC) regarding image must be evaluated periodically in order to maintain image quality.

2. Validation and quality control of brain imaging techniques: brain phantoms

For the validation of diffusion models and for the development of an accurate QC on clinical magnetic resonance scanners are required physical phantoms with a well-defined structure, composition and architectural organization [15]. Phantoms are then models that mimic human tissue and organs that have been used for characterization and calibration of diagnostic techniques. They are constructed with well-defined dimensions and internal features, thereby simplifying and standardizing the imaging environment. Phantoms are composed of tissue-mimicking materials and the majority presents a simple homogeneous internal structure. Simple or complex targets are sometimes embedded within phantoms to mimic internal structures or to serve as characterization targets [32].

Researchers have developed various methods to validate and to control these methodologies: software phantoms, physical phantoms, histological, in vitro, ex vivo, and in vivo studies [29].

There is a variety of tracking assessment technologies, including organic and numeric phantoms that provide qualitative agreement of diffusion imaging and tract structure [33]. Computational phantoms are useful for small crossings but become less precise with very small diffusion spaces and over long distances [34]. In fact, physical phantoms provide a different balance between ground truth control and realism, to that provided by computer simulations [35]. They present well-known geometry and microstructural characteristics, being imaged by a scanner with the same protocols as used in vivo. The samples take much longer to degrade comparing with in vivo tissues and can therefore be used repeatedly for quality assurance. Similarly, this type of phantom can be transferred between research or clinical facilities to assist in the validation of protocols for multisite clinical trials. In turn, histological and in vivo studies have many of the necessary biological characteristics of tissue. However, the controllability or definability of the software phantoms does not exist in histological and in vivo studies [27].

It is important that phantom allows to evaluate isotropic and anisotropic parameters found in the human brain [30]. Another significant property is the size of material used to mimic human

brain. Regarding white matter, in literature, it was found that fibers present a diameter between from less 1 around to 25 μm. Similarly, axons vary in terms of length, reaching about one meter [16,36].

2.1. Isotropic phantoms

Isotropic phantoms are developed by liquids with well-characterized diffusion coefficients to assess MD estimation [37]. Several liquids have been proposed for isotropic diffusion phantoms, as water, viscous aqueous solutions and alkanes [30].

Water is used, for example, to investigate the noise immunity characteristics of diffusion parameters and to calibrate and correct for eddy current induced artifacts in diffusion MRI [38–40]. One of the problems of the water is its high diffusion coefficient at room temperature (2.0 x 10^{-9} m^2/s) compared to the diffusion coefficient of a normal brain, between 0.3 x 10^{-9} m^2/s and 1.0 x 10^{-9} m^2/s [41]. However, this problem can be resolved by using iced water in phantoms. This type of phantoms has been vastly employed due its simple process of construction with cheap, safe and readily available materials. A disadvantage of this type of phantoms is in the storage because, in general, regular freezers are too cold and refrigerators are too warm. The ideal option, before every scan, is to prepare a water ice mix [30,42].

About viscous aqueous solutions, sucrose and agar gel have been used to develop phantoms with the aim to simulate the diffusion and contrast differences between normal gray matter and areas of acute ischemia. Sucrose solution presents a diffusion coefficient similar to that of water at low concentrations but at high concentrations MD value are similar to those found in the brain. In this case, it is necessary to control the solution temperature and when this reaches a stable value the scan can be done. Sucrose has an advantage to be a safe material and it is easily found in appropriate chemical suppliers [30].

On the other hand, alkanes have been proposed as suitable materials for use in isotropic test objects due its desirable properties that promote a good MD test liquid and any preparation is necessary to use the alkanes. Regarding cyclic alkanes, cyclohexane and cycloheptane, with a low molecular weight, have a suitable MD. However, both are not the most appropriate liquids for studying in large quantities on a clinical MRI scanner because they exhibit a high flammability and they are volatile liquids. In turn, linear n-alkanes, like decane and dodecane, are less

flammable comparing with cyclic alkanes and, at room temperature, they present a range of MD values that cover the values found in the brain [43].

Polyvinylpyrrolidone (PVP) water solutions were used to develop isotropic phantoms due to alkanes limitations related to flammability and potential toxicity. PVP showed to be a good candidate because, besides its non-toxic, it is a material easy to manufacture and cost-effective [44,45]. An example of an isotropic phantom developed by scientists at the National Institute of Standards and Technology in collaboration with the National Cancer Institute and the Radiological Society of North America is shown in Figure 9.

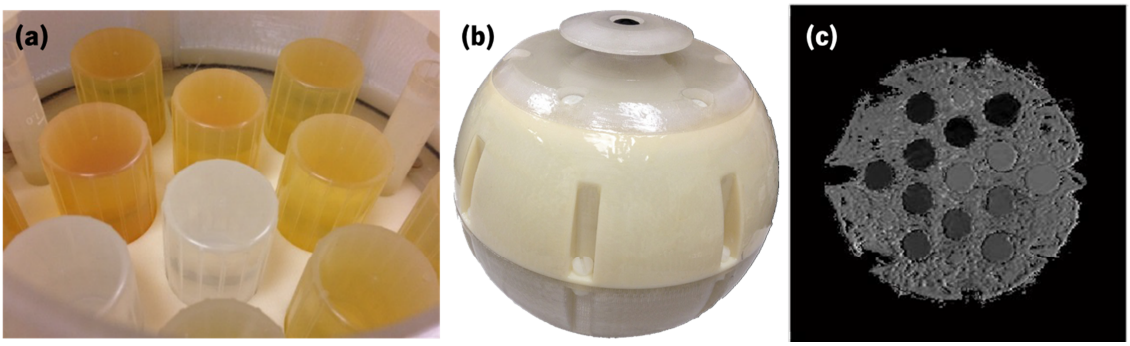


Figure 9: Isotropic phantom: (a) vials of PVP in aqueous solution. The central vial is pure water, while darker solutions indicated higher concentrations of the polymer; (b) assembled first prototype phantom, with a diameter of 194 mm; (c) software-generated ADC map of the phantom [46].

The isotropic phantom is based on different concentrations of PVP dissolved in water, from 10% to 50%, each in a separate vial. The vials are mounted within a spherical plastic shell (Figure 9 (a)). In Figure 9 (b) is possible to see the first prototype phantom and the software-generated ADC map of the phantom is shown in Figure 9 (c), where it is possible to see different tones of gray, which indicate different apparent diffusion coefficients. Higher concentrations of PVP result in lower ADC values [46].

2.2. Anisotropic phantoms

Anisotropic hardware diffusion phantoms, biological and synthetic phantoms are used for the validation of diffusion MRI. This type of phantom is important to analyze the variability, in terms of fiber orientation and anisotropy, of different MR-scanners and to evaluate quantitatively measured diffusion parameters expressing anisotropy.

Regarding biological phantoms, they can be divided in phantoms based in plants and phantoms based in biological tissue.

An example of a plant used in diffusion process since that presents isotropic diffusion in the parenchyma and anisotropic water diffusion in the vascular bundles is monocotyledon plant. Neeman *et al.* [47] used the phloem system of celery (*Apium graveolens*) to demonstrate free water isotropic diffusion and anisotropic diffusion of water. Similarly, Trudeau *et al.* [48] did water diffusion measurements in parenchyma of fresh celery where diffusion was isotropic. Boujraf *et al.* [49] used a phantom consisting of asparagus stems as a test object for assessing the value of the acquisition and postprocessing techniques commonly used in the clinic for this kind of investigation. Asparagus exhibits a well-defined sub-classification of cells on the basis of size and shape, allowing a relatively simple interpretation of the results obtained in the diffusion experiments. The average diameter of asparagus stems is approximately 30 mm [30]. Other authors used asparagus in construction of phantoms due its well-known cell structure that leads to axial diffusion anisotropy, with a larger diffusivity along the stalk than transverse to it by approximately 30% [50–53]. More recently, Osage orange, a fruit with columns running from the central core to the surface, where each column was found to provide anisotropic diffusion, was used as a diffusion imaging phantom. The Osage orange was acceptable as a diffusion imaging phantom, obtaining values of FA around 0.28 [54].

Plant phantoms, in general, may be used for short-time investigation but they are not suitable for serial studies required for a QC protocol due their inherent instability as they decompose. Equally, cell structures depend of the maturation time so there will be differences that will influence diffusion parameters [30].

Regarding phantoms based in biological tissues, this type of phantoms is a useful tool for testing and validating diffusion models, because its structure to be similar to the in vivo situation. On the other hand, availability of biological tissue is not easy, preparation requires specialized knowledge and due to limited storage time and lack of stability, this type of phantom is not suitable for calibration [55]. There are several studies that works excised tissue based phantoms. In 1994, Ford *et al.* [56] studied apparent diffusion coefficient (ADC) in rat spinal cord. ADC is another measure used in diffusion imaging techniques. The extent of tissue cellularity and the presence of intact cell membrane help determine the impedance of water molecule diffusion. This impedance of water molecules diffusion can be quantitatively assessed using the ADC value [57–59]. Ford *et al.* [56] observed that along the longitudinal axis of the injured cord ADC values decreased and transverse to the cord the values increased. This study showed that ADC

measurement may complement routine imaging for evaluation of spinal cord injury. Trudeau *et al.* [48] used freshly excised spinal cord of pigs to study diffusion, where, in white matter, the measured diffusion coefficient was anisotropic and independent of sample orientation in the magnetic field. Similarly, Gulani *et al.* [60] measured the apparent diffusion tensor in excised and fixed spinal cords of rats, comparing myelin-deficient rats and age matched controls. The results showed that while myelination is not a prerequisite for diffusion anisotropy, it does influence the magnitude of the observed anisotropy. Madi *et al.* [61] also used excised rat spinal cords for testing new DTI sequences. Equally, excised rat spinal cords were used to develop new fiber tracking algorithms [62]. In 2007, Freidlin *et al.* [63] investigated the feasibility of using a hierarchy of models to describe diffusion tensor magnetic resonance data in fixed tissue, also using excised pig spinal cord. More recently, Numano *et al.* [64], using rat brain, studied the ADC mapping using a multi-shot spiral MRI sequence.

To mimic fiber crossings, synthetic phantoms are the most adequate models and currently research in this area has increased regarding to the use of this type of materials to develop brain phantoms. Synthetic phantoms can be divided in capillary phantoms and fiber phantoms [15].

Regarding capillary phantoms, glass or plastic tubes keep a very well defined geometry and maintain properties reasonably constant over time. However, this type of material cannot be manipulated to achieve complicated white matter arrangements such as fiber crossing and, in general, inner diameters are too large to mimic human axons [15,55].

von dem Hagen and Henkelman [65] used plastic tubes to investigate a model of diffusion analogous to nerve fibers. Polytetrafluoroethylene (PTFE) hollow plastic fibers were used to create an experimental model of white matter fiber bundles, with inner and outer diameters of 50 and 325 μm, respectively. Comparing these dimensions with human axon sizes is possible to conclude that plastic tubes are much larger than radial myelin thickness. In this sense, the density of water was much less than in tissue. Three orientations of the fibers were created (aligned, coiled, and oriented at random). One year later, Lin *et al.* [66] used, also, PTFE fibers with similar dimensions (inner diameter = 50 μm and outer diameter = 350 μm) placed in two orientations (45° and 90°) and they quantified the accuracy of a diffusion imaging in defining crossing fiber orientation.

Yanasak and Allison [67] used capillaries in the construction of an MRI phantom for the assessment of diffusion tensor imaging. The difference regarding studies mentioned above was the material and dimensions. They used arrays of glass capillaries with inner diameters between 20 and 80 μm (Figure 10). Results showed a decrease of eigenvector variance with decreasing capillary diameter.

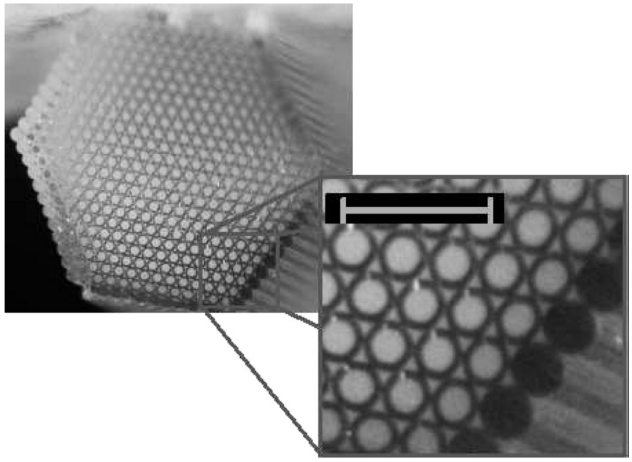


Figure 10: Cross-sectional photograph of the capillary arrays used by Yanasak and Allison [67]. The hash mark in the insert is 0.2 mm in length.

Others authors investigated the behavior of capillary phantoms, also, using hollow capillaries with inner and outer diameters between 20 and 150 μm, respectively [55,68–72].

Regarding fiber phantoms, various materials are used from natural to synthetic fibers with a wide range of diameters. Hemp and linen are examples of natural fibers used in the development of brain phantoms. On the other hand, polyester (PES), polyethylene and polyamide (PA) are examples of synthetic fibers.

Perrin *et al.* [73] started this development of brain phantoms based in fibrous materials since that capillary phantoms do not show any bending and they have too large diameter compared with the diffusion measurement scale. Due requirements as plasticity, permeability and size, it was chosen rayon. Diameter of rayon filaments was about 17 μm, similar to white matter axons (Figure 11). As can be seen in Figure 11 (b), the phantom was built from several layers of parallel fibers in two arms directions, forming an angle of 90°. The whole structure was immersed in distilled water. The results showed that rayon exhibited low values of FA (0.2) comparing with human brain.

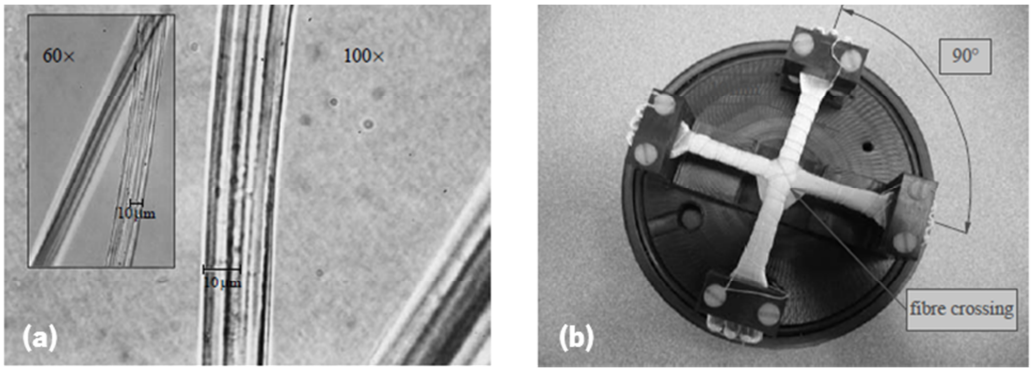


Figure 11: (a) Microscopic view of a rayon textile filament and (b) top view of the phantom [73].

Fieremans *et al.* [74] used Dyneema®, specifically Micro Dyneema®, in total of 400 parallel fibers, each fiber with a diameter of 15 µm. The phantom presented an extremely simple geometry.

Lorenz *et al.* [75,76] to show the differences between natural and synthetic fibers used hemp, linen and rayon as natural fibers and Dyneema® as synthetic fiber. Results showed that synthetic fiber presents higher values of FA comparing with natural fibers. This fact is justified due to the hydrophobic behavior of synthetic fibers. The FA value was similar to human brain for Dyneema®.

In order to investigate and control temperature dependence of diffusion parameters, Reischauer *et al.* [77] developed a diffusion phantom with Dyneema® fibers. The results showed the dependence between temperature and diffusion parameters: with increase on temperature, FA tends to increase.

A problem of Dyneema® fibers, extensively used in brain phantoms due its properties regarding the restriction of water diffusion and anisotropy, is its magnetic susceptibility which is distinctly lower than that of distilled water. Lindemeyer *et al.* [78] purposed an aqueous solution of magnesium chloride to modify the susceptibility of the diffusing liquid to better match that of Dyneema®.

Laun e*t al.* [79] chose polyamide fibers with different diameters (14 – 230 µm) and they observed that FA decrease with increasing of diameter. FA was 0.75 to fibers with 50 µm, diameter a bit higher comparing with human axons.

Other authors investigated the behavior of synthetic fibrous materials to develop anisotropic brain phantoms [27,35,80–85].

Due the dissimilarity between fibrous materials and white matter regarding to geometry and/or permeability properties, hollow fibers produced by electrospinning were studied aiming to approximate geometry of phantom's material to the geometry of human axon [29,86–88]. In particular, co-electrospinning allows the deposition of hollow, aligned and micron-sized fibers, by using a set of concentric needles containing different solutions/melts, for the development of phantoms which mimic the microstructural and bulk characteristics of white matter tracts [29,89]. Polycaprolactone (PCL) and polyethylene oxide (PEO) have been the solutions studied in this area due can be electrospun as individual components, which resulted in a well-defined boundary between the core and the shell in the co-electrospinning process of these two materials. Several parameters influence final diameters of hollow fibers: concentration of solutions flow rate of each solution, electrostatic field, working distance between the coaxial spinneret and the fiber collector [89]. A range of diameters was obtained mimicking white matter. Once again, it was showed that FA increase with decrease of inner diameter. However, besides the maximum value obtained to FA be 0.45, it is necessary a study of the long term stability in solvents [29].

The main conclusions about anisotropic phantoms found in literature are:

- Synthetic fibrous materials present better results when compared to other type of materials, allowing flexibility and hydrophobicity with higher values of fraction anisotropy and stability in solvents;
- Regarding geometry of synthetic materials, in general, fibers used until now do not have a similar geometry with human axons, presenting higher diameter and a solid cross-section (not hollow);
- Complex regions of human axons as crossing (with a range of crossing angles) and kissing are not mimic in phantom;
- FA values, in general, are not similar to the human brain.

3. Synthetic fibrous materials

Fibers are defined as units of matter characterized by flexibility, fineness and a high length to thickness ratio [90]. Fibers can be classified in various ways: based upon the final use of fibrous material (apparel and non-apparel), based in terms of fiber length (continuous or staple fiber) and, based in fiber nature (natural or non-natural fibers) [91]. Thus, according to its nature, fibers

can be natural fibers or non-natural fibers. Natural fibers can be have animal (silk, wool), vegetal (cotton, flax) or mineral (asbestos) origins. Non-natural fibers can be artificial or regenerated (viscose), obtained by natural polymer as cellulose, synthetic (PES and PA) or inorganic origin (glass fiber, carbon fiber) [91,92]. According to Hongu *et al.* [93] the main difference between natural and synthetic fibers is in structure. Synthetic fibers are produced by extruding a polymer through a nozzle followed by drawing. The resulting fiber has a simple structure when compared to the natural counterparts. On the other hand, natural fibers present a multi-phase structure and a non-even nonhomogeneous surface. Synthetic fibers, according to International Organization for Standardization, are defined as fibers manufactured from polymers built up from chemical elements or compounds [94]. They appeared in the market in 1938 made by PA, the first synthetic fiber material. Polyester, polyurethanes and polyolefins are other important synthetic fibers materials. Properties as high tensile strength, dimensional stability, high hydrophobicity, easy handling and high resistance to pests, light and mold are commons in synthetic fibers.

In terms of length, fibers can be classified in continuous or staple fibers. The first ones have practically an infinitive length while staple fibers can be a short length between 10 – 400 mm. It can be said that fiber is the unit in making textile yarns and fabrics [91].

Yarns can be categorized in various ways. The basic yarns can be multifilament, monofilament and staple or spun. Multifilament yarns have a lower flexural rigidity comparing with equivalent monofilament yarns due the presence of large thin fibers in multifilament [95]. Filaments in a continuous multifilament yarn are slightly twisted as they come from a fiber production tools. When more interfilament cohesion is required, continuous multifilament yarns are twisted [96].

Fiber shape can be analyzed by cross-section of the fiber (cross-sectionally) and by fiber lengthways (longitudinally). Natural fibers present a wide range of shapes, while synthetic fibers can be almost any desired shape. Cross-section of fibers can be round, trilobal, multilobal, dog-bone shaped, serrated, hollow, etc., as illustrated in Figure 12.

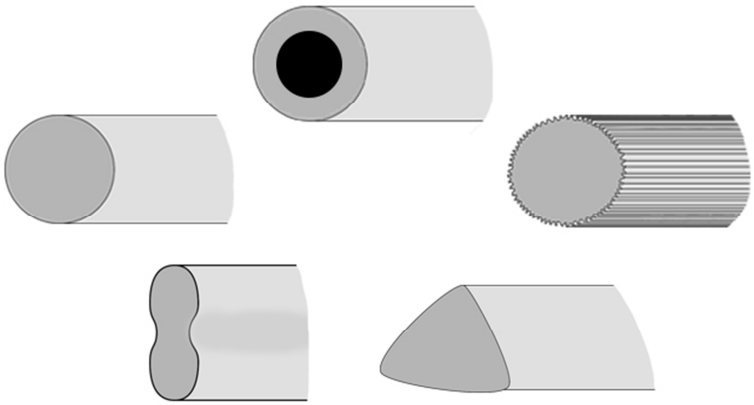


Figure 12: Different types of fiber cross-sections.

Longitudinally, fibers can present smooth, rough, cracked, uneven surfaces. Both shape and surface are important characteristics which influence properties as wettability, wicking, cohesion, etc.

3.1. Melt spinning

Spinning processes are the most employed to manufacture yarns, continuous or staple fibers. The most common spinning process is melt spinning where the filament is produced from a melt. A polymer in the form of pellets is fed into an extruder, being melted and then pumped through a spinneret to form filaments. A suitable shape of holes in the spinneret controls the fiber cross-section shape. Subsequently, they are immediately cooled by quench air to obtain solidified filaments (Figure 13) [91,97,98]. Melt spinning is, generally, followed by the mechanical drawing of the extruded filament which results in increased molecular orientation along the filament axis [97].

It is important to point out that in the production of multifilaments, in order to promote a uniform cooling for all filaments, in the quenching zone and to allow enough separation from each other, the holes of the spinneret are distributed in a staggered configuration.

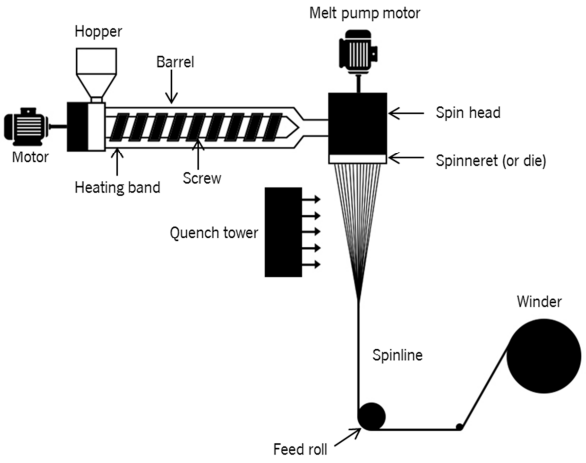


Figure 13: Scheme of melt spining process.

Two types of flows are comprised in the spinning process: shear flow, before the extrusion (flow through of the spinneret) and elongational flow, during the subsequent stretching. Viscoelastic effects are extremely important since defects or breaks can occur in spun filament due flow instabilities. During flow through of the spinneret melt fracture and extrudate swell may also occur. On the other hand, during elongational flow, on the polymer fluid in spinning zone, drawing instabilities may arise, a phenomenon known as draw resonance. Regarding melt fracture, this irregularity is generated by an actual fracture of the molten material, visible on the surface of the filament, as it flows through the spinneret into the spinning space. Melt fracture happens when the polymer is made to flow at a shear stress higher than its critical value. Extrudate swell is the increase of the fiber cross-section when the polymer exits the die, which happens due to the polymer melt viscoelastic nature, which tends to partially recover the deformation it underwent when it was squeezed at the narrow flow channel. Due to this phenomenon, the spinneret to produce multifilament yarns has the holes sufficiently spaced among them, allowing filaments to spin independently without sticking to each other upon extrudate swell. In turn, draw resonance reflects by periodic fluctuations of the filament diameter at the take up of the spinning line. It happens due to a critical draw ratio by the occurrence of sustained periodic oscillations in spin-line variables such as filament cross-section and stress, despite maintaining constant extrusion rate and take-up velocity [99,100]. In literature, several studies about these instabilities during synthetic fibers production are found [101–103].

Flow rate of the molten mass, take-up velocity of the wound filaments, extrusion temperature, dimensions and shape of the spinneret holes and cooling conditions are parameters extremely important for the fiber spinning process. Melt spinning is a very cost effective process comparing

with other types of spinning; it is not necessary to additional cleaning operations since this process does not require solvents. In the case of monofilaments production, cooling has to be done in water, instead of air, due the larger cross-section of this type of yarn [91,104].

Polyamide, polypropylene (PP), polyester are examples of fibers obtained by melt spinning since the polymers are less prone to thermal degradation at the temperatures required to extrude the polymer melt.

In the case of staple fibers, fibers are firstly opened and, if necessary, mechanically cleaned. After, they are combed, by carding process, into a sliver, which is a thick linear assembly of randomly arranged fibers. Sliver needs to reach dimensions of final yarn so it is necessary be attenuated, being thinner. Drafting and drawing processes provide the desire dimension to the sliver. However, it is necessary to take into account mass variation occurring in the drafting process. To give the cohesion to this thin assembly of fibers twisting or wrapping processes are performed [95,104].

3.2. Molecular orientation

Fibers present regions where molecules are closely packed, resulting in regions of high crystallinity and, on the other hand, regions where the molecules present higher disorganization, resulting in amorphous regions. The end application of the fibers is significantly determined by the degree of orientation of these regions [105].

For cristallinity, the most important requirement in polymers is to present some type of stereoregularity. It is essential that regions along the backbone of a significant number of the macromolecules have such regularity, which does not mean that the entire collection of macromolecules, within the sample has to be all isotactic or syndiotactic [106].

Figure 14 shows possible orientation and order of a fiber polymer system. It is possible to see: (a) a unordered and not orientated system, (b) a highly ordered or crystalline region embedded amorphous regions and, (c) other type of orientation and order is when fiber polymer system presents highly crystallinity as well as preferential orientations in a particular direction.

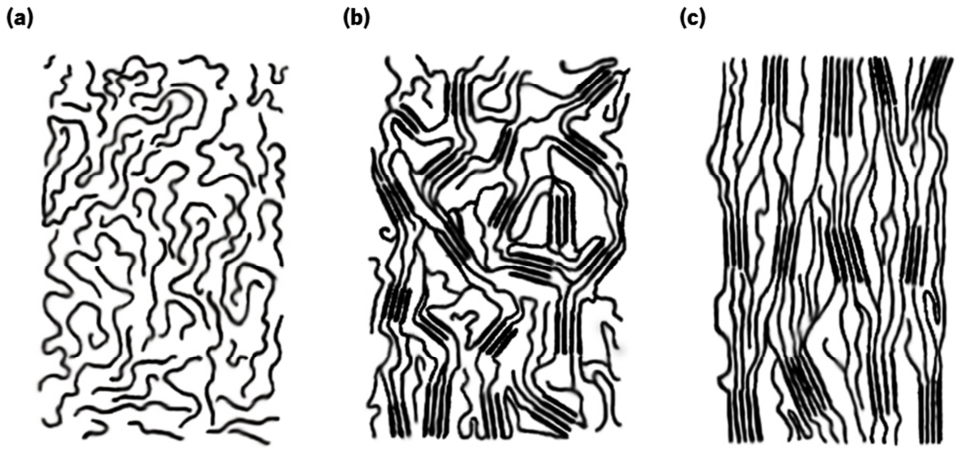


Figure 14: Orientation and order of fiber polymer system: (a) non-orientated non-crystalline; (b) non-orientated but sections ordered; (c) orientated and crystalline.

In natural fibers the variation regarding orientation is created by nature and in synthetic fibers the variation can be controlled during production [107]. Stretching of a molten polymer followed by rapid cooling of the melt and cold or hot drawing process are examples to induce molecular orientation [108].

X-ray diffraction (XRD) of most fibers show that they usually present an oriented crystal lattice, accompanied by an amorphous halo, indicating that fibers consist of partially oriented and partially crystalline regions [109]. Understanding the fine structure of synthetic fibers, which means the way in which the molecules pack together is still uncertain, particularly in quantitative detail of the three-dimensional fiber paths through crystalline and amorphous regions [110].

Partially ordered structures like synthetic fibers require details of the paths and interactions of many molecules for a comprehensive description. To characterize the most important features, six parameters are important: degree of order, referred as cristallinity; degree of localization of order, which distinguishes structures with a well-defined separation into amorphous and crystalline regions; length/width ratio, where lamellar, micellar and fibrillar forms are distinguished; degree of orientation, crystalline and amorphous orientation and also may include transverse and axial orientation; size of localised units that may include cross-sectional shape; and, molecular extent, where direct measurement is not possible. It is an inverse measure of the degree to which molecules are folded to-and-fro in the different regions [109,110].

Polymethylmethacrylate, polycarbonate, amorphous polyamides are examples of amorphous polymers, which slowly soften when heated to their glass transition temperature. In these type of

polymers, increasing temperature, mechanical properties decrease until the threshold of the glass transition temperature. As already referred, polymers are, more often, semicrystalline as polypropylene, polyester, polyamides, except amorphous, etc. Contrary to amorphous polymers, semicrystalline polymers preserve part of their mechanical properties, beyond the glass transition. Also, the dimensional stability is maintained approximately up to the threshold of its melting point [111].

3.3. Hollow fibers

To mimic human axons, some studies from the literature used fibers with hollow configuration. Hollow fibers (Figure 15) are often used in membranes to ultrafiltration, artificial kidneys, artificial lungs, etc. In the same way, this type of fiber configuration is used to improve thermal insulation, which is improved by the air region.

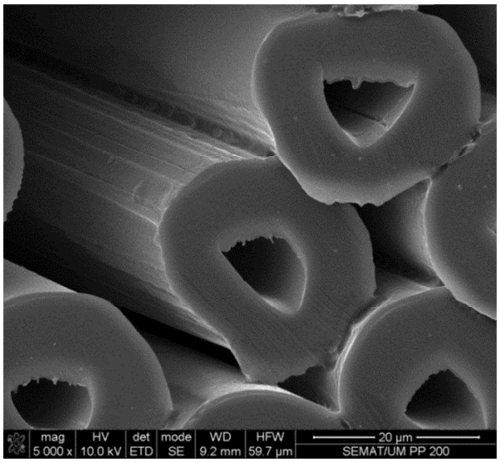


Figure 15: Cross-section of polypropylene hollow yarn.

There are just a few studies about state-of-the-art of hollow fibers because hollow fibers are used, mainly, in membranes form, as referred by Peng *et al.* [112].

Hollow fibers are produced by a fiber spinning technique, described before, but with a special spinneret with the required hollow configuration. Spinning process to hollow fibers is similar to spinning circular cross-sectional fiber, with a difference: the inner radius is an additional dimensional variable [113]. Annular die, with a system of air blown into the inner core, and segmented arc-type die are the two types of spinneret designs used to produce hollow fibers [114]. The type of fiber spinning process is related with extrudate and quench type. When the extrudate does not have any solvent, i.e. is a pure polymer, the method is known as melt spinning. On the other hand, polymer solutions with one or more solvents are used in solution

spinning processes, where wet and dry indicate whether the extrudate passes through a liquid quench bath or not . These processes use a bore fluid, which can be gas or liquid, to preserve inner fiber hole [115]. Polymer viscosity, spinning temperature, throughput rate and fiber take-up velocity are the main parameters of the production process [116]. Properties of fibers are dramatically affected by changes in the rate of fiber spinning as well as any subsequent cold drawing [117]. Wall thickness is an important dimension for hollow fibers. This type of fibrous materials is characterized by the ratio of the void area to the whole area of the fiber. Void percentage, also known as hollowness, defines that ratio [109].

Comparing with synthetic fibers of the same outer diameter, cost savings can be achieved by using hollow fibers since these require less raw materials [118].

4. Final Remarks

Taking in account the state-of-the-art, the development of an anisotropic brain phantom that mimics human white matter axons as well as the complex regions of brain white matter is imperative to provide referent measurement, aiming to achieve the first true calibration of diffusion measurement in the MRI. Thus, a systematic study of fibrous materials used to development a brain phantom is crucial, being an innovation in this area, since in the literature there is no work that includes the study of physical, chemical and mechanical characteristics of the material used in development of brain phantoms. Understanding materials properties is extremely important to support their selection to build the brain phantom and to explain the observations during MRI scanning.

CHAPTER II: Fibrous materials for development of brain phantom

1. Introduction

Currently, in roverethe field of diffusion MRI lacks a ground truth standard that can be used to validate diffusion models for the microstructure of tissue. Besides attempts that have been made to create a phantom simulating diffusion patterns using biological and synthetic fibers as described in Chapter I, the ideal validation study demands a physical phantom with well-known structure and diffusion behavior. Thus, it is necessary to develop an anisotropic brain phantom that mimics, as close as possible, the human axons by using hollow and hydrophobic fibrous materials, with desirable diameters within the range of neuronal white matters. Synthetic fibrous materials have shown better results when compared to natural fibers in development of anisotropic brain phantoms [27].

Polyamide, polyester and polyolefins (polypropylene and polyethylene) are the three most common types of synthetic fibers available in the market [94].

Polyamide fibers, known as nylon®, exist both in crystalline and amorphous forms. PA polymer backbone present a characteristic amide group (-CO-NH-) alternating with a $(CH_2)_n$ group. PA 6 and PA 6.6 are two types of PA with a great commercial importance, and the difference between both is in the number of carbon atoms forming the polyamide. They are identified as PA x, y, where x and y are the number of carbon atoms in the diamine and the diacid respectively. Carbon (C), hydrogen (H), oxygen (O) and nitrogen (N) are combined into adipic acid hexamethylene diamine and caprolactam and after condensation polymerization is formed the molecule of polyamide. In polymide 6.6, the diamine and dibasic acid contain 6 carbon atoms each. On the other hand, in polyamide 6, this is obtained by self-condensation of a single constituent (Figure 16) [91,119,120].

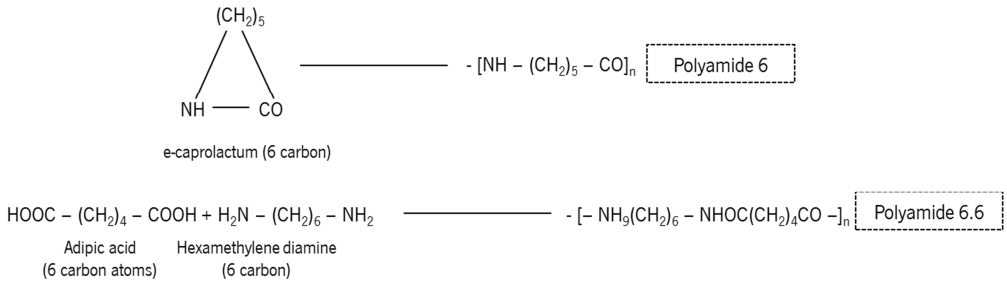


Figure 16: Chemical reactions to obtain polyamide 6 and polyamide 6.6.

Polyester fiber is very important in the synthetic fibers world and it is obtained by polyethylene terephthalate (PET). To produce polyester, a chemical reaction between terephthalic acid and ethylene glycol occurs at a temperature around 280 °C (Figure 17) [91,119].

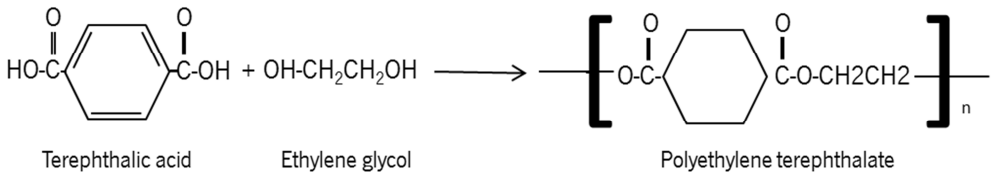


Figure 17: Polyethylene terephthalate reaction.

Due to the aromatic ring and its associated C – C bonds, PES present a stiffer structure when compared to polyamide. In the same way, it presents a bulkier structure than PA and therefore it is less flexible and its crystallization rate is slower.

Polyolefins fibers are also important synthetic fibers including polyethylene and polypropylene, being polypropylene the most widely used. Polypropylene is made by polymerizing of a gaseous by product of petroleum refining with a catalyst, known as propylene. In the chemical reaction, many propylene molecules are linked to form a long chain – the polypropylene macromolecule (Figure 18) [91,121].

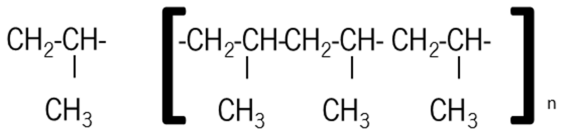


Figure 18: Propylene monomers and polypropylene chain.

During polymerization, -$CH_2CH(CH_3)$- sequences can be added in either a right- or a left-handed screw direction, due to the stereochemistry of the chain. Atactic polypropylene is formed when the chain presents an irregular shape because these forms have a random occurrence. On the other hand, when units are added in the same sense polypropylene assumes isotactic form when molecule is regular and will crystallize. Syndiotactic polypropylene is another regular form, alternating right- and left-handed groups [122].

Table 1 shows some properties of polyamide, polyester and polypropylene fibers.

Table 1: Properties of polyamide, polyester and polypropylene fibers [95,123]

	Polyamide 6.6	**Polyester**	**Polypropylene**
Density (g/cm^3)	1.14	1.38	0.91
Melting Point (°C)	260	250 – 266	160 – 175
Glass transition temperature (°C)	57	73	-14
Thermal conductivity (W/m^2k)	0.243	0.141	0.117
Moisture regain (65 % relative humidity)	4 – 5	0.5	0

In the case of hollow fibers, extremely important shape to mimic the tube-shaped geometry of human axons, they are usually made in the form of staple fiber and spun from a modified staple spinning pack, which is a disadvantage to mimic human axons due to its discontinuous length [124]. An example of PES hollow fibers (Thermolite®) is presented in Figure 19. Beyond the discontinuous length due to staple fiber yarns, yarns are twisted between them. On the other hand, formation of hollow polypropylene fibers was reported to be complex due to large die swell, and spinning of polygonal hollow fibers was found less stable than that of their solid circular counterpart [125].

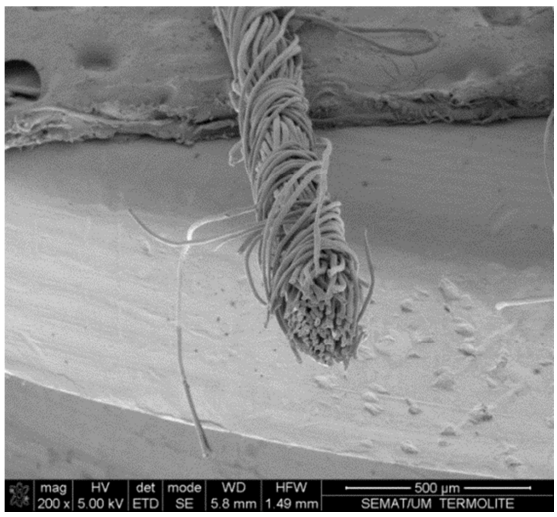


Figure 19: Hollow polyester staple yarn.

As referred in Chapter I, to obtain yarns, fibers are subjected to the spinning process being the melt spinning the most commonly used. In order to decrease the diameter of synthetic fibers,

electrospinning have been used to produce fibers with very small dimensions [126,127], being an option to melt spinning process.

Electrospinning allows producing hollow fibers with micro and nanometric diameters by the deposition of hollow, aligned, micron-sized fibers to mimic the microstructural and bulk characteristics of white matter tracts [29]. The standard laboratory setup for electrospinning involves three systems: an injection pump comprising a syringe and a metallic needle, a source of high voltage direct current (DC) electrically connected to a fluid and a collector. A prepared solution or melt is inserted in the syringe (Figure 20).

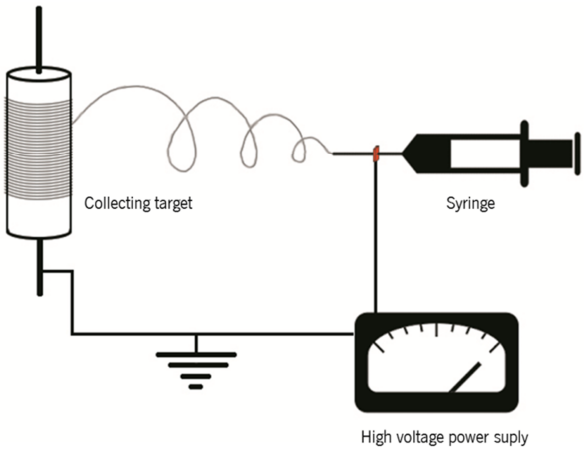


Figure 20: Electrospinning apparatus.

Source of high voltage is connected to the needle of the injection pump, by a positive electrode, and a negative electrode is connected to collector, creating a potential difference between needle of the injection pump and collector. The tip of the pipette or needle that is attached to the syringe is charged with a voltage, and when the electric field produces a force that overcomes the surface tension of the solution, a jet of polymer is drawn from the syringe and attracted to a grounded collecting plate placed some distance away from the needle. Immediately after leaving the needle, the jets form a Taylor Cone, and as it travels toward the grounded target, the solution gradually evaporates, leaving small fibers to collect on the collector [89,128]. The way the fibers are collected can influence the fiber orientation and consequently the final application. Therefore, there are several types of collectors, like a single ground, rotating single ground, dual bar, dual ring, single horizontal ring, etc [89].

In order to mimic tube-shaped human axons, and in accordance with the literature, the choice of materials for this study took into account the following aspects:

- Synthetic fibrous materials are hydrophobic, presenting an anisotropic behavior when compared to natural fibers;
- Synthetic fibrous materials have higher resistance to water than natural fibers;
- Human axons present diameters ranging from less 1 μm to around 25 μm;
- Human axons present a tube-shaped cross-sections and can reach 1 m in length;
- Different materials promote different water motion orientations and, consequently, different fractional anisotropy values.

Considering the aspects referred above, to obtain the desired characteristics comparable to human axons, three different technologies were used in the present study: polypropylene and polyamide hollow multifilament commercial yarns obtained by melt spinning technique; post-production stretching of the previously mentioned hollow yarns using a laboratorial filament extrusion line; and, production of coaxial electrospinning polycaprolactone fibers by electrospinning. The analysis of the cross-section and respective diameters of yarns is presented in this chapter.

2. Materials and methods

2.1. Hollow multifilament yarns

Two potential fibrous materials, produced by melt spinning, to build the anisotropic brain phantom were studied:

- Polypropylene hollow multifilament yarns, supplied from Multicol, with 64 filaments/yarn and 0.905 g/cm^3 density;
- Polyamide 6.6 hollow multifilament yarns (Meryl® Nexten), supplied from Nylstar, with 30 filaments/yarn and 1.14 g/cm^3 density.

Multifilaments were made by, practically, non-twisted filaments (the filaments were slightly twisted during extrusion process). Taking into account the brain phantom application, the non-twisted yarns allow a more oriented water movement when compared with twisted yarns, since in general white matter human axons present a water flow in parallel orientation due to myelin sheath, as explained in Chapter I.

Regarding PP hollow multifilament yarns, the production process was closely observed. Melt spinning extrusion technique using a vertical extruder with 4 spinnerets, each one producing a

spool of yarn was used. The PP pellets were melted for extrusion and forced to pass through a filtering unit to remove the impurities of the molten polymer mass, as they may block the fine holes of the spinneret plate. The molten polymer was then pumped through the spinneret, specially designed to form the desirable hollow configuration (Figure 21). The molten filaments were cooled by air in a quench tower and winded in a roll.

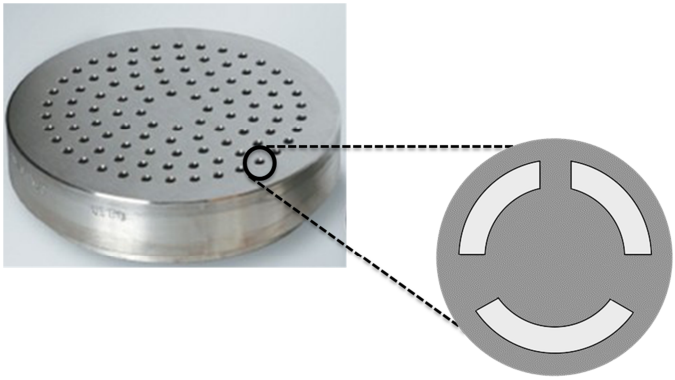


Figure 21: Schematic representation of the spinneret used to produce polypropylene hollow multifilament yarns.

The lowest linear mass produced by Multicol to commercialization is 34 tex. In order to mimic the range of human axons that can be found between from less than 1 μm to about 25 μm and to evaluate the effect of diameter in brain phantom scanning results, mass throughput rate of extrusion process was decreased, without modifying the take-up speed, with the aim to obtain yarns with inferior linear mass and, consequently, inferior dimensions. Five types of PP hollow multifilament yarns, with different linear densities, were obtained at the Multicol melt spinning line.

Regarding PA multifilament yarns, since their production was not performed in Portugal the detailed information about the process was not provided by the company.

2.1.1. Characterization of hollow multifilament yarns

Cross-section analysis of hollow filaments was observed by scanning electronic microscopy (SEM) using Nova NanoSEM 200 with an accelerating voltage of 10 kV. For that, samples were coated with a thin gold film to increase its electrical conductivity. A custom-made cutter (Figure 22) was used to perform the transversal cuts of the yarns, since the commonly employed cutting by cryo-preparation method resulted in flattening the yarns cross-sections. This simple cutter is composed of an orifice where the yarns are inserted transversely (red circle in Figure 22) and placed in a tight arrangement. Then a sharp cutting blade is used to section the profile in a single

move. Using image analysis software Image J®, outer and inner filament areas were measured and, posteriorly, diameters calculated. Although the hollow parts of the filaments are not perfect circles, the term diameter is nevertheless used to express the dimension, as the shape is nearest to that of the circle and in literature are found values relative to the human axons diameters [16,36]. 30 readings was taken at random locations and the mean was calculated.

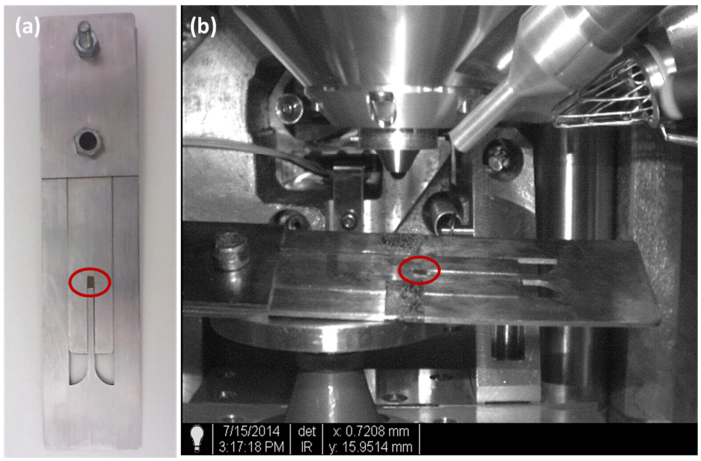


Figure 22: Cutting tool used to obtain the yarns cross-section for further visualization on SEM: (a) photograph of the cutting tool and (b) the same tool prepared inside SEM equipment. Red circle highlighted the hollow filaments already cut.

Linear mass of yarns was quantified using NP EN ISO 2060 standard [129].

Yarn diameter is not a straightforward parameter to measure [130]. Equations that related diameter with linear mass are found in literature [131]. However, there are studies showing that diameters predicted by relationships quoted in the literature can be much smaller than those experimentally observed [132]. The diameter of the yarn does not only depend on the material and on the yarn linear mass, but also on many other factors, like twist, type of fibers, spinning technologies, etc. [133]. Therefore, and taking into account that yarns used in this study were non-twisted hollow multifilament yarns, PP and PA hollow multifilament yarns were examined longitudinally by a transmission microscope and images were captures using a digital camera and analyzed by Leica Application Suite software. 20 readings was taken at random locations and the mean was calculated. A similar method based on image analysis technique was recently applied to measure yarn diameter [134].

Hollowness was defined as the hole area divided by the fiber total area, according to Subashini [135]. Equation 1 was used to obtain hollowness.

$$Hollowness\ (\%)\ =\ \frac{Inner\ Diameter}{Outer\ Diameter}\ x\ 100$$

Equation 1

2.2. Post-production stretching

Subsequently to the SEM analysis of the filament cross-sections and, with the aim of obtaining the most approximate dimensions to those found in human axons, a post-production stretching was done to the yarns produced in Multicol, using a drawing stage of a laboratorial filament extrusion line. Multifilament yarns were stretched using the prototype downstream equipment of a filament extrusion line from the Department of Polymer Engineering of the University of Minho (Figure 23).



Figure 23: Prototype downstream equipment of a filament extrusion line.

The parameters for stretching process were chosen by trial-and-error. Changes in the oven temperature and stretch ratio were studied as conditions to obtain filaments with half of the initial areas. Regarding PP hollow multifilament yarns, the temperature applied in first oven was 170 °C and in last oven was 20 °C. The stretch ratio was 3:1. The five types of PP hollow multifilament yarns produced in Multicol were subjected to this post-production stretching. Consequently, this technique allowed for obtaining other five types of PP hollow multifilament yarns with linear masses about half of ones of the yarns produced in Multicol. Regarding PA hollow multifilament yarns, post-production stretching was also performed but due to the high melting temperature is more difficult to control the process and the stretching of the PA was not achieved in stable

conditions. Mainly, mechanical rupture occurred before reaching the temperature required to stretch the PA 6.6 filaments.

Similarly to commercial yarns, filament cross-sections were observed by SEM and diameters were measured using Image J®, linear mass of yarns was quantified following the NP EN ISO 2060 standard [129], hollowness obtained using Equation 1 and yarn diameters were measured using image analysis technique as explained above.

For easier understanding of the tests and results, sample coding of PP hollow yarns was done according to material type (PP) and numbered by descending order of its linear mass since the yarn that is produced by Multicol for commercialization is 34 tex PP, which is, in this work, the yarn with the higher linear mass. To distinguish yarns obtained in post-production stretching, an "S" was added to the sample coding. For example, PP 1 is polypropylene yarn with 34 tex, produced in Multicol, and PP 1S is the same yarn (PP 1) after post-production stretching. Regarding polyamide yarns, sample coding was done only according to material type (PA).

2.3. Electrospun fibrous materials

Electrospining process was used in this research work to obtain hollow fibers with smaller diameters. PCL and PEO were used since both are electrospinnable materials studied before [29,87]. PCL (weight average molecular weight Mw = 70 000 – 90 000) and PEO (viscosity average molecular weight Mv = 900000) were obtained from Sigma Aldrich. Regarding the solvents, chloroform, N,N dimethyl-formamide (DMF) and cyclohexane were also purchased from Sigma Aldrich. Deionized water was used to dissolve the PEO. A 10 w/w % solution of PCL in chloroform/DMF (8:2, w/w) was used as the shell fluid. A 4 w/w % PEO in deionized water acted as the core fluid.

Preliminary tests were performed using a coaxial spinneret, with two concentric needles, filled PCL solution (outer needle) and PEO (inner needle), being independently controlled by two syringe pumps. A wide rotating drum was used as a collector to align the fibers (Figure 24).

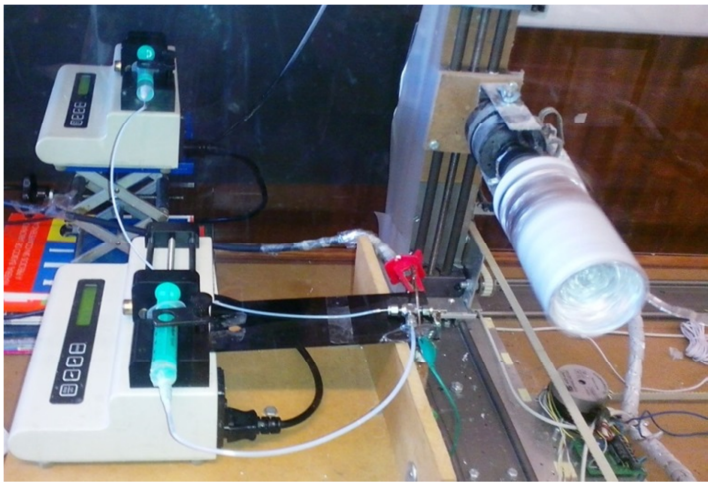


Figure 24: Electrospinning apparatus used to produce aligned hollow fibers.

The outer needle was connected to the positive electrode from a DC high voltage power supply, and the fiber collector, which was placed 6 cm from the tip of the concentric needles, was connected to the negative electrode (ground). A voltage of 12 kV was applied and the flow rate of the outer solution was fixed at 3 mL hr^{-1} and the inner solution was fixed at 0,8 mL hr^{-1}. Tests were conducted at 31 % moisture and 22 °C temperature.

This part of work was done at Faculty of Sciences and Technology of Nova University of Lisbon with Soft Matter and Bio-functional Materials Group of CENIMAT.

Surface and cross-section of electrospun fibers were analyzed by SEM images, using the commonly employed cutting by cryo-preparation method. Image J® was used to obtain the fibers diameter.

3. Results and discussion

3.1. Characterization of hollow yarns

Figure 25 to Figure 29 show the cross-section of PP hollow filaments before and after the post-production stretching.

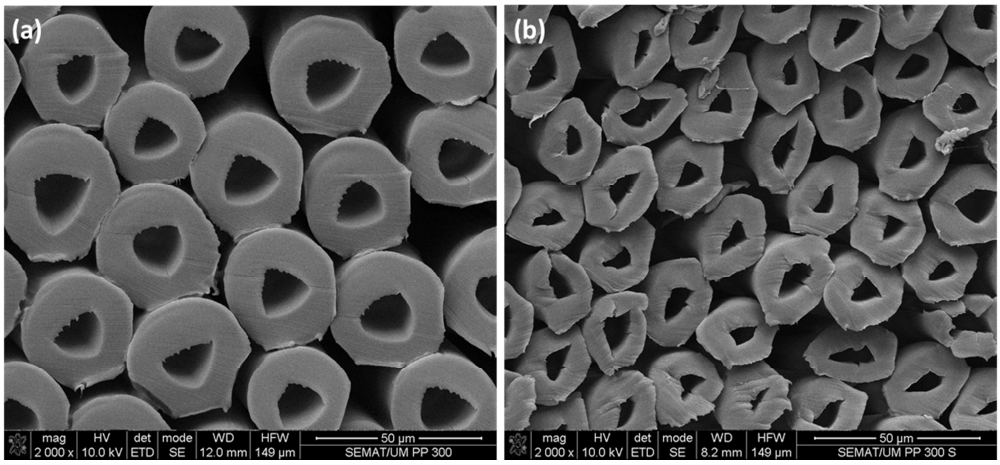


Figure 25: Cross-sectional of PP 1 filaments before (a) and after (b) post-production stretching.

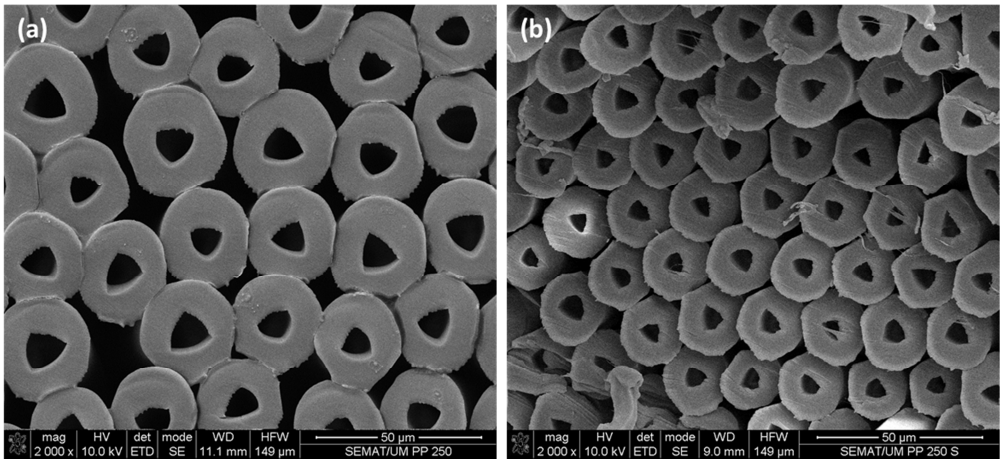


Figure 26: Cross-sectional of PP 2 filaments before (a) and after (b) post-production stretching.

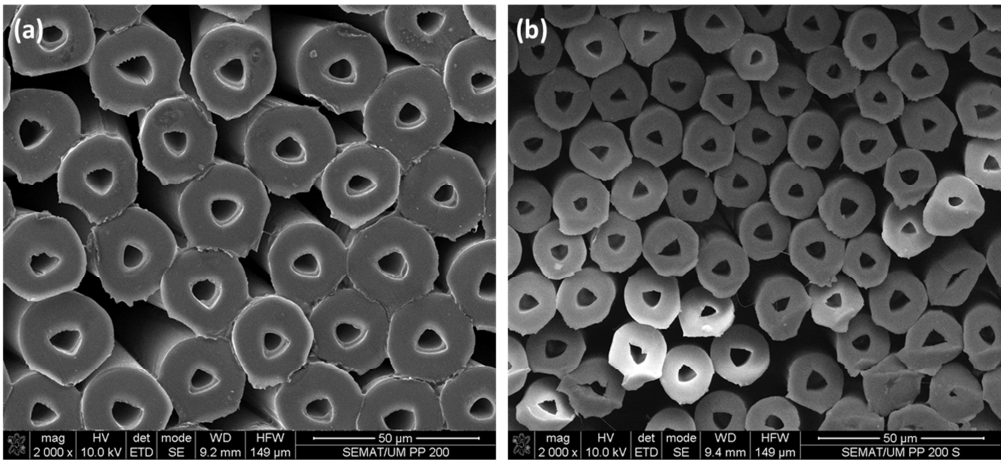


Figure 27: Cross-sectional of PP 3 filaments before (a) and after (b) post-production stretching.

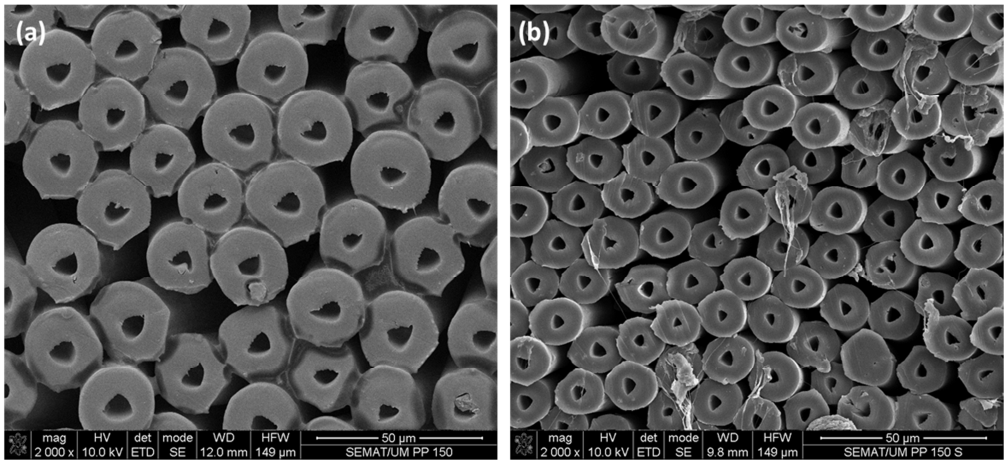


Figure 28: Cross-sectional of PP 4 filaments before (a) and after (b) post-production stretching.

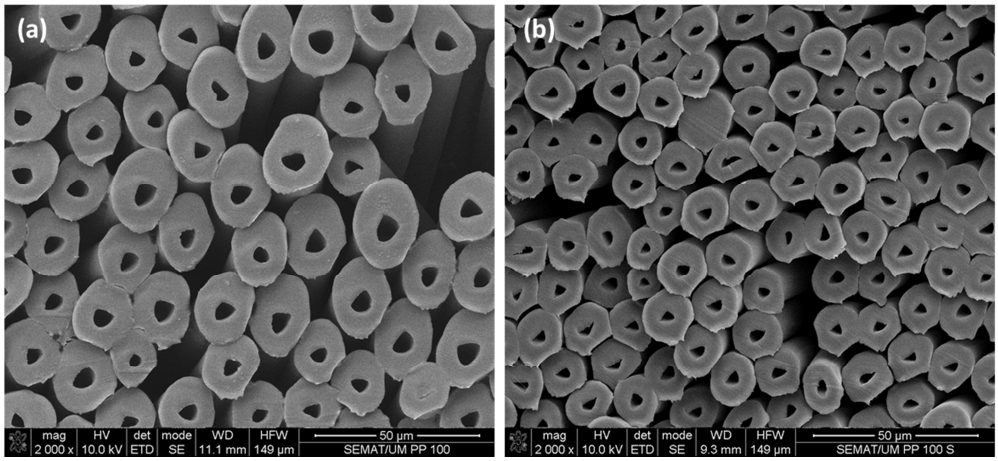


Figure 29: Cross-sectional of PP 5 filaments before (a) and after (b) post-production stretching.

Table 2 shows linear mass, the diameters of cross-section and of yarn and respective hollowness.

Table 2: Linear mass, outer and inner diameters, yarn diameter and hollowness of PP yarns

Yarns	Linear mass (Tex)	Outer diameter (µm)	Inner diameter (µm)	Yarn diameter (mm)	Hollowness (%)
PP 1	34.00 ± 0.39	33.53 ± 2.26	11.84 ± 1.19	0.74 ± 0.11	35.31 ± 0.06
PP 2	28.25 ± 0.60	29.35 ± 1.39	9.52 ± 0.72	0.77 ± 0.12	32.44 ± 0.04
PP 3	22.00 ± 0.39	25.78 ± 1.46	5.71 ± 0.73	0.57 ± 0.10	22.15 ±0.04
PP 4	16.80 ± 0.24	22.01 ± 1.21	5.53 ± 0.44	0.4 ± 0.06	25.12 ± 0.03
PP 5	11.00 ± 0.39	20.12 ± 6.44	5.44 ± 0.72	0.3 ± 0.04	27.04 ± 0.12
PP 1S	14.50 ± 0.59	23.21 ± 1.39	7.46 ± 0.88	0.46 ± 0.04	32.14 ± 0.06
PP 2S	13.55 ± 0.35	20.44 ± 1.48	5.39 ± 0.62	0.45 ± 0.09	26.37 ± 0.05
PP 3S	9.55 ± 0.42	17.56 ± 0.98	4.74 ± 0.69	0.46 ± 0.05	26.99 ± 0.05
PP 4S	6.80 ± 0.33	14.69 ± 0.62	3.72 ± 0.30	0.26 ± 0.10	25.32 ± 0.03
PP 5S	5.80 ± 0.24	14.30 ± 0.70	2.84 ± 0.43	0.15 ± 0.03	19.86 ± 0.04

Comparing Figure 25 (a), Figure 26 (a), Figure 27 (a), Figure 28 (a) and Figure 29 (a), it was observed a decrease on the filaments cross-section with the decrease of the mass throughput rate of extrusion process. Similarly, comparing Figure 25, Figure 26, Figure 27, Figure 28 and Figure 29 before (a) and after (b) post-production stretching, it is possible to confirm again the expected cross-section decrease, showing both decrease of mass throughput rate of extrusion process and post-production stretching allowed additional reductions of the filaments dimensions, in order to mimic the human axons diameters. The variability in the diameter of the filaments within the same multifilament yarn was also observed, which is related to the production process sensitivity. The swelling effect, which occurs in cast polymer extrusion, plays an important role in the definition of the geometry obtained. However, small changes in the process conditions affect the filament geometry. Swelling phenomenon is characterized by the increase of the extruded diameter relative to the diameter of the die. It occurs due to the relaxation of the chains that tend to return to their random conformations, which were directed during its passage through the matrix [113]. Among many other factors, the rheological behaviour of PP also influences swelling [125,136]. Similarly, environmental conditions during the production process did not always remain constant, which not only affected the hole as all the filament shape. Nevertheless, these variations are not considered a drawback of the method since it allows for mimicking the inherent

variation observed in brain axons, which typically range between 1 and 25 μm in humans [16,36].

Regarding the yarn diameter, as hollow multifilament are, practically, non-twisted yarns the diameter is a difficult parameter to measure, due to the interfilament spaces. In general, and by analyzing Table 2, yarn diameter decreased with the decrease of linear mass, as expected.

Regarding hollowness values for PP filaments (Table 2 and Figure 30), it is possible to see that for the PP yarns before post-production stretching there was a decrease of void percentage with linear mass until PP 3, slightly increasing in PP 4 and PP 5 samples. Although, hollowness percentage was not linear for all PP yarns, it is possible to affirm that PP 1 filaments presented the higher hollowness value and PP5 a lower hollowness value comparing with PP 1. After post-production stretching, PP 1S and PP 5S filaments presented the highest and the lowest hollowness percentages, respectively; and, between PP 2S and PP 3S filaments there was a slight increase, decreasing in PP 4S and PP 5S filaments. This behaviour might be an outcome of the above mentioned process conditions oscillations, typical of extrusion line, being polymer throughput rate one of the most critical factor affecting percentage of hole area in fibers [113]. The trend of larger hole area with increasing polymer throughput observed in the present study is in accordance with Prahsarn *et al.* [116].

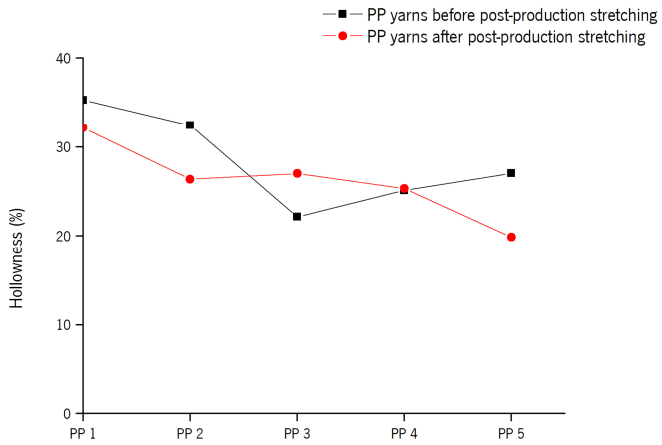


Figure 30: Hollowness PP values before and after post-production stretching.

The hollowness of the filaments is an interesting property in terms of the axons-mimicking structures since there are different axon diameters and axon/myelin thickness ratios in human

brain [137]. For a better understanding, Figure 31 compares a human axon and a hollow filament.

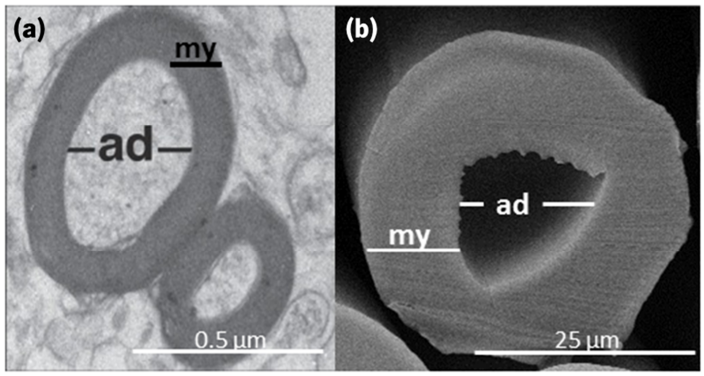


Figure 31: (a) Axon and respective myelin sheath (adapted by [137]) and (b) PP hollow filament axonal diameter: axonal diameter (ad) and myelin thickness (my).

PA hollow multifilament yarns were also further analyzed for its capability to mimic the brain white matter due to be a synthetic fiber and to present hollow configuration. Figure 32 shows PA filaments cross-section.

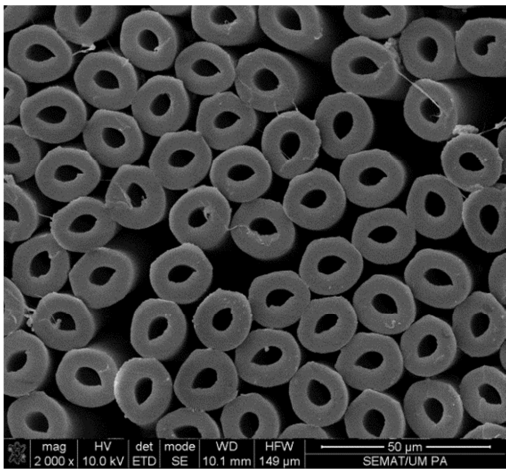


Figure 32: Cross-sections of PA filaments.

Table 3 shows the diameters of cross-section, linear mass, diameters of PA yarns and respective hollowness.

Table 3: Linear mass, outer and inner diameters, yarn diameter and hollowness of PA yarns

Yarn	Linear mass (Tex)	Outer diameter (µm)	Inner diameter (µm)	Yarn diameter (mm)	Hollowness (%)
PA	6.30 ± 0.08	17.46 ± 0.68	6.42 ± 0.32	0.20 ± 0.32	36.77 ± 0.03

Observing Figure 32, it is possible to see that PA filaments presented a hollow cross-section, mimicking the human axons, similarly to what happen with the PP yarns. Table 3 shows that PA filaments presented a high hollowness when compared to PP, observing the relation between hollowness and linear mass. Comparing the PP and PA filament diameters, it is possible to see that PA filaments presented diameters (outer and inner) in the range of the PP filament diameters after post-production stretching. The design of the spinneret and the different properties between both polymers, like density, for example, influence the diameter measures [138].

To help visualizing the scale of the filaments studied in this work, Figure 33 compares the diameter of a human hair, which medium diameter is around 40 to 80 µm, with the diameter of PP filaments [139].

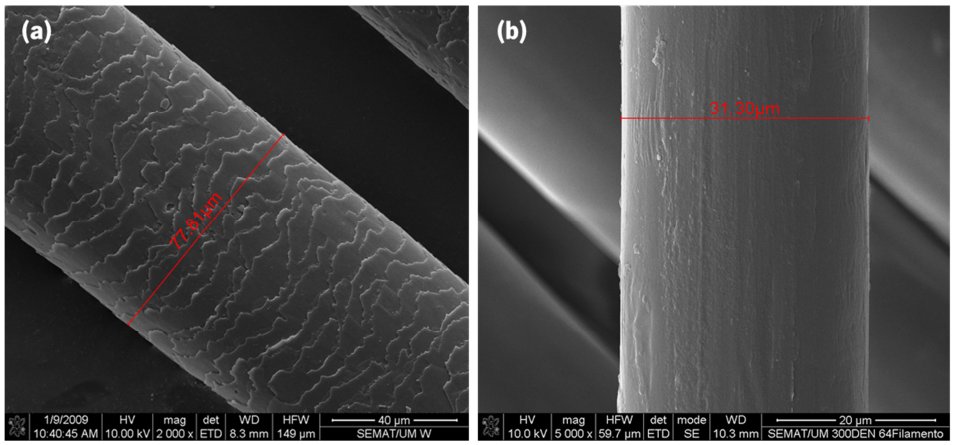


Figure 33: SEM micrograph of longitudinal section of (a) human hair and (b) PP hollow filament, with respective diameters. Please note the different scales.

3.2. Characterization of electrospun fibers

In order to obtain very small fiber diameters, i.e. with reduced diameter when compared to PP and PA hollow multifilament yarns, which mimic the tube-like shape of human axons, PCL/PEO electrospun fibers were also evaluated. Figure 34 shows the SEM images the alignment and the cross-section of electrospun fibers and Table 4 presents the diameter values and hollowness, respectively.

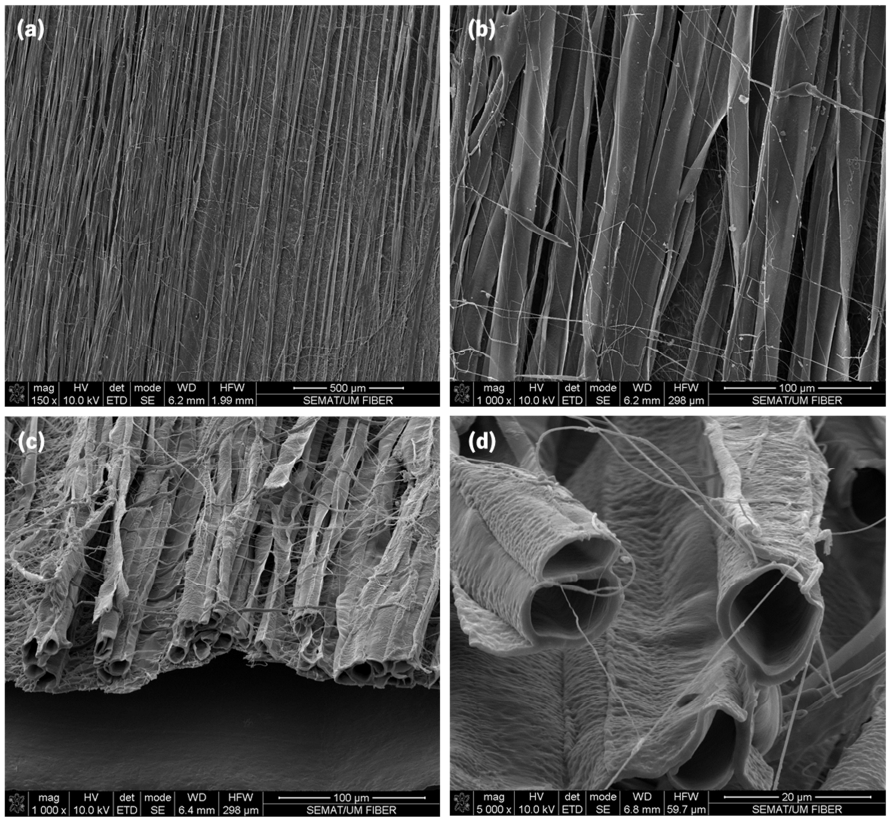


Figure 34: SEM images of (a) and (b) aligned electrospun fibers of PCL/PEO solution and respective cross-sections (c) and (d).

Table 4: Outer, inner diameter and hollowness of electrospun PCL/PEO fibers

Outer diameter (μm)	Inner diameter (μm)	Hollowness (%)
10.20 ± 2.98	8.31 ± 2.82	81.47 ± 0.51

Figure 34 (a) and (b) shows that filaments produced using wide rotating drum collector were, in general, aligned. Observing the filaments cross-sections (Figure 34 (c) and (d)) it is possible to verify that electrospun fibers presented a hollow configuration. Moreover, it is possible to see some filaments without a specific orientation (Figure 34). This fact may be due to the high process sensitivity to different parameters that influence significantly the electrospinning production, like solution properties (viscosity, elasticity, conductivity, and surface tension), processing conditions (voltage, needle diameter, distance from the needle to the grounded target), and the environment (temperature, humidity, and static electricity) [29,86,89,128]. Similarly, according literature, by changing these parameters it is possible to obtain inferior diameters of coaxial electrospun fibers.

Regarding hollowness, electrospinning technique allowed to obtain higher void space percentage when compared to melt spinning technique, whose filament walls were much thinner than the one obtained for hollow multifilament yarns.

In general, results obtained for a flow rate of the outer solution of 3 mL hr^{-1} and inner solution of 0,8 mL hr^{-1}, a voltage of 12 kV and fiber collector placed at 6 cm from the tip of the concentric needles were similar to the results obtained by Hubbard *et al.* [29].

4. Conclusions

This chapter showed three types of technologies used to produce fibrous materials with the desired characteristics comparable to human axons. In order to mimic human axons, fibrous materials need to present a hydrophobic behavior to simulate anisotropic values of the human brain; diameters should vary from less 1 μm to around 25 μm; and, they should present a tube-shaped geometry. Similarly, it is important a parallel disposition between filaments and it is known that different materials promote different water motion.

Therefore, PP and PA hollow multifilament yarns produced by melt spinning were purposed to mimic human axons. These hollow multifilament yarns were exposed to a post-production stretching using a laboratorial filament extrusion line. Furthermore, PCL and PEO were used to produce coaxial electrospinning fibers using the electrospinning technique. Cross-sections of PP and PA hollow multifilament yarns were analyzed by SEM. It was observed that the decrease in linear mass led to a decrease in the size of the filament cross-section. Through the post-production stretching, diameter of the PP filaments was reduced for about half of the initial area. However, PA hollow multifilament yarns did not reach the processing temperature of PA 6.6, not being possible the post-production stretching. The size of the PP and PA multifilaments analyzed was lower when compared to the materials used on brain phantom so far. Regarding to electrospinning process, it was showed that it is possible to obtain aligned hollow fibers using a wide rotating drum. Despite electrospinning seems to be a promising technique to obtain hollow fibers with smaller dimensions, it must be taken into consideration that electrospun fibers are produced in a membrane form, becoming more difficult to create patterns similar to the human brain. Moreover, melt spinning extrusion process of hollow multifilaments is a relatively easier process of significantly shorter operational times to produce long length of yarns. Due to these reasons, the electrospun fibers will not be considered in the following chapters.

Based on the above, the subsequent studies, presented in next chapter will be focused on the chemical, physical and mechanical characterization of just PP and PA hollow multifilament yarns.

CHAPTER III: Characterization of the fibrous materials

1. Introduction

Taking into account the previous chapter where three types of technologies were applied in order to obtain fibrous materials with diameters similar to the human brain axons, PP and PA hollow multifilament yarns presented the best results in terms of geometry, hollow diameter and sample handling.

Existing studies on brain phantoms present some gaps both in terms of geometry and properties of the materials used to mimic human axons. These factors are very important to explain results of the anisotropic brain phantom and also to develop different configurations to mimic, as closest as possible, the human brain.

Properties to take into consideration include the chemistry of synthetic fibrous materials, to check the purity of material, as well as the contact angle, to verify the hydrophobicity, since natural fibers are known to possess a hydrophilic behavior and are susceptible to biological degradation. On the other hand, synthetic fibers exhibit a hydrophobic behavior and typically display higher biostabilities, extremely important in the development of an anisotropic brain phantom.

Tenacity, Young's modulus and extension at break are important mechanical properties of yarns that define the final application. In terms of brain phantoms, this mechanical study of yarns could be interesting for brain phantoms used to validate and to calibrate imaging techniques that assess, quantitatively, the mechanical properties of a tissue. Magnetic resonance elastography (MRE) is a technique for performing noninvasive and quantitative "palpation" by measuring tissue stiffness [140]. It combines MRI with underlying biomechanics, by applying frequency controlled mechanical vibrations whilst acquiring MRI data in a tissue of interest [141]. MRE was described for the first time in 1995 [142]. This type of medical imaging modality detects modifications in mechanical properties of tissues, as liver, heart and more recently brain, that are affected by the presence of disease processes, such as cancer and inflammation, and by age as well [143–145]. Materials used in phantoms applied to evaluate MRE are essentially agar and gelatin or a blend of these materials [146]. Most MRE studies analyze isotropic mechanical properties however tissues as brain white matter possess anisotropic mechanical properties due to their fibrous structure. For that reason, there is a high interest in developing phantoms that simulate both isotropic and anisotropic properties, since most of the solid gel phantoms have isotropic mechanical properties, which are unsuitable for validating anisotropic MRE [147]. A possible

solution should be the use of fibrous materials in combination with gelatins to simulate both isotropic (provided by agar, gelatin or combination of both) and anisotropic (given by fibrous materials) behavior [148].

For that reason, it is also important to study the mechanical properties of fibrous materials used in the development of brain phantoms since they can be used to validate and to make quality control of several neuroimaging techniques.

It should be highlighted that brain phantoms are surrounded by liquid, in general, water. Therefore, materials used in brain phantoms should have stability in water and they should allow the motion of water, mimicking water motion in human axons (Figure 4). The spontaneous liquid penetration in fibers networks, due to capillary forces, knowing as wicking, [149], assumes an important role regarding the simulation of water motion in the axons. The ability to maintain capillary flow is known as wickability and, on the other hand, wettability describes the initial behavior of a fabric or yarn in contact with a liquid [150].
The capillary rise of liquids in a yarn follows the Lucas-Washburn equation [151]:

$$L^2 = \frac{\gamma R \cos\theta_a}{2\eta} t$$

Equation 2

Where,
L – liquid front position or wicking length;
γ – surface tension of the liquid;
η – viscosity of the liquid;
θ_a– apparent contact angle;
R - effective hydraulic radius of the interfilament pores;
t – time.

Related with wickability in yarns, there are numerous studies found in literature. In general, there are several parameters that influence wicking behavior of yarns, as yarn structure, yarns tension, twist, fiber shape and configuration, number of filaments in yarns, finish and surfactants [152–157]. Due to this fact and the fact that, in the case of vertical wicking, Lucas-Washburn equation is limited by the time since it is only valid for very low values of time (t) and not for the complete wicking profile, in this sense, other theoretical models have been proposed to predict the vertical

wicking behavior of yarns. An example is the mathematical model proposed by Das *et al.* [158]. In this theoretical model, several parameters such as fiber denier, yarn denier, fiber cross-sectional shape and number of fibers in the yarn are taken into account in wicking behavior. They concluded that yarn having same linear mass but made of more number of fibers (i.e. with smaller denier fibers) will provide higher wicking. Furthermore, with the increase in twist in yarn, its wickability reduces and with the increase in fiber shape factor, the wickability of yarn increases.

There are different methods to study wicking properties in the yarns: one can be performed maintaining yarns vertically with the lower end immersed in liquor, occurring a spontaneous wicking due to the capillary penetration and the adsorption height is recorded as a function of time [159]; other method uses a Wilhelmy balance to measure weight variations during capillary wicking [160]; image analysis technique can be also applied [161]. It is possible to state that the most used method is the first, where yarns are immersed vertically in a liquid, mainly due to its simple procedure.

There is no literature that focuses on the study of material properties that simulate the human axons of brain white matter. To address this gap, the present chapter describes the characterization of PP and PA hollow multifilament yarns regarding physical, chemical and mechanical properties. Chemical purity of PP and PA was analyzed as well as the hydrophobic behavior was verified by contact angle measurements. Tensile properties of PP and PA yarns were characterized as well as the friction coefficient, important characteristics of textile yarns in general. The percentage of cristallinity was also measured, comparing the differences between hollow multifilament yarns before and after post-production stretching. Moisture and vertical wicking were also investigated since fibrous materials should allow water motion in order to mimic the different diffusion process that occurs in human axons.

2. Materials and methods

Fibrous materials studied in this chapter were PP and PA hollow multifilament yarns.

2.1. Chemical analysis

In order to test the purity of the PP and PA, a chemical and phase analysis using the Fourier Transform Infrared spectroscopy (FTIR) and X-Ray Diffraction (XRD) techniques was carried out.

The polymer cristallinity was measured using the differential scanning calorimetry (DSC) and XRD, to help understanding possible differences between both fibrous materials and between hollow multifilament yarns before and after post-production stretching since cristallinity influences mechanical properties, such as tenacity. Similarly, differences between both techniques was evaluated.

2.1.1. Structure: FTIR and XRD

The FTIR spectra of the PP and PA multifilaments were obtained using an FTIR spectrometer (Avatar 360). Each spectrum was recorded in the range of 4000-400 cm^{-1} averaged over 32 scans.

Phase analysis obtained by XRD, using a Bruker AXS D8 Discover system, Cu-Kα (λ = 1.54060 Å) radiation (40 kV and 40 mA) with a parallel beam configuration, in a Bragg-Brentano, θ - 2θ mode was analyzed since cristallinity behavior explained below was studied using XRD.

2.1.2. Crystallinity: DSC and XRD

The crystallization behavior of the PP and PA multifilament yarns was investigated using DSC and XRD. A DSC 200 F3 Maia® was used under nitrogen atmosphere scanning samples from 30 °C to 200 °C with rates of 10 °C/min. The percentage of crystallinity was calculated using the melting enthalpy, via following formula:

$$\%Crystallinity = \frac{\Delta Hm}{\Delta H^{o}m} \times 100$$

Equation 3

Where,

ΔHm – melting enthalpy of the polymer (J/g);

$\Delta H^{\circ}m$ – melting enthalpy of 100 % crystalline polymer (J/g).

Regarding values of melting enthalpy of 100 % crystalline polymer, for PP was assumed 207 J/g [162] and for PA was assumed 196 J/g [163].

Regarding XRD analysis, to determine crystallinity percentages of samples EVA software was used.

2.2. Contact angle

Typically contact angles are measured using a goniometer. This requires that a drop of the test liquid be placed on the surface of the solid to be tested. Due to the fact that the placement of a drop of liquid on fibers of small diameter is quite difficult, an environmental scanning electron microscope (ESEM) was used to observe the wetting behavior of PP fibers [164]. In the ESEM, small droplets in the micron range can be condensed on the fiber surface within the chamber by controlling the specimen temperature and the chamber pressure. PP and PA samples were precooled to approximately 4 – 6 °C. To minimize the risk of accidental freezing, images were acquired around 7 °C and 1250 Pa. Contact angles of water in filament surfaces were measured from ESEM micrographs, using image analysis software Image J®. For the measurements, it was necessary some adjustments of the images.

2.3. Moisture content

Moisture content of PP and PA yarns was measured according to ASTM 629 – 15 [165] where specimens are heated until they reach constant mass; the loss mass in mass in considered moisture.

2.4. Friction coefficient

Friction coefficient of PP and PA yarns was measured using an automatic system, Attrifil II Mesdan®, according to ASTM D3108 [166], which reports the procedure for friction coefficient measures between fibers and solid materials. The result of the measurement assumes a value between 0 and 1.

2.5. Tensile tests

The tensile tests were carried out based on NP EN ISO 2062:1997 standards [167], using a H100KS Hounsfield Universal Testing Instrument and a load cell of 250 N. The gauge length was 100 mm and speed used during the tests was 100 mm/min. Tests were done in dry and wet conditions, at different temperatures: room temperature (24 ± 2 °C) and human body temperature (36 ± 2 °C), using a thermal chamber. These factors (wet and dry conditions; room and human body temperature) are important to be analyzed since brain phantoms are immersed in liquid, usually water, and can be scanned at different temperatures [77].

2.6. Vertical wicking

The schematic diagram of the experimental setup to measure vertical wicking is shown in Figure 35. The specimens were suspended vertically with their bottom ends dipped in a reservoir containing distilled water. A dye was added to water with aim to facilitate visual tracking of the water movement along the yarn. In order to ensure that the bottom ends of the specimens could be immersed vertically at a depth of 3 cm into the water, the bottom end of each specimen was clamped with a 2.45 g paper clamp. Total length of each sample was 20 cm. For kinetics of wicking heights, distance traveled by water on vertical strip was measured to each minute during 10 minutes, since that beyond this time the behavior of wicking height evolved very slowly, and it is the range of time typically used in vertical wicking [134,168,169].

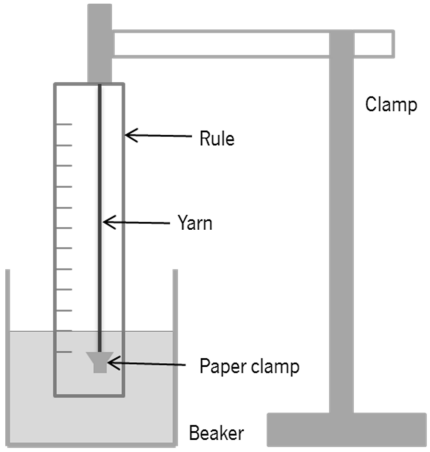


Figure 35: Schematic of experimental set up for capillary rise.

Similarly to the tensile tests, vertical wicking was performed at room (24 ± 2 °C) and at body temperatures (36 ± 2°C) using a hotplate under beaker to heat the water. A thermometer was for temperature control purposes.

3. Results and discussion

3.1. Chemical analysis

3.1.1. Structure: FTIR and XRD

Infra-red characterization absorption peaks of PP 1 and PP 5 are represented in Figure 36 (a) and Figure 36 (b), respectively.

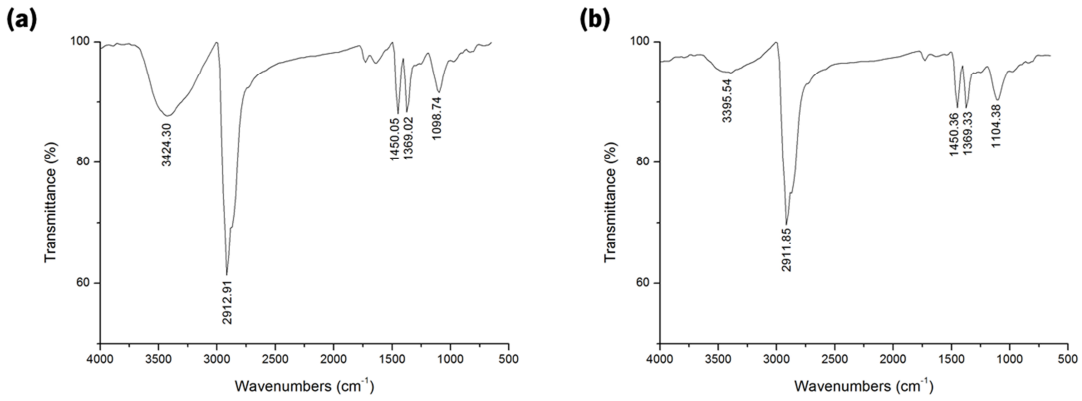


Figure 36: (a) FTIR spectra for PP 1; and (b) FTIR spectra for PP 5.

It can be observed that the major peaks found were associated with typical groups from PP, namely due to hydrogen bonded asymmetric –CH stretching vibration around 2913 cm^{-1}, asymmetrical CH_2 bending at 1450 cm^{-1} and symmetrical CH bending at 1369 cm^{-1}. O-H stretch and free vibrations peak due to hydrogen bonding was also observed around 3400 cm^{-1} due to the absorption of water, which explains why the peak decreases with decreasing diameter, as it is possible to see in the infra-red characterization absorption peak of PP 5 (Figure 36 (b)) [170,171].

As XRD provides structural information, Figure 37 presents XRD diffraction pattern of PP 1, since, as expected, XRD diffraction patterns of other PP yarns are identical.

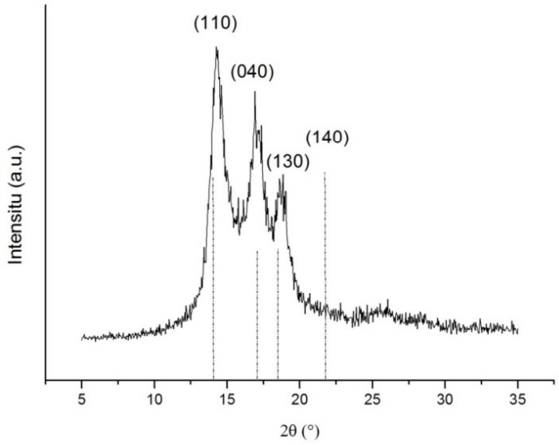


Figure 37: XRD diffraction pattern of PP 1.

The diffraction pattern presented shows a pure monoclinic PP (ICDD card no. 00-054-1936), also confirming the type of material of the yarns. However, it should contain a peak at 21.8°. The

absence of this plane (140) can be explained by preferred orientation of the fibers in plans (110), (040) and (130) during processing.

Figure 38 shows the FTIR spectra (a) and XRD diffraction pattern (b) for PA multifilaments.

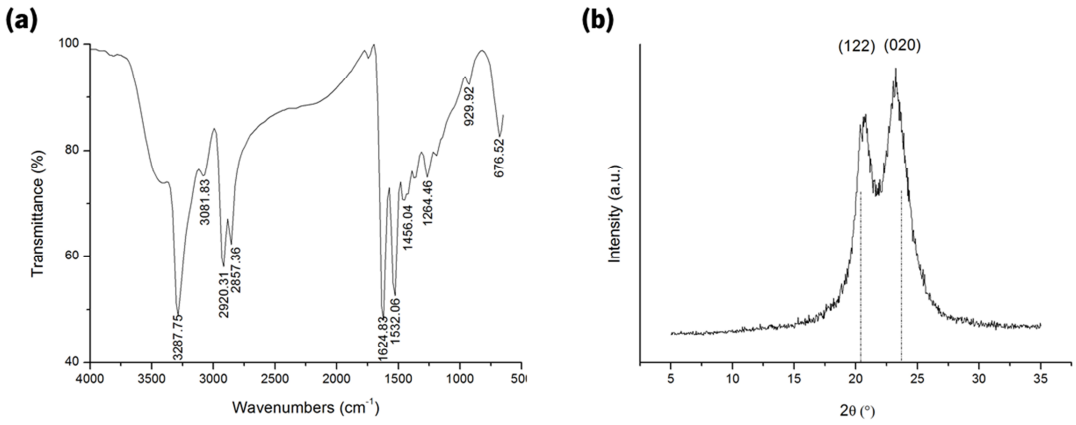


Figure 38: (a) FTIR spectra of PA; and (b) XRD diffraction pattern of PA.

Analysing the infra-red characterization absorption peak it can be concluded that the major peaks found were associated with typical groups from PA. The presence of the amide bands at 1624.83 and 1532.06 cm^{-1} and N-H, C-H (a symmetric stretching) and CH_2 (symmetric stretching) at 3287.75, 2920.31 and 2857.36 cm^{-1}, respectively [172,173] was identified.

The diffraction pattern presented in Figure 38 (b) shows a pure triclinic PA (ICDD card no. 00-047-2017), also confirming the purity of the material.

The FTIR and XRD analysis proved that PP and PA yarns are pure, with no change to its synthetic origin. This fact is important in the development of the anisotropic brain phantom since synthetic materials allow a water motion oriented when compared to natural fibrous materials since natural fibers have a hydrophilic behavior and the affinity with water leads to a random water movement, without restrictions. As there is no change to the synthetic origin of the PP and PA yarns, it is expected that these materials allow an oriented water motion and, consequently, FA values similar to those presented by brain white matter.

3.1.2. Crystallinity: DSC and XRD

Table 5 presents the crystallinity percentage of the PP and PA hollow multifilament yarns obtained by DSC and XRD analysis.

Table 5: Cristallinity results in percentage according DSC and XRD analysis

Yarns	DSC (%)	XRD (%)
PP1	45.21 ± 0.54	32.20 ± 1.71
PP2	43.53 ± 0.86	41.09 ± 1.88
PP3	44.31 ± 2.46	41.75 ± 2.06
PP4	43.20 ± 1.09	32.60 ± 3.23
PP5	43.99 ± 0.81	41.95 ± 2.12
PP1S	55.10 ± 0.87	62.08 ± 1.54
PP2S	53.09 ± 0.55	69.20 ± 1.71
PP3S	54.03 ± 1.35	67.26 ± 0.54
PP4S	50.16 ± 2.25	59.63 ± 0.96
PP5S	52.75 ± 0.98	65.36 ± 0.67
PA	29.72 ± 2.04	23.66 ± 0.38

Firstly, it can be mentioned that, comparing DSC and XRD results, there were some difference between cristallinity values, that evidences a different type of sensitivity of the measuring techniques [174]. Preparation of samples to DSC should cause differences in results. Multifilaments should be positioned in the same direction and in contact with the aluminum pan to provide good thermal contact. After cut, filaments tend to separate and due to the very small dimensions involved, sample preparation becomes difficult to accomplish.

Regarding PP, both DSC and XRD measurements indicated an increase on the crystallinity after post-production stretching. Polymer chains of these yarns are more oriented and, consequently, more stable which promote the increase of crystallinity [175].

The DSC curves of the PP yarns before and after post-production stretching are presented in Figure 39 (a) and (b), respectively, while the PA DSC curve is presented in Figure 39 (c).

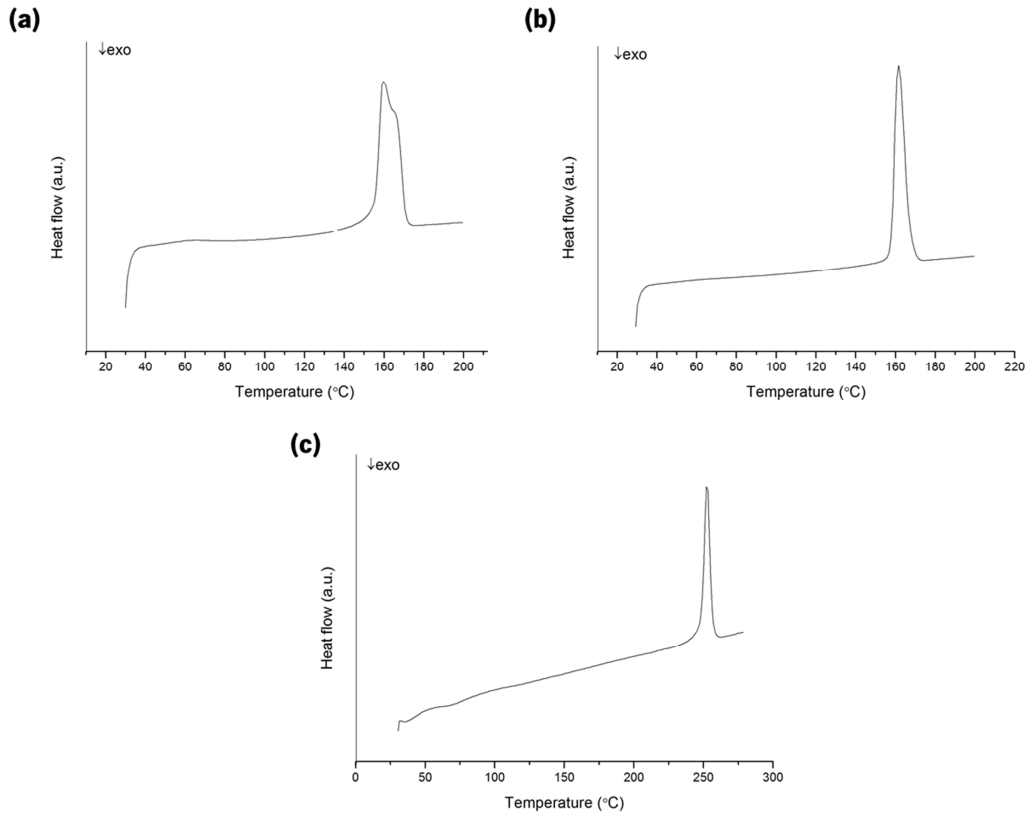


Figure 39: DSC curves: (a) PP 1, (b) PP 1S and (c) PA.

Analyzing Figure 39 (a) and (b), showing the example for PP 1 and PP 1S respectively, it is possible to see differences between the obtained peaks. This variance may be explained by the melting of different sized crystals or disordered crystals. Similarly, the difference between melting behaviors of chain folded crystals and the crystals in more extended chain conformation can origin multiple peaks [176], justifying the small deviation that occurred in PP 1 peak in the melting zone when compared to the one well-defined peak of PP 1S. Regarding PA, it is possible to see that percentage of cristallinity was inferior when compared to PP yarns and by analyzing Figure 39 (c) it can been seen one peak at 252.5 °C, which are similar results presented by other authors [177].

3.2. Contact angle

Contact angle is influenced among others by the material surface. Regarding PP, all type of yarns studied are produced with same raw material; therefore, contact angle was measured in PP 1 yarns since the only difference between yarns is the diameter. Figure 40 shows droplets on PP 1 (a) and PA (b) filament surfaces.

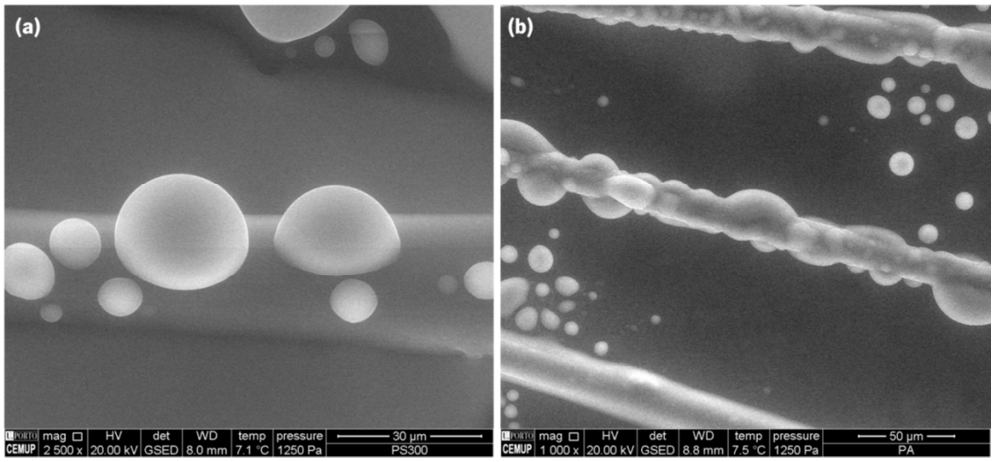


Figure 40: (a) Droplet on PP 1 filament surface; (b) droplet on PA filament surfaces.

The contact angle of PP 1 was found to be 95.24° ± 1.57, proving, as expected, that PP yarns possess a hydrophobic behavior (typically contact angle above 90° are considered hydrophobic) [178]. On the other hand, PA presented a contact angle of 81.97° ± 1.00, presenting higher wettability when compared with PP yarns, due to the hydrophilic nature of the amide functional group [179], confirming that although PA is often thought to be a hydrophobic fiber, in practice, it is moderately hydrophilic [120].

This hydrophobic behavior is extremely important for the development of anisotropic brain phantom. As explained before, natural fibers are known to have hydrophilic behavior and susceptible to biological degradation, while synthetic fibers exhibit a hydrophobic behavior so they are being more stable to degradation. Moreover, the hydrophobicity of the synthetic fibrous materials also plays an important role for the phantom development due to the fact that it allows for creating a restricted movement of water inside the filaments in contrast to hydrophilic fibrous materials, thus mimicking the water movement in the intact myelinated white matter human axons, leading to high values of FA [15,180].

3.3. Moisture content

Table 6 shows the moisture content of PP and PA hollow multifilament yarns.

Table 6: PP and PA hollow multifilament yarns moisture contents

Yarns	Moisture Content
PP 1	1.44 ± 0.14
PP 2	1.56 ± 0.27
PP 3	1.06 ± 0.10
PP 4	1.20 ± 0.14
PP 5	0.90 ± 0.08
PP 1S	1.09 ± 0.06
PP 2S	0.98 ± 0.11
PP 3S	1.13 ± 0.11
PP 4S	1.48 ± 0.16
PP 5S	1.30 ± 0.08
PA	3.56 ± 0.19

Regarding PP hollow multifilament yarns, the chemical structure of PP presents CH and CH_2 groups along its backbone and a CH_3 pendant group. It is a very non polar molecule which means that, inherently, it will be hydrophobic, justifying this low moisture absorption. Usually, moisture content of PP is near zero. Although low, the values of moisture content were higher than those found in the literature [181] due to hollow yarn configuration and the fact that is multifilament rather than a monofilament. This low moisture absorption explains why there were no significant differences between dry and wet properties of PP yarns [182], as it will be seen below, when presenting the results of the tensile test.

Regarding PA yarns, they presented a higher value of moisture content comparing with PP yarns. Due to amide groups bonded to the hydrogen and amorphous regions, water is able to penetrate in the PA structure. In general, all polyamides present certain degree hygroscopic, absorbing moisture when left open to the atmosphere [183]. The results are in accordance with the values presented in the literature [184].

Taking into account the development of brain phantom, low values of moisture absorption are important in order to force water molecules to acquire an oriented flow through of the hollow filaments, which leads to a higher values of anisotropy similarly to the human brain white matter [15,180].

3.4. Friction coefficient

Table 7 shows the friction coefficient between yarn and solid material of the PP and PA hollow multifilament yarns.

Table 7: Friction coefficient of PP and PA hollow multifilament yarns

Yarns	Friction coefficient
PP 1	0.65 ± 0.03
PP 2	0.69 ± 0.05
PP 3	0.71 ± 0.07
PP 4	0.70 ± 0.09
PP 5	0.63 ± 0.07
PP 1S	0.50 ± 0.04
PP 2S	0.44 ± 0.04
PP 3S	0.48 ± 0.05
PP 4S	0.51 ± 0.04
PP 5S	0.38 ± 0.04
PA	0.49 ± 0.09

Friction coefficient can be affected by several parameters such as molecular orientation and the yarn diameter. PP yarns before post-production stretching presented a higher friction coefficient when compared to PP yarns after post-production stretching, and there was no relation inside each group of yarns. Probably, as yarns before post-production stretching have a higher diameter, thus the contact surface area is larger, and then the friction coefficient is higher when compared with group of yarns obtained after post-production stretching. Comparing friction coefficient values between both materials, PA presented a smaller value than PP yarns before post-production stretching, which can be justified by the differences on the linear mass of yarns since friction coefficient of PA was similar to those found on PP yarns after post-production stretching, where values of linear mass between PP and PA yarns are similar. Furthermore, it should be taken into account that PP and PA are different polymers and the fiber material also influences the value of friction coefficient [185].

This property is important in this study due to the fact that fibrous structures with hollow multifilament yarns will be developed to mimic specific configurations of the brain [180] and friction between yarn and solid material can affect manufacturing process of the textile structures. For instance, the number of yarn breakages increase with the increase of yarn friction [185,186].

3.5. Tensile properties

The results of tensile properties, in dry and wet conditions, at room and human body temperature, are provided in Table 8 and Table 9 for PP hollow multifilament yarns.

Table 8: Tensile properties of PP yarns in dry and wet conditions at room temperature

Yarns	Tenacity (cN/Tex)		Elongation at break (%)		Young's modulus (cN/Tex)		Work of rupture (N.mm)	
	Dry	Wet	Dry	Wet	Dry	Wet	Dry	Wet
PP 1	22.76 (0.38)*	22.44 (0.53)	90.87 (9.13)	100.90 (9.00)	113.12 (7.04)	103.65 (2.94)	649.51 (49.36)	725.66 (49.35)
PP 2	21.78 (0.48)	21.58 (0.45)	71.56 (24.52)	82.59 (23.65)	111.03 (4.23)	105.30 (3.81)	497.93 (109.30)	550.06 (110.01)
PP 3	23.21 (0.59)	23.40 (0.74)	73.10 (21.00)	70.31 (28.14)	114.58 (4.21)	115.12 (5.47)	402.47 (50.03)	419.35 (91.21)
PP 4	22.52 (0.42)	22.45 (0.71)	67.30 (15.87)	65.83 (25.01)	118.31 (5.17)	118.35 (3.59)	275.14 (30.65)	317.73 (95.51)
PP 5	25.50 (0.56)	29.42 (1.38)	37.07 (4.59)	101.63 (27.91)	128.94 (6.71)	143.85 (5.24)	126.72 (28.35)	311.83 (86.32)
PP 1S	58.16 (2.02)	52.15 (7.95)	14.48 (1.02)	15.12 (0.91)	506.54 (17.05)	437.41 (34.55)	80.37 (7.16)	74.07 (14.84)
PP 2S	56.03 (0.78)	56.35 (2.21)	20.34 (0.92)	20.51 (1.42)	368.66 (8.02)	387.11 (9.90)	106.12 (6.70)	106.27 (10.10)
PP 3S	59.63 (3.99)	53.92 (3.19)	19.47 (2.04)	17.39 (1.48)	457.16 (17.31)	439.50 (11.07)	74.74 (9.53)	60.14 (9.05)
PP 4S	59.04 (1.91)	58.66 (2.11)	13.70 (0.53)	13.78 (0.49)	508.59 (19.57)	548.60 (15.54)	35.20 (2.23)	35.52 (3.12)
PP 5S	58.08 (1.95)	53.76 (5.09)	19.61 (1.57)	18.18 (2.40)	443.29 (5.64)	462.73 (22.54)	44.94 (5.77)	38.46 (8.35)

* Values within the brackets are the standard deviation.

Table 9: Tensile properties of PP yarns in dry and wet conditions at human body temperature

Yarns	Tenacity (cN/Tex)		Elongation at break (%)		Young's modulus (cN/Tex)		Work of rupture (N.mm)	
	Dry	Wet	Dry	Wet	Dry	Wet	Dry	Wet
PP 1	20.78 (0.42)*	19.73 (0.50)	102.13 (10.11)	98.9 (7.21)	85.15 (4.73)	82.21 (2.59)	620.89 (55.88)	594.64 (40.44)
PP 2	20.36 (0.50)	19.15 (0.30)	114.20 (12.56)	106.2 (13.50)	83.59 (4.12)	80.61 (4.72)	612.16 (48.91)	530.18 (49.09)
PP 3	22.27 (0.36)	21.16 (0.36)	106.80 (13.88)	102.2 (12.33)	97.23 (5.11)	91.30 (4.32)	466.11 (43.35)	422.22 (45.52)
PP 4	21.08 (0.45)	19.21 (0.80)	94.70 (9.80)	91.73 (7.68)	93.08 (4.31)	83.15 (4.10)	288.60 (30.39)	257.59 (24.86)
PP 5	22.88 (0.61)	25.17 (1.50)	55.23 (11.77)	118.10 (17.62)	116.08 (2.14)	107.84 (3.78)	152.40 (14.19)	274.53 (47.30)
PP 1S	53.23 (2.02)	52.66 (2.00)	14.26 (0.74)	14.49 (0.80)	436.85 (9.29)	426.17 (11.05)	69.18 (4.43)	69.33 (6.37)
PP 2S	50.75 (2.21)	49.90 (2.83)	18.65 (1.25)	18.54 (0.81)	353.67 (5.58)	367.04 (6.98)	86.98 (8.64)	81.75 (8.38)
PP 3S	53.77 (3.00)	45.59 (3.53)	16.38 (1.61)	13.99 (1.67)	458.04 (18.06)	441.42 (17.21)	56.92 (9.34)	38.64 (8.12)
PP 4S	54.74 (3.16)	52.69 (2.23)	12.41 (1.14)	12.26 (0.71)	528.10 (14.81)	530.90 (10.55)	30.59 (2.92)	27.16 (2.84)
PP 5S	53.09 (2.13)	49.55 (3.66)	17.43 (1.67)	15.70 (2.08)	430.83 (8.26)	444.02 (16.50)	34.03 (5.04)	28.83 (5.82)

* Values within the brackets are the standard deviation.

Analyzing the tensile test results (Table 8 and Table 9), and in accordance with the results obtained in [187], post-production stretching induced a high tenacity and Young's modulus. On the other hand, elongation at break was lower for post-production stretching yarns. The tensile properties of textile yarns are strongly influenced by the physical structure, which is controlled by the choice of the raw material and the fiber formation conditions. Additional molecular rearrangements, proved by increase of crystallinity (Table 5), were promoted in post-production stretching. After post-production stretching, yarns showed a stiff and brittle behavior (Figure 41 and Figure 42). According to Mukhopadhyay *et al.* [188], post-production stretching cause chain slip through the crystals, sliding and breakage of tie chains and activation of constrained amorphous regions driven by lamellar disintegration. The amorphous phase participates actively in the deformation process together with crystallites during tensile test. For highly crystalline gradient drawn filaments, oriented amorphous layers transmit effectively the stress between crystallites.

Representative tenacity-extension curves for dry condition are presented in Figure 41 and for wet condition in Figure 42. From these results it is possible to see that there was a different behavior between yarns before and after post-production stretching. On the contrary, there were no significant differences between dry and wet conditions at room and human body temperature.

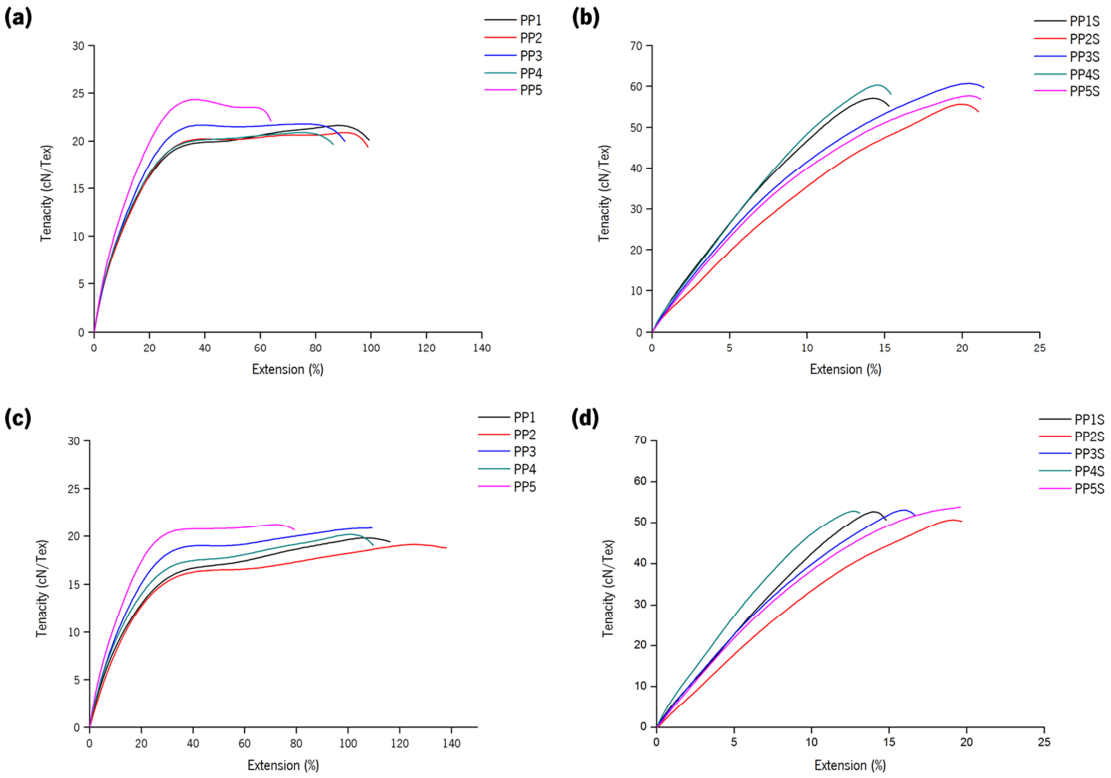


Figure 41: Tenacity-extension curves in dry conditions at room temperature of PP yarns (a) before and (b) after post-production stretching; at human body temperature of PP yarns (c) before and (d) after post-production stretching. Please note for different scales due different reached values.

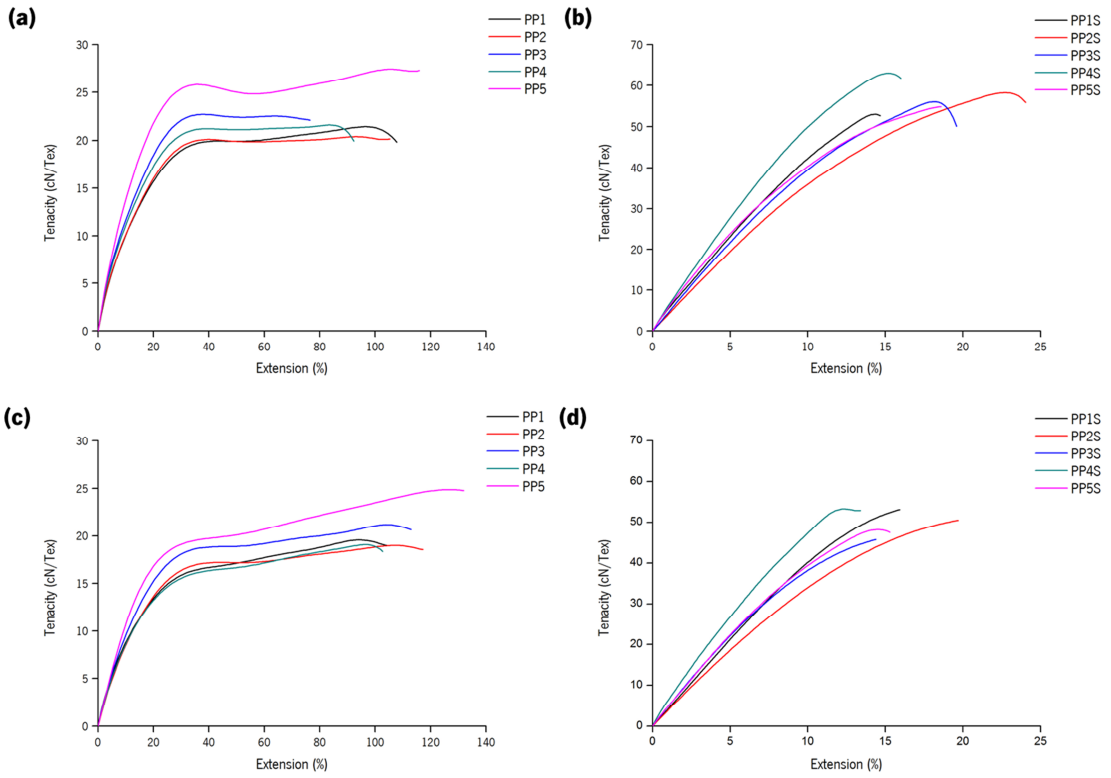


Figure 42: Tenacity-extension curves in wet conditions at room temperature of PP yarns (a) before and (b) after post-production stretching; at human body temperature of PP yarns (c) before and (d) after post-production stretching. Please note for different scales due different reached values.

Tenacity-extension typical curve of PP yarns is presented below (Figure 43).

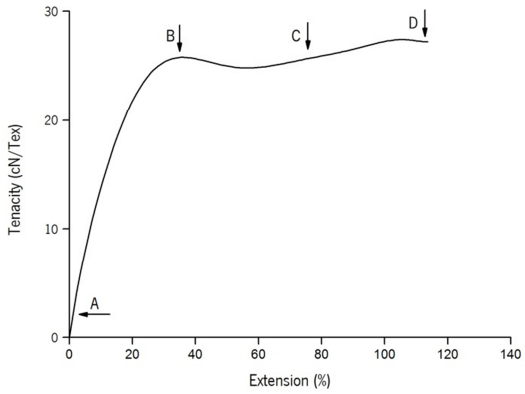


Figure 43: Characteristic points of tenacity-extension curve.

It is possible to recognize the initial high-slope part in which the approximate proportionality between tenacity and extension is held on. There is a distinct instant change in a curve slope, above the limit of proportionality, at certain point A. This point is correlative with some release of freedom and the relative movement of adjacent molecular chain elements preferably in the

amorphous regions. Point B defines the beginning of spontaneous elongation of the yarn without any increase in tensile stress. This behavior is due displacements and rearrangements of molecular chains, crystallites and fibrils. In the end of the curve (point C) stress begins to increase as well, reaching maximum value. In some yarns occurs break of most or all filaments. In other yarns, it does not happen.

Regarding PP yarns after post-production stretching, rearrangements have formed during its high-scale drawing, and point B of Figure 43 does not exist [187,189]. As all yarns are multifilament, zero-twist, their single filaments break gradually. This feature together with the fact that the extrusion process of hollow multifilament yarns is more complex, justifies the occurrence of some variations that affect the tenacity-extension behavior. Consequently, the typical curve points, given Figure 43, can be more or less highlighted, depending of sample behavior.

Comparing room and human body temperature results, it is possible to see that, as expected, the behavior was quite similar because tenacity-extension curves presented similar behaviors. The inexistence of significant differences in dry and wet conditions at different temperatures was expected, because synthetic fibers present resistance to water and to temperature, presenting high melt temperatures [122]. Due to the low human body temperature, the PP hollow multifilament yarns mechanical behavior did not present significant variations in the studied temperature range.

Regarding to work of rupture, yarns before post-production stretching presented the higher values of energy. According to literature [189–191] there is a relationship between work of rupture and linear mass which, in general, was also verified in the studied PP yarns (Table 8 and Table 9). Increasing linear mass, more energy is required to reach the specimen to the breaking load. Some exceptions were observed and previously justified: single filaments break individually and gradually which lead each sample to have a unique behavior. The extrusion process of the filaments and the use of a prototype extrusion line to post-production stretching, may explain some of the differences obtained between samples.

Regarding PA hollow multifilament yarns, the results of tensile properties in dry and wet conditions at room and human body temperature are provided in Table 10 and tenacity-extension curves are presented in Figure 44.

Table 10: Tensile properties of PA yarns in dry and wet conditions at room and human body (HB) temperature

PA	Tenacity (cN/Tex)		Elongation at break (%)		Young's modulus (cN/Tex)		Work of rupture (N.mm)	
	Dry	Wet	Dry	Wet	Dry	Wet	Dry	Wet
Room Temp.	22.77 (2.30)*	23.60 (1.59)	48.07 (7.30)	45.2 (3.65)	189.73 (16.93)	205.58 (44.80)	40.83 (8.98)	36.21 (4.88)
HB Temp.	21.93 (3.96)	22.69 (1.88)	46.24 (8.16)	44.19 (5.54)	267.17 (65.06)	251.58 (35.13)	34.63 (9.95)	36.61 (6.64)

*Values within the brackets are the standard deviation.

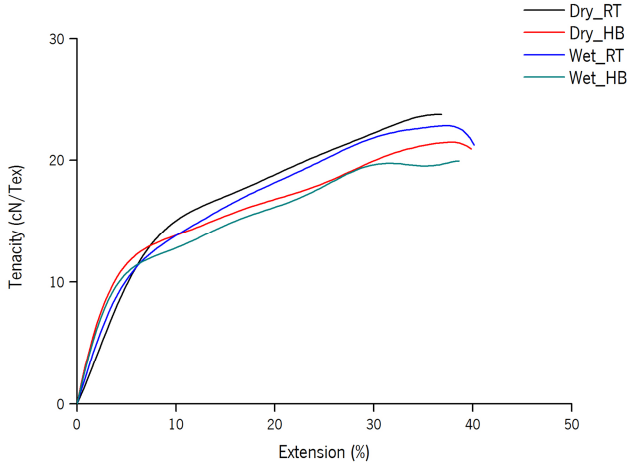


Figure 44: Tenacity-extension curves in dry and wet condition at room temperature (RT) and human body temperature (HB) of PA yarns.

From the values provided in Table 10, one can conclude that there were not significant differences between dry and wet conditions and room and human body temperature. A slight difference is noted regarding the Young's modulus of yarns subjected to human body temperature, assuming higher values comparing with room temperature. This difference is also identified in representative tenacity-extension curves in Figure 44 and is related to the multifilament nature of the yarn without twist. Each filament presents a unique behavior, as explained above for PP. In general, the results obtained are in agreement with the literature [109,120].

3.6. Vertical wicking

Figure 45 shows capillary rise, at room and body temperatures, for the PP hollow multifilament yarns.

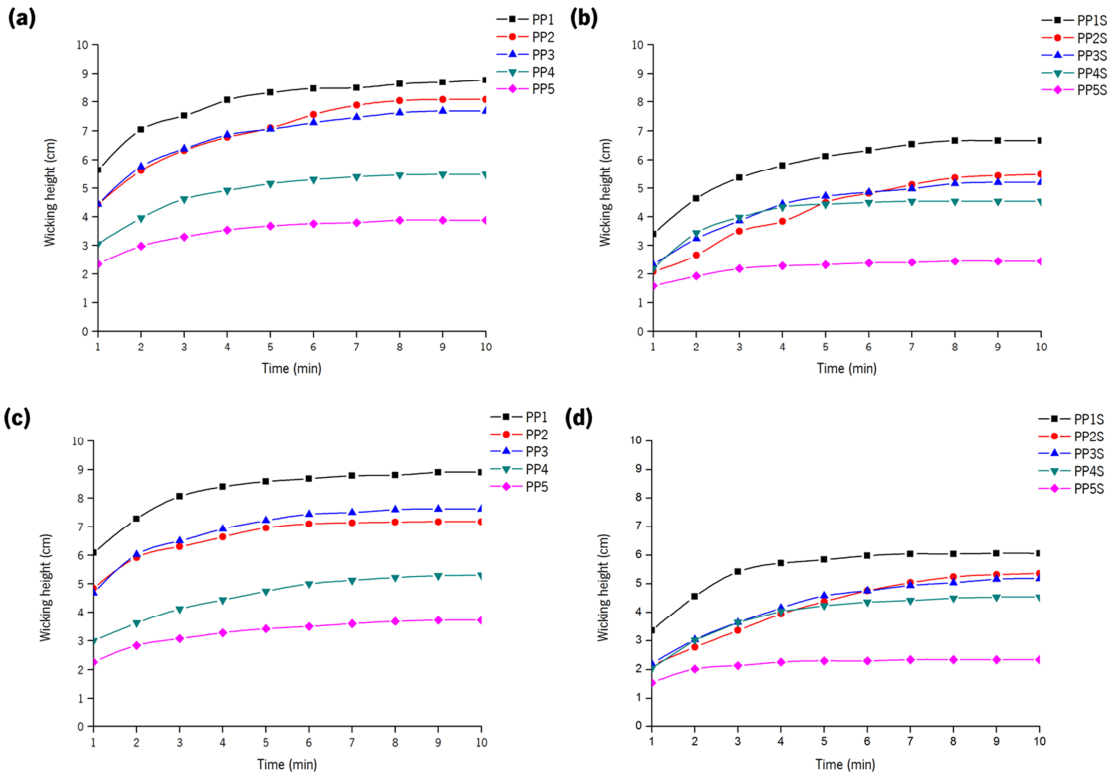


Figure 45: Wicking height at room temperature of PP yarns (a) before and (b) after post-production stretching; at human body temperature of PP yarns (c) before and (d) after post-production stretching.

Analyzing results of PP yarns (Figure 45), it is possible to see that, before post-production stretching, PP yarns reached high capillary rise when compared with yarns after post-production stretching. PP 5 before and after post-production stretching presented the lowest capillary rise. On the other hand, PP 1 before and after post-production stretching presented the higher capillary rise. In the case of hollow filaments, the liquid flows through the yarn both through its hollow passage (inner flow) and interfilament spaces (outer flow) [153]. Increasing the spaces between the filaments and the diameters of the filament itself, the wicking height is increased. These results allow also concluding that there was a fast increase of capillary rise in the first minutes and that temperature did not influence the capillary rise since curves are similar (Figure 45).

Some differences observed in Figure 45 can be explained by filament configurations. As described before, filaments can present irregular geometry due to the swelling effect that occurs in the extrusion process. According to Doakhan *et al.* [192] the heterogeneity of the yarn structure affects the capillary behavior. Furthermore, it should be noted that capillary rise in yarns is difficult to quantify with absolute certainty due to the method of measurement.

Figure 46 shows capillary rise, at room and body temperatures, for the PA yarns. Analyzing results of PA yarns, it is possible to confirm that the temperature did not also influence the wicking effect, since the curves of the wicking height at room temperature and human body temperature are similar. The height reached by PA yarns was low and practically constant during all test compared with PP yarns, which had an increase of height in first minutes.

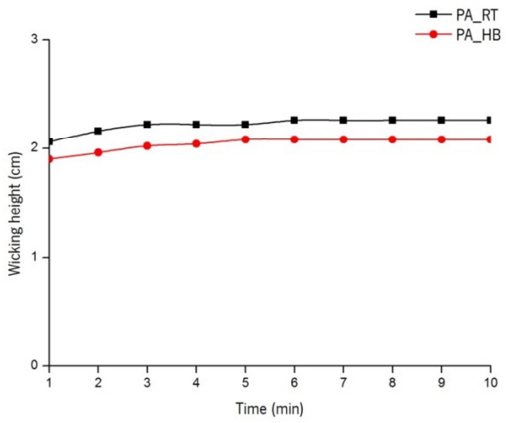


Figure 46: Wicking height at room temperature (RT) and human body temperature (HB) to PA hollow multifilament yarns.

The first minutes of capillary rise will be analyzed in more detail in order to analyze the wickability data by linear regression analysis, which was found to be a very useful tool in earlier studies [134]. Figure 47 and Figure 48 presents the results for PP and PA hollow multifilament yarns, respectively.

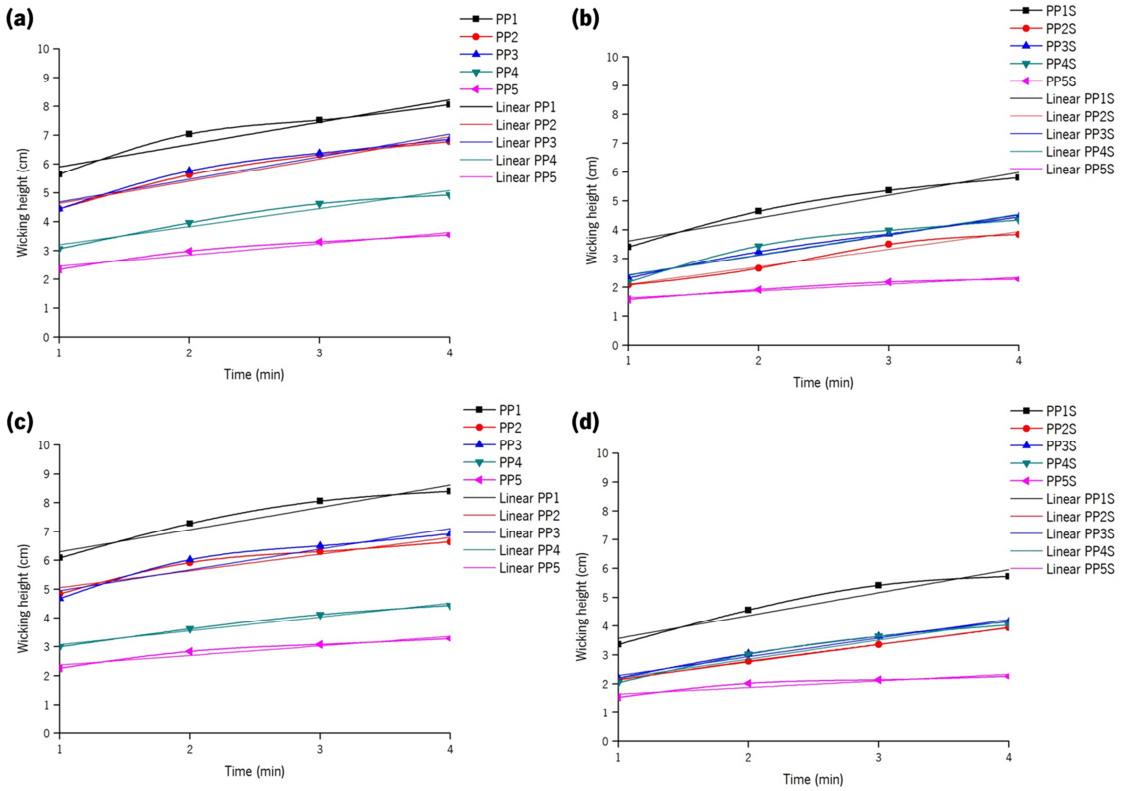


Figure 47: Wicking height and respective linear fit curves of PP yarns at room temperature of (a) before and (b) after post-production stretching; at human body temperature (c) before and (d) after post-production stretching.

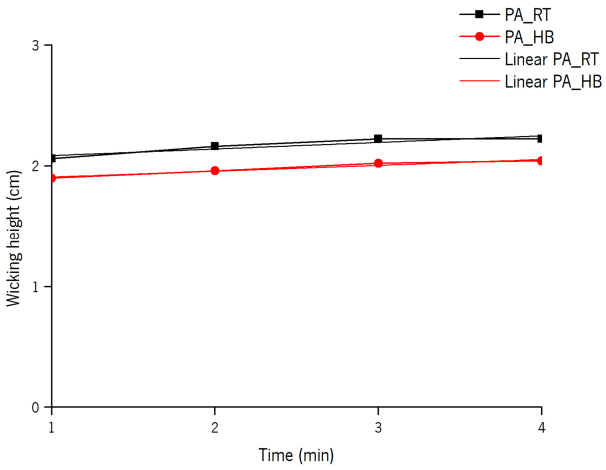


Figure 48: Wicking height and respective linear fit curves at room temperature (RT) and human body (HB) temperature to PA hollow multifilament yarns.

Table 11 shows the regression values and correlation coefficient of linear fit curves (Figure 47 and Figure 48) of PP and PA hollow multifilament yarns. The correlation was found to be good.

Table 11: Regression values and correlation coefficient of the PP and PA yarns at room temperature (RT) and human body (HB) temperature

Yarns	Slope (cm/min)		Intercept (cm)		Correlation coefficient	
	RT	HB	RT	HB	RT	HB
PP 1	0.774	0.774	5.13	5.52	0.892	0.913
PP 2	0.772	0.578	3.86	4.48	0.936	0.869
PP 3	0.788	0.720	3.89	4.23	0.913	0.871
PP 4	0.624	0.482	2.58	2.59	0.933	0.971
PP 5	0.392	0.330	2.06	2.04	0.920	0.896
PP 1S	0.792	0.794	2.82	2.78	0.926	0.908
PP 2S	0.612	0.598	1.49	1.56	0.966	0.999
PP 3S	0.698	0.648	1.72	1.64	0.980	0.981
PP 4S	0.702	0.662	1.73	1.53	0.879	0.944
PP 5S	0.236	0.228	1.4	1.42	0.925	0.805
PA	0.054	0.048	2.03	1.86	0.779	0.940

By Figure 49, it is easier to see the differences between slopes of the curves in the first 4 minutes of the PP and PA yarns wicking tests at room and human body temperature.

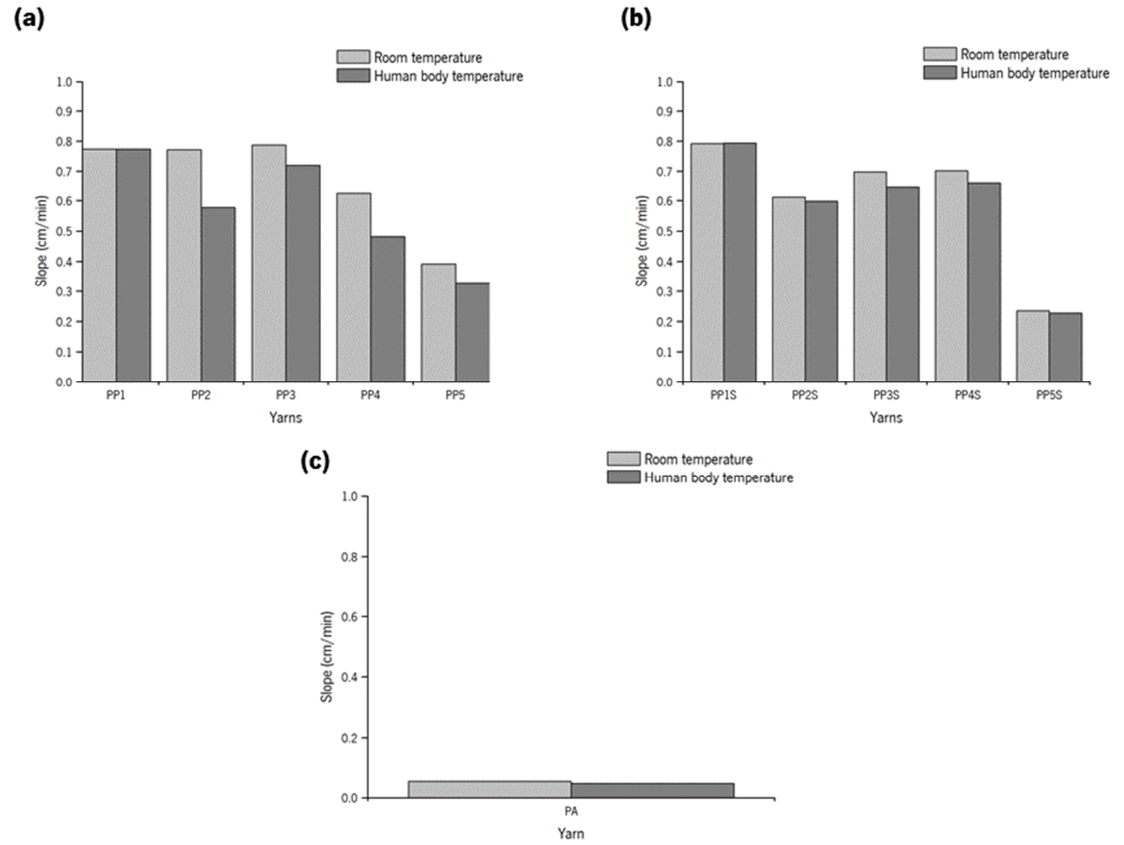


Figure 49: Slope values versus yarns: (a) PP yarns before post-production stretching; (b) PP yarns after post-production stretching; and (c) PA yarns.

Observing Figure 47, Figure 48, Figure 49 it is possible to note that, in general, values of slope and intercept decreased with the thickness reduction, according to values present in Table 11. The higher the slope and intercept, the better is the wickability and vice-versa [134]. It should be noted that there was a considerable difference of slope values between PP and PA yarns.

Comparing both temperatures, there was small differences of the slope and intercept values. This difference is probably due to the irregularity of the yarns, already explained, since surface tension of the water at room and human body temperature, is very similar, so there is no influence in capillary rise [193], and observing the wicking height vs. time curves (Figure 47 and Figure 48) there was not a clear difference between temperatures.

Taking into account the development of the brain phantom, this study of wicking is an important property since it aims to mimic the water motion in human axons, as previously explained in Chapter I. Capillary action can be effectively used for filling the fibers: the inner flow through the hollow spaces mimics the restricted diffusion while the outer flow through interfilament spaces mimics the hindered diffusion. Furthermore, the inexistence of relevant differences in results of

wicking at different temperature conditions is important since brain phantom can be tested both at room and human body temperature. The water motion in yarns, as well as, the scanning of the brain phantom at different temperatures will be explained in more detail in Chapter V.

4. Conclusions

This chapter presented the characterization of PP and PA hollow yarns regarding physical, chemical and mechanical parameters. In literature, there are no studies about the material properties that simulate the human axons of brain white matter, which are used to develop brain phantoms and this research is significant since it can help to a better comprehension about scanning results of the phantoms. Tests about chemical structure to ensure the purity of the materials, wettability, friction coefficient, tensile strength and wicking were done since they are important properties of the materials in the development of anisotropic brain phantom.

PP hollow multifilament yarns showed to be less susceptible to wettability, presenting low water absorption and higher contact angle, superior to 90°. Besides, wicking values reached by PP yarns were higher then compared to PA yarns. Similarly, PP yarns present a range of diameters that allows studying the effect of diameter in brain phantom scanning results. As PP yarns also present more filaments per yarn than PA multifilaments, they can simulate more easily the millions of axons that exist in human brain. Consequently, PP yarns seem to be the most adequate material for the envisaged application. However, PA hollow multifilaments are interesting yarns to study in future in terms of comparison with PP yarns even because PA fibers were already used in brain phantoms, as referred in Chapter I.

Due to the high cost of a MRI scan, it was decided, with the orientations of the Learning Research Development Center of University of Pittsburgh, where phantom was constructed and scanned using MRI, only to use PP 1 in the next chapters due the higher capillary rise when compared with the other PP hollow multifilament yarns.

Next chapter will be focused on the development of fibrous structures using PP hollow multifilament yarns, more specifically PP 1.

CHAPTER IV: Development and characterization of fibrous structures

1. Introduction

An important characteristic when an anisotropic brain phantom based in fibrous materials is developed is related with the yarns orientation and the number of axons that are replied by the yarns. Axons, in generally, grow in a parallel orientation [194]. However, there are complex structures in human brain - an example is the visual system - where axons present a multidirectional orientation. One common gap found in fibrous-based brain phantoms described in literature is the time of production and reproducibility of the models since, in general, they are developed using intensive handwork. In order to avoid the failures verified on the work of Poupon *et al.* [81], whose production of the phantom was extremely difficult and time consuming and, therefore, had a higher cost, conventional approaches employed to manufacture textile structures can be used to build yarn structures. The development of fibrous structures might be a good solution: (a) to mimic the different orientation of human axons; (b) to replicate the large number of human axons; (c) to decrease the time required to manufacture the phantoms; and (d) improving the models reproducibility.

Braiding, narrow weaving and embroidery techniques seems to be the most adequate technologies to meet the requirements of the anisotropic brain phantom based in fibrous materials, allowing to position the yarns in unidirectional, bidirectional and multidirectional arrangements.

Braided fibrous structures result from the interlacing of two or more systems of yarns in the diagonal directions, forming an integrated structure. According to Potluri & Nawaz [195], a traditional braiding machine presents the same principle of a traditional maypole dance, in which the performers dance around a pole holding ribbons tied to the center pole, being divided in two groups: one that travelling around the pole in a clockwise direction while the others travel in an anti-clockwise direction.

It is a relatively simple mechanism to control which has two sets of carriers to support the yarn spools. Each set of carriers rotate in opposite orientations, in the clockwise and counterclockwise. Figure 50 explains this process (spindles that support the spools are represented by the numbers 1 to 16). According to the desired final braided structure, it is possible to control the number of spools. Production of braided structures is relatively simple and do not involve complex yarn

preparation processes, being one of the most cost-effective fabric manufacturing processes [196,197].

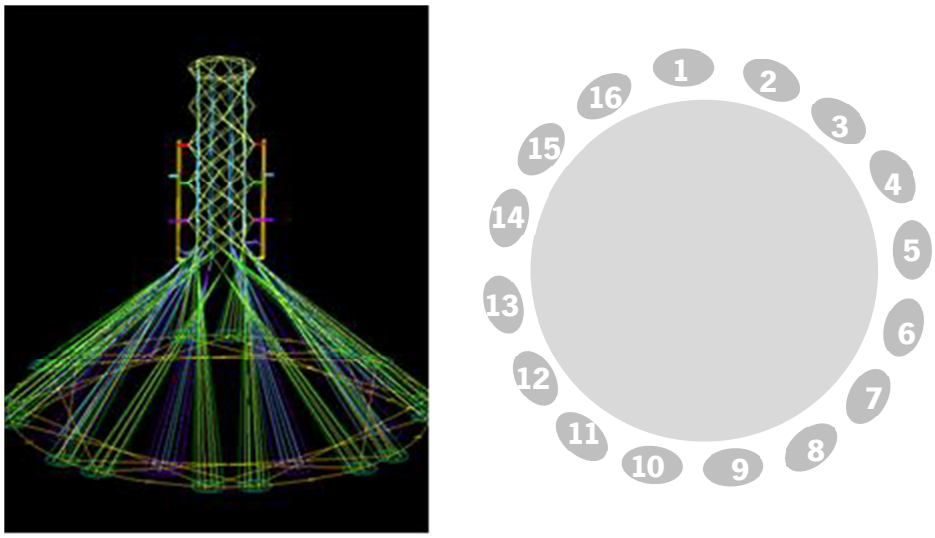


Figure 50: Braiding scheme (left side image) and spindles representation (right side image). Odd spindles rotate in clockwise and even spindles rotate in counterclockwise (adapted from [198]).

It is possible to construct braided structures with materials inserted in the core. Core reinforced braided structures are braided tubular structures presenting, beside two systems of yarns moving helically, a third one that introduces yarns on the braid axial direction [199] (Figure 51).

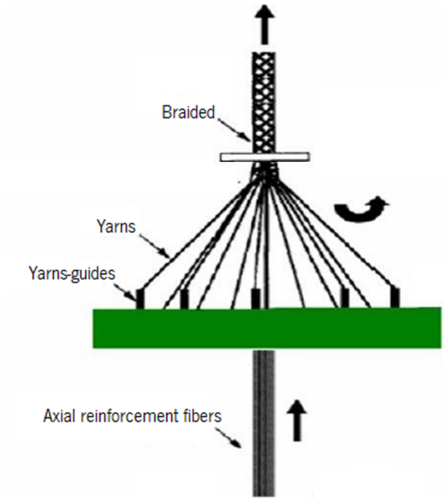


Figure 51: Core reinforced braided structure (adapted from [199]) .

A typically braided structure is presented in Figure 52.

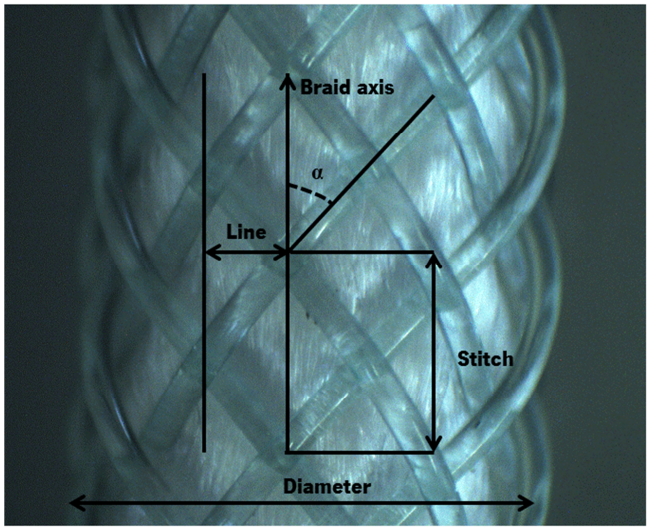


Figure 52: Braided structure.

The braiding angle is the angle between the longitudinal axis (braiding axis) and the direction of insertion of braiding yarns. On the other hand, the diameter of the braided structure is length of the straight line connecting the two edges passing through the braiding center. Stich is one repeat of braiding structure along the braid axis while line can be described as one repeat of braiding structure perpendicular to braiding axis. This dimension can vary depending on the diameter of the yarns of the braided structure, the diameter of the axial structure and the take-up speed [196,198].

Braiding angle is the most important parameter that determines the cover factor of braided structure and it is strongly influenced by take-up speed. With increase of take-up speed, braiding angle decreases, creating a closely packing structure. On the other hand, an opened braided structure is created by the decreasing of take-up speed, increasing the braiding angle. This is a key point to change the elasticity of the braided fibrous structure, according to the application requirements [198,200].

Regarding narrow fabrics, they are usual woven fabrics with widths up to 120 cm. The difference is only in the weaving machine [201]. The weaving operation, done in weaving looms, is the orthogonal intersection of two systems of yarns, the warp (longitudinal threads) and weft (lateral threads), to produce a fabric (Figure 53) [202].

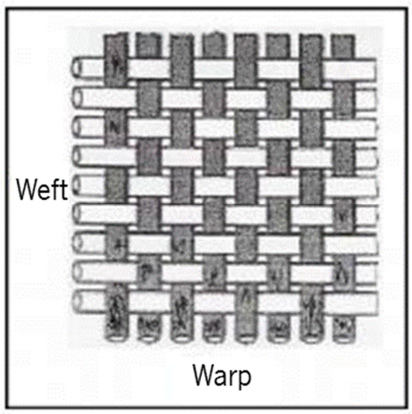


Figure 53: Weft and warp representation.

Individual warp and weft are called ends and picks and their interlacement produces a coherent and staple structure. Weave is the repeating unit of the interlacement. It can be created several patterns according way as yarns are inserted. The weave patterns are extremely important because they determine the product end application, since appearance, flexibility, etc. depend of these weave patterns and of the type of yarns used in weaving production. Plain weave presents the simplest repeating unit of interlacement and maximum possible frequency of interlacements. A grid is used to represent a weave, where warp is represented by vertical lines and weft by horizontal lines. The crossing of an end and a pick is represented by each square. Crosses or marks are used to indicate where the warp thread is uppermost. Only warp floats or lifts are indicated by a mark: a blank square indicates that the weft thread is placed over the warp. [202–204].

Other useful method for development of anisotropic brain phantoms is embroidery technique since it allows applying yarns to a textile substrate in a defined pattern [205]. Standard embroidery, tailored fiber placement (TFP) and chain stitch embroidery are three types of embroidery found in literature. Standard embroidery is a two-thread system. Firstly, the pattern is defined and transferred to a software which is, posteriorly, converted into embroidery machine code. The needle, or upper, thread is stored on a conical bobbin that forms the stitches on the underside of the garment. The bobbin, or lower, thread holds the top embroidery thread to the garment. An embroidery frame is used to hold under tension the basic fabric. The frame is moved along x and y-directions, creating the programmed pattern. The needle punches through the fabric, interlacing the upper thread with the bobbin thread by means of a rotating gripper, placed below the basic fabric. Standard embroidery allows creating complex pattern and it is an

accurate and reproducible process since it is computer-controlled. In turn, TFP is a three-thread system. In addition to the top yarn and the bottom yarn, a functional yarn is introduced. On the textile substrate is placed the roving and across this is created a zigzag stitch by the needle that punches left and right of the roving into the textile substrate. The roving is fixed by the top and bottom sewing threads. As the roving is never penetrated by the needle, no damage is induced in the yarn (Figure 54) [205,206].

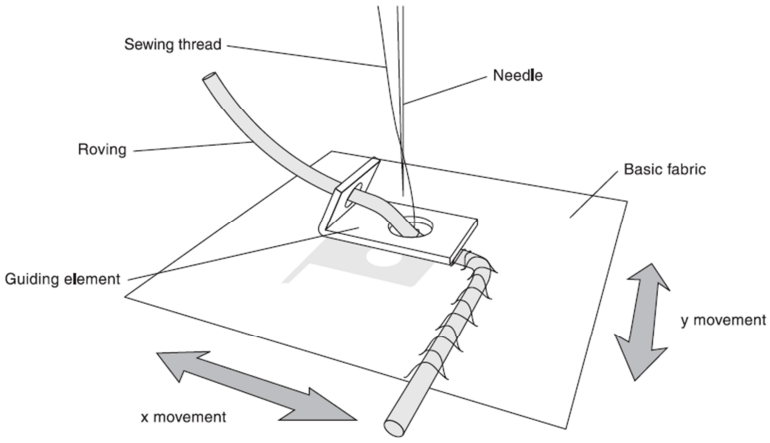


Figure 54: Tailored fiber placement [206].

Chain stitch embroidery is usually used for kettle and moss embroidery. The machine that creates this type of embroidery has a one-thread system. The needle pulls the thread out from under the needle, during it goes through the carrier material. On the upper side of the carrier material is created a loop due the rotary motion of the needle. A moss-like surface occurs with repetitions of this pattern [205].

This chapter presents a novel study about the development of fibrous structures to apply in anisotropic brain phantoms. Three types of fibrous structures using PP hollow multifilament yarns, more specifically PP 1, were developed: braided structures, narrow fabrics and embroidered structures aiming to (1) create oriented fibrous structures (unidirectional, bidirectional and multidirectional orientations); (2) mimic the large number of human axons that there is in human white matter; (3) improve the production of phantoms in relation to manufacturing time and, consequently, cost of the final product; and, (4) reproducibility. Characterization of the structural configuration, mechanical properties and wicking of the fibrous structures was also presented and discussed in this chapter. As observed in Chapter III, there were no significant differences in the results between test conditions (dry/wet; room and human

body temperature). Consequently, in this chapter, characterization tests were done at dry conditions and room temperature.

2. Materials and methods

According to the explanation presented in the previous chapter, PP hollow multifilament yarns, specifically PP 1 was used in this chapter to develop fibrous structures. Braiding, narrow weaving and embroidery technologies were used to produce the fibrous structures.

2.1. Braided structures

Braiding technique allows the introduction of parallel yarns in the braided core yarn system using appropriate braiding technique. In order to fit the requirements of the application, braided structures should be flexible, allowing an easy handling. Braided structures create a unidirectional orientation to 0° of the PP hollow multifilament yarns.

2.1.1. Braiding conditions

In order to produce the braided fibrous structures, a vertical braiding machine TRENZ® with 16 bobbins was used.

Two types of braided structures were developed (Figure 55):

- Braided structures with axially reinforcing PP hollow yarns (Figure 55 (a));
- Braided structures with axially reinforcing braids, which are in turn axially reinforcing PP hollow yarns (Figure 55 (b)).

PA monofilament (diameter of yarn = 0.3 mm) was used to construct the braided structures (specified as braid filaments in Figure 55 (c)). The choice of this monofilament was due to the fact that: (1) PA is a synthetic fiber and (2) PA yarn is a monofilament, not allowing the water motion between interspaces like multifilaments. In other words, with this arrangement, only PP yarns contribute for the water motion. PA monofilament served as a support to hold in the PP hollow multifilament yarns.

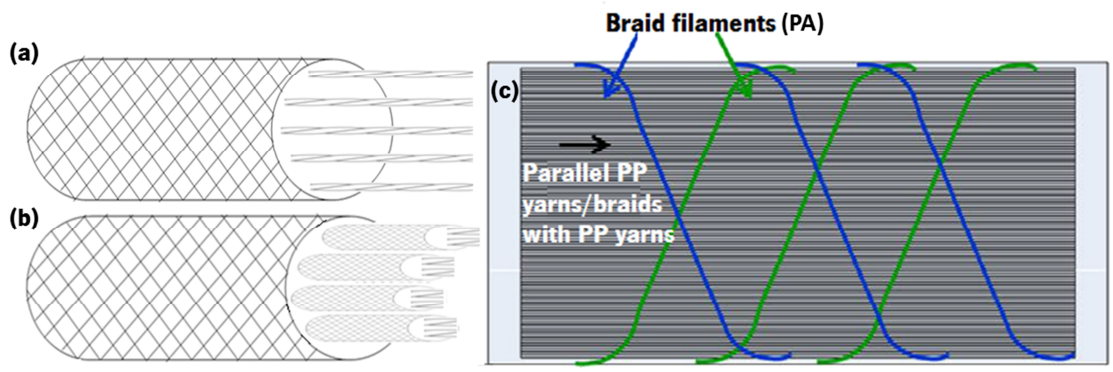


Figure 55: Schematic diagram of produced braided structures: (a) braids with axially reinforcing PP hollow yarns; (b) braids with axially reinforcing braids; (c) orientation of yarns/braids in the core of braided structures.

In the case of braided structures with axially reinforcing PP hollow yarns, 16 PA filaments were used in its production to hold the PP yarns. On the other hand, regarding circular braids with axially reinforcing braids, 10 PP hollow yarns were used in the core of each circular braid used in the axial reinforcement and 8 PA yarns were used (to hold the PP yarns) to produce the braid which is used as axial reinforcement. 16 PA yarns were also used to produce the outside braided structure, which holds the core formed by braided structures. The number of PP yarns inside of the braided structures varies from 40 to 100 yarns (40, 60, 80 and 100 yarns). This range was established in accordance with the orientations of the Learning Research Development Center of University of Pittsburgh, where the anisotropic brain phantom was constructed. Figure 56 summarizes the structures produced using braiding technology.

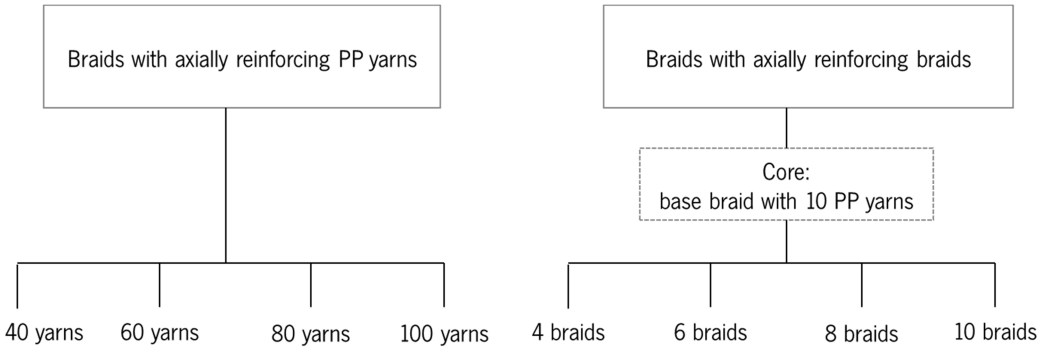


Figure 56: Scheme showing the production of different types of braided structures.

Figure 57 shows the production of braided structures. In this specific case, it shows the production of a braided structure with axially reinforcing PP hollow yarns.

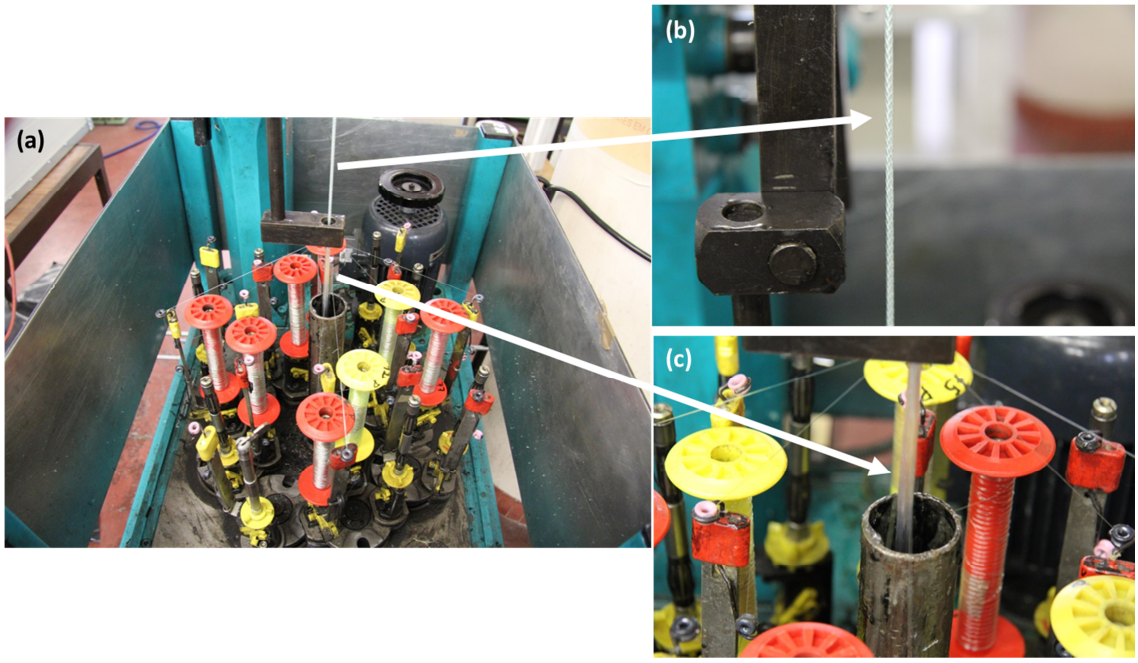


Figure 57: Braiding process of braided structures with PP yarns in the core: (a) vertical braiding machine TRENZ®; (b) braided structure; (c) PP hollow yarns (core of the braided structure).

The reproducibility of the braided structures is important to assure the phantom reproducibility and, consequently, the results reproducibility. Since in the braided structures with axially reinforcing PP hollow yarns, hollow yarns are inserted manually in the core, this could induce differences in the tension of the yarns during the insertion in the core. For this reason, it was decided to develop the two types of braided structures with: 1) axially reinforcing PP hollow yarns; and, 2) axially reinforcing braids, which are in turn axially reinforcing PP hollow yarns. From these two, the braided structures with axially reinforcing braids allow better tension control during the insertion of the core. The processing parameters are the same for all braided structures.

2.1.2. Characterization of the braided structures: structural properties

In order to simplify the movement of water in braided structures, essential to mimic human axons, an opened braided structure is desirable. As previously explained, braiding angle increases as the take-up speed decreases. This relationship is given by Equation 4.

$$\alpha = tan^{-1}(\frac{WRc}{V})$$

Equation 4

Where,

α – braiding angle (rad);

W – angular speed of bobbins (rad/s);

Rc – core radius (cm);

V – take-up speed (cm/s).

Braiding angle was measured theoretically and by image analysis using a stereomicroscope with camera to collect images and Image J® was used to measure the angles.

Diameter is other important structural property of braided structures as it the key point to the mechanical behaviour (Figure 52). In the specific case of brain phantoms, it is necessary to take into account the relationship between diameter and braiding angle, since, ideally, it is intended to use braided structures with a braiding angle which helps the water motion but, at the same time, with small diameters to simulate the micro-dimensions of the human brain axons.

The take-up speed was chosen according to a previously study done by Rebelo *et al.* [207] and according to the need to keep the final braided structure functional to the handling. Therefore, the take-up speed was 1.44 cm/s and angular speed of bobbins was fixed at 7.075 rad/s.

2.1.3. Tensile test

Tensile tests were carried according to NP EN ISO 2062:1997 standards [167], using a H100KS Hounsfield Universal Testing Instrument and a load cell of 100 kN. A 100 mm gauge length and 100 mm/min speed were used. Preliminary tests were done to observe the behavior of the braided structure. It was possible to observe that there was slippage between the core and sheath, and the structure broken at the ends, near of the grips. Therefore, it was decided to apply epoxy resin (Biresin® CR83) in the ends of the braided structures since the epoxy matrix holds the various components (core and sheath) of braided structures together, enabling them to act as a single structure.

2.1.4. Vertical wicking

The process described in Chapter III was applied to the braided structures.

2.2. Narrow fabrics

In order to produce the narrow fabrics based in PP hollow multifilament yarns, a narrow weaving Müller® machine, model NHJM2 53, was used (Figure 58). Narrow fabrics allow positioning yarns in bidirectional orientation to 0° - 90°.

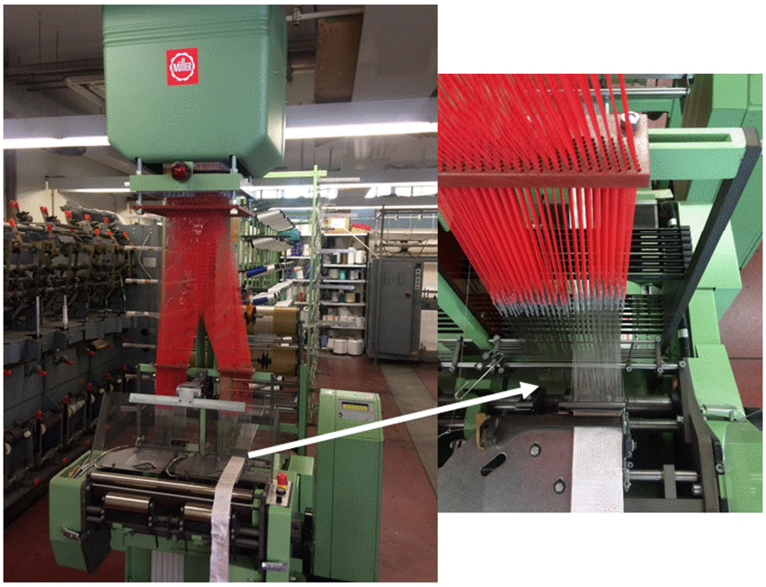


Figure 58: Narrow weaving Müller® machine model NHJM2 53.

PP hollow multifilament yarns were used in the warp, while 3 different yarns were used in the weft:

- Two types of PES with different linear densities, named PES 1 with 16.8 tex and PES 2 with 34 tex. The choice of PES yarns (PES 1 and PES 2) was due to: (1) PES to be a synthetic fiber and (2) availability of the same material with different linear densities in the textile laboratory where narrow fabrics were produced. PP hollow yarns (warp) are placed in parallel orientation to 0°, mimicking the axonal growth, which presents a parallel orientation;
- PP hollow yarns, being, in this case, warp and weft formed by the same fibrous material. The development of the narrow fabrics constituted of PP hollow yarns aims to mimic crossing zones of the human axons. The yarns are positioned to 0° - 90°.

Three types of weave patterns of the machine software were chosen: plain, satin and jacquard, all illustrated in Figure 59. The aim was to create narrow fabrics with different openings that could be influence in water motion that occurs in the anisotropic brain phantom.

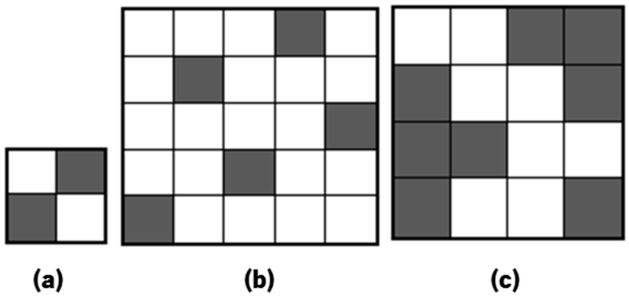


Figure 59: Weave patterns: (a) plain; (b) satin; (c) jacquard. Weave patterns have a double weft insertion.

Figure 60 summarizes the structures produced using narrow weaving technology, which warp yarns is the same for all structures (PP 1) and weft yarn varies (PES 1, PES 2 or PP 1) as explained before.

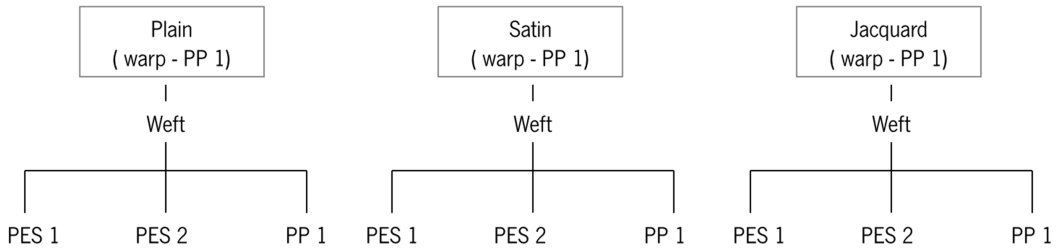


Figure 60: Scheme showing the production of different types of narrow fabrics.

2.2.1. Characterization of the narrow fabrics: structural properties

Analysis on the number of yarns in the weft and the warp directions were carried out based on NP EN ISO 1049-2:1995 standard, using a counting glass [208]. In the woven fabrics, the warp yarns are typically referred by "ends" and the weft yarns are typically referred by "picks" [209].

Regarding the mass per unit area, ASTM D 3776 – 96 [210] standard was used. Cover factor which indicates the extent to which the area of a fabric is covered by one set of threads was obtained according Equation 5 [211]:

$$K_x = \frac{threads/cm}{10} \times \sqrt{tex}$$

Equation 5

Where,

K_x – cover factor, being "X" representative of the warp or weft cover factor.

For any fabric warp and weft cover factors are important parameters. The fabric cover factor is given by the Equation 6 [211,212]:

$$Fabric\ cover\ factor = K_1 + K_2 - \frac{K_1 K_2}{28}$$

Equation 6

Where,

K_1 – warp cover factor;

K_2 – weft cover factor.

Thickness of the fabrics was measured based on NP EN ISO 5084:1999 standard [213], using a Mitutoyo No. 2046F with a contact area of 78.5 mm^2 and a foot pressure of 18 Pa.

2.2.2. Tensile tests

Tensile tests were carried out based on NP EN ISO 13934-1:2001 standards [214], using a H100KS Hounsfield Universal Testing Instrument and a load cell of 2.5 kN. Gauge length was 200 mm and the tests were carried out at 100 mm/min. Tensile tests were only done in warp direction in accordance with the orientations of the Learning Research Development Center of University of Pittsburgh, where brain phantom was constructed, since any load applied to the narrow fabric will be applied in that direction.

2.2.3. Vertical wicking

The process described in Chapter III was applied to the narrow fabrics.

2.3. Embroidered structures

Embroidery technique allows creating complex patterns since it is supported by computer software as previously explained. In the present study, the application of this type of technology allows guiding the yarns in several orientations, according the pattern that is intended to reproduce.

One of the complex human brain patterns is the visual system as it is possible to see in Figure 61.

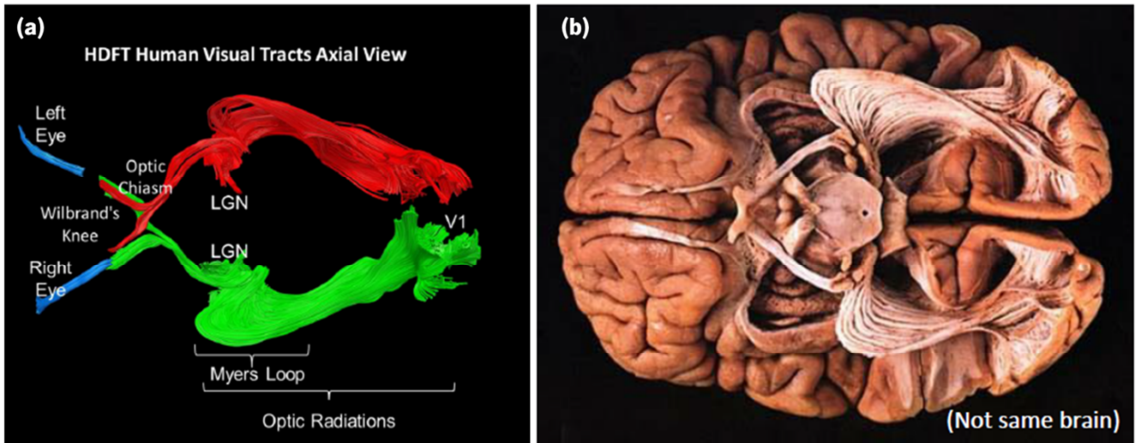


Figure 61: (a) Human visual tracts obtained by HDFT and (b) visual system of the human brain (Images provided by the Walt Schneider Lab, USA).

Therefore, embroidery technique was chosen to mimic the visual system of human brain, specifically the optic chiasm which is the part of the brain where the optic nerves are partially crossed (Figure 61).

Two types of coated textiles (supplied by Endutex) where used as substrate to PP hollow multifilament yarns. The composition of these substrates is below:

- 27% PES and 73% polyvinyl chloride (PVC) and 570 ± 50 g/m^2;
- 30% PES and 70% PVC and 300 ± 30 g/m^2.

Embroidered structures were produced by Bordados M.A. & Filhos Ltd. (Portugal), using a multi-head automatic embroidery machine SFW/TA-WL 910-120 (Figure 62).

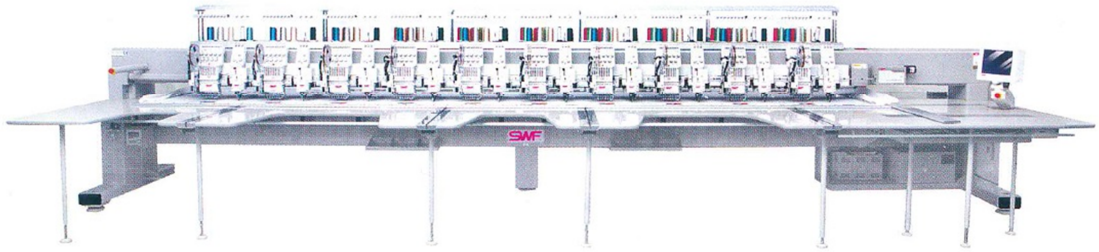


Figure 62: Multi-head automatic embroidery machine SFW/TA-WL 910-120 (Image provided by Bordados M.A. & Filhos Ltd., Portugal).

The use of embroidery technology aimed to provide alternative yarns structures, suitable for the simulation of complex patterns of the human brain and no further characterization studies were performed.

3. Results and discussion

3.1. Braided structures

Figure 63 presents two types of braided structures produced in this work, both with 100 PP hollow yarns in the core and PA monofilament to hold the PP hollow multifilament yarns.

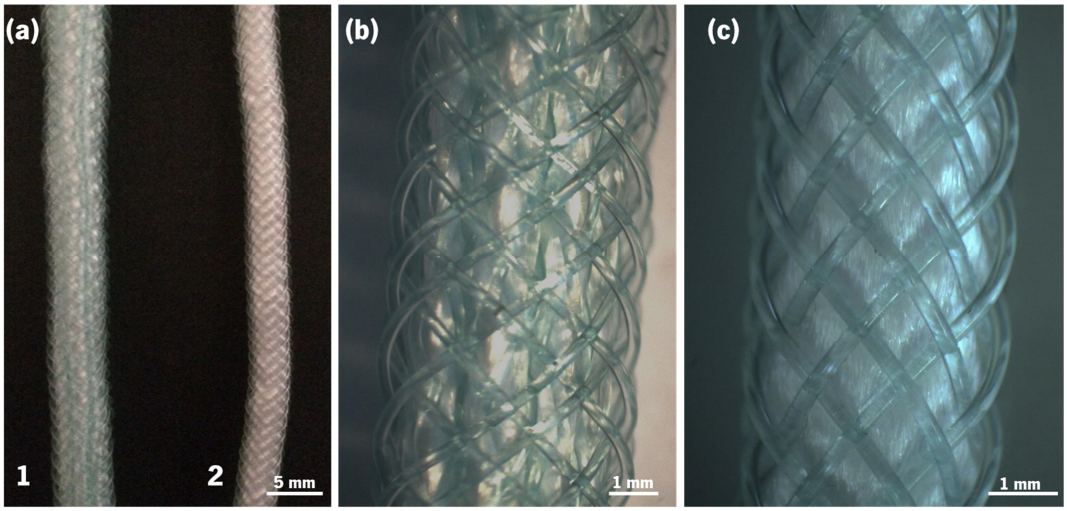


Figure 63: Examples of the braided structures produced: (a) 10 braids in the core -1- and 100 yarns in the core -2-; (b) 10 braids in the core (magnification); (c) 100 yarns in the core (magnification).

3.1.1. Structural properties

Table 12 presents values of the braiding angles predicted by Equation 4 and measured by imaging analysis. Furthermore, it is presented the diameter and linear mass of the braids.

Table 12: Structural properties of braided structures according with the core

Core	4 braids	6 braids	8 braids	10 braids	40 yarns	60 yarns	80 yarns	100 yarns
Measured braiding angle (°)	35.28 (2.98)*	40.30 (4.84)	42.14 (2.61)	44.63 (2.87)	28.61 (1.75)	34.52 (1.69)	38.70 (4.25)	40.28 (3.61)
Predicted braiding angle (°)	35.88	40.26	44.14	49.18	25.99	29.79	34.15	37.72
Diameter (mm)	3.55 (0.05)	4.06 (0.07)	4.56 (0.07)	5.32 (0.09)	2.59 (0.03)	2.94 (0.05)	3.37 (0.06)	3.76 (0.08)
Linear mass (g/m)	55.980 (0.011)	77.040 (0.007)	97.100 (0.007)	120.340 (0.006)	29.060 (0.006)	35.760 (0.003)	43.700 (0.004)	50.680 (0.013)

*Values within the brackets are the standard deviation.

Assuming that the core of the braided structures is perfectly circular and without air, like a mandrel, an approximation to the core radius can be devised to predict the braiding angle. For the particular of braided structure with 10 braids in the core, the core radius was calculated as follows:

- Diameter (mm) = 5.32
- Thickness of PA yarns (mm) = 0.3
- Core radius (mm) = $\frac{5.32 - 2 \times 0.3}{2}$ = 2.36

The predicted braiding angle was found applying Equation 4.

Figure 64 shows a comparison between measured and predicted braiding angles.

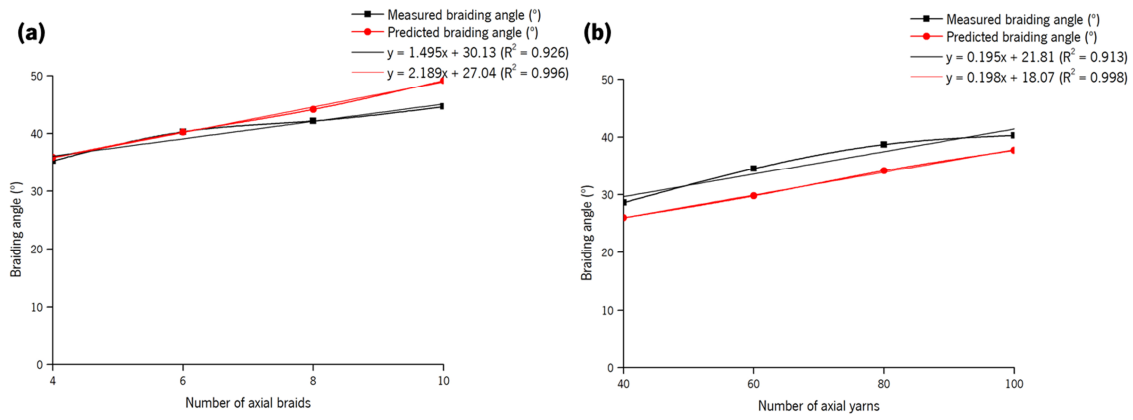


Figure 64: (a) Comparation between measured and predicted braiding angles: (a) braided structures with axially reinforcing braids; (b) braided structures with axially reinforcing yarns.

As per Equation 4, for the same production parameters, increasing the number of axial braids or yarns, there is an increase of braiding angle, which is clear both in Table 12 and Figure 64. Furthermore, by analyzing Figure 64 it is possible to notice that the values of the measured braiding angles of braided structures with axially reinforcing braids were lower comparing with values of predicted braiding angles (except for the braided structure with 6 braids in the core). On the other hand, braided structures with axially reinforcing yarns possessed values of measured braiding angles higher when compared to the values of predicted braiding angles. These differences should be explained by production process and variables of the equipment, impossible to control as the tension applied in core material during insertion. However, in both situations the differences between measured and predicted braiding angles were minimal.

Diameter and linear mass of braided structures increased with the increase on the number of axial yarns or braids (Table 12), as expected [215].

Regarding the final application of this work (brain phantom), the braiding angle can influence the water motion. It is expected that braided structures with high braiding angles allow a better and faster water flow comparing with braided structures with low braiding angles since high braiding angles create a more opened structure when compared to braided structures with low braiding angles.

3.1.2. Tensile properties

Table 13 presents the results obtained within the tensile tests emphasizing the breaking force and extension at failure for different braided structures.

Table 13: Breaking force and extension at failure for different braided structures

Core	4 braids	6 braids	8 braids	10 braids	40 yarns	60 yarns	80 yarns	100 yarns
Breaking force (N)	1428 (24)*	1907 (167)	2393 (160)	3246 (90)	449 (40)	582 (50)	701 (20)	836 (31)
Extension at failure (%)	34.2 (1.7)	40.5 (2.9)	32.7 (6.4)	35.1 (8.4)	24.4 (0.6)	25.3 (1.5)	28.4 (0.4)	30.2 (2.6)

*Values within the brackets are standard deviations.

Representative force – extension curves of the braided structures are shown in Figure 65.

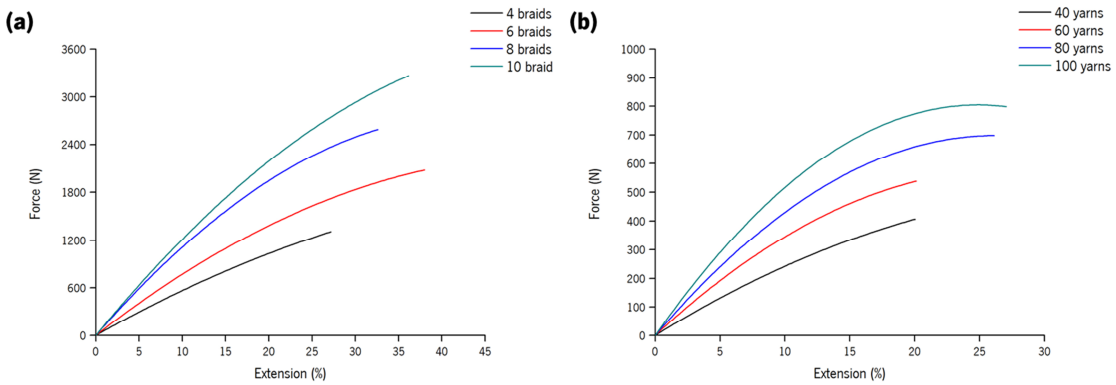


Figure 65: Force – extension curves for: (a) braided structures with axially reinforcing braids; (b) braided structures with axially reinforcing yarns (Please note the different graphic scales).

Analyzing Table 13 and Figure 65, it is possible to confirm, as expected, that braided structures with axially reinforcing braids presented higher values of breaking force when compared to braided structures with axially reinforcing yarns. Furthermore, the increase of axial reinforce (braids or yarns), led to an increase the breaking force value.

A typical tensile behavior of a core reinforced braided structure present a usual initial stage where occurs a rearrangement of internal tensions in the set: core and braided structure (Zone I, Figure 66) [198]. This typical behavior is not reflected in Figure 65, since the load is taken immediately by the straight axial braids or yarns, resulting in instant increase of load with extension [215]. After, the reinforcement fibers are completely straight and the load is borne by the core reinforced fibers. There is a significant increase in the load required to stretch the reinforcement fibers. This is the elastic zone (Zone II, Figure 66). Zone III in Figure 66 represents the plastic deformation zone.

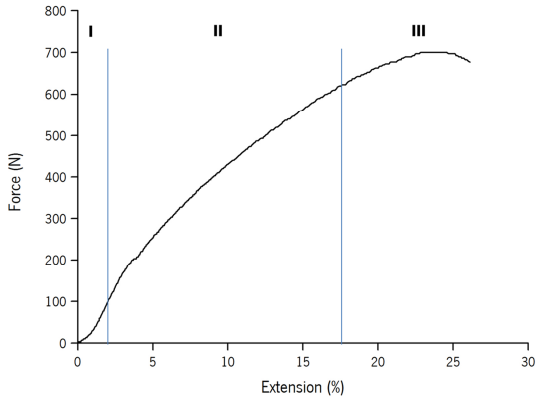


Figure 66: Force-extension curve of a core reinforced braided structure.

During the development of an artificial phantom, it is important that materials support the handling and production process forces. The elastic zone occurred until, approximately, 20% of extension for the braided structures with axially reinforcing braids (Figure 65 (a)) and, approximately, 15% of extension for the braided structures with axially reinforcing yarns (Figure 65 (b)). After that, plastic deformation occurred, where the deformation in the structure is permanent. In the case of the application, in this plastic zone the deformation occurs in localized regions, creating non-uniformity in the yarns. It should be taken into account that specifically for the application on brain phantoms, braided structures will not be subjected to such high forces that lead to the rupture.

The relationship between the breaking load and the number of reinforcing braids and yarns is shown in Figure 67. It can be noticed that the breaking force of these braided structures increased quasi-linearly with the number of axial reinforcement, as expected. The load carrying capability of the structure improved with the number of yarns in the axial direction [215].

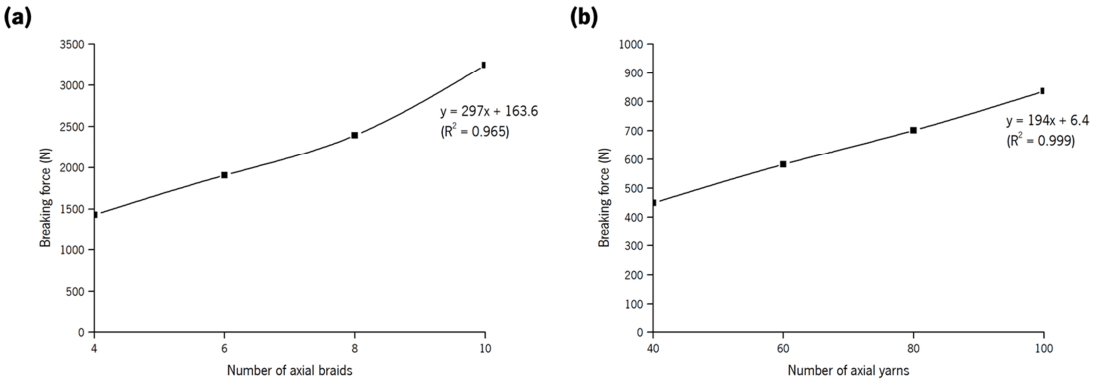


Figure 67: Relationship between breaking force and (a) number of axial braids and (b) number of axial yarns.

3.1.3. Vertical wicking

Figure 68 presents the results obtained in the vertical wicking tests for the braided structures. As shown, the behavior of both braided structures axially reinforced with braids or with yarns was similar and there were no significant differences according with the number of braids or yarns in the core. As all braided structures presented, approximately, the same diameters and they were produced with same yarn inside (PP 1), this similarity was expected.

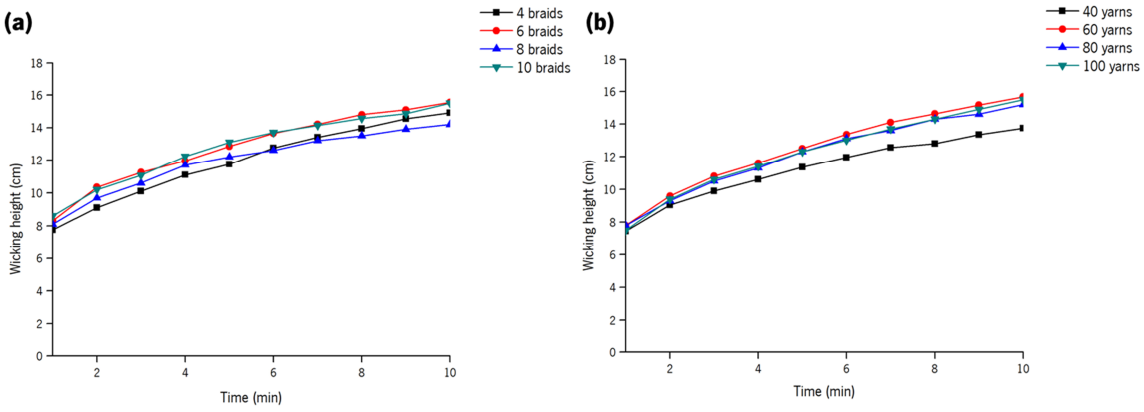


Figure 68: Wicking height of: (a) braided structures with axially reinforcing braids; (b) braided structures with axially reinforcing yarns.

As the curves possessed almost linear behavior comparing, for example, with the curves of yarns presented in Chapter III, the linear fit for each braided structure during the first 10 minutes of the wicking process was calculated. Table 14 shows the regression values and correlation coefficient of linear fit. The correlation was found to be good.

Table 14: Regression values and correlation coefficient of the braided structures

Core	4 braids	6 braids	8 braids	10 braids	40 yarns	60 yarns	80 yarns	100 yarns
Slope (cm/min)	0.786	0.750	0.628	0.719	0.653	0.832	0.790	0.823
Intercept (cm)	7.61	8.67	8.51	8.84	7.68	7.95	7.85	7.71
Coefficient of correlation	0.973	0.943	0.920	0.938	0.951	0.961	0.960	0.961

The values presented show that there were no significant differences between different braided structures, as expected and confirmed by the analysis of Figure 68.

3.2. Narrow fabrics

Plain, satin and jacquard woven fabrics, produced with PP 1 in warp and PES 2 in weft are shown in Figure 69.

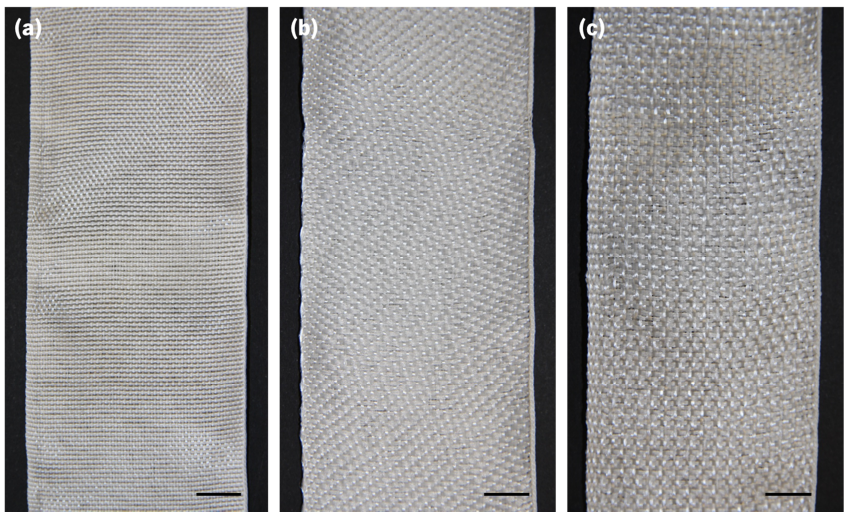


Figure 69: Narrow fabrics produced with PP 1 (warp) and PES 2 (weft): (a) plain; (b) satin; (c) jacquard. Scale bars represent 1 cm.

3.2.1. Structural properties

Structural properties of the narrow fabrics produced are listed in Table 15.

Table 15: Structural properties of narrow fabrics

Weave pattern	Narrow fabrics	Ends x Picks/ unit area	Thickness (mm)	Fabric cover factor	Weight (g/m^2)
Plain	PES 1	14 x 9	0.310 ± 0.008	10.70	92.4 ± 1.0
	PES 2	14 x 9	0.400 ± 0.007	11.77	126.3 ± 0.7
	PP1	14 x 9	0.420 ± 0.007	11.77	125.3 ± 0.7
Satin	PES 1	14 x 9	0.340 ± 0.017	10.70	88.7 ± 2.2
	PES 2	14 x 9	0.445 ± 0.009	11.77	122.5 ± 1.8
	PP1	14 x 9	0.435 ± 0.016	11.77	121.5 ± 2.7
Jacquard	PES 1	14 x 9	0.340 ± 0.017	10.70	87.6 ± 1.2
	PES 2	14 x 9	0.420 ± 0.020	11.77	124.5 ± 1.9
	PP1	14 x 9	0.450 ± 0.015	11.77	123.4 ± 1.1

Observing Table 15, thickness was, practically, the same for each type of narrow fabric. As per Equation 5, cover factor depends on threads/cm and linear mass and the fabric cover factor is obtained by Equation 6. As warp was the same for all narrow fabrics and the ends x picks was also equal, cover factor was the same for each type of narrow fabric. For example, cover factor for plain with PES 1 in weft was the same for plain, satin and jacquard. The larger the cover factor, more closed is the structure. Regarding weight per area, and as expected, narrow fabrics with PES 2 and PP 1 in the weft presented a similar weight due equal linear densities and narrow fabrics with PES 1 in the weft presented lower weight due its linear mass inferior comparatively to PES 2 and PP 1 [209].

In the development of brain phantom, more opened structures probably will be more adequate to simplify the inner and outer water flow (restricted and hindered diffusion, respectively) since if structure is extremely closed, it will be more difficult to water penetrate through the yarns.

3.2.2. Tensile properties

Table 16 presents the values of breaking strength and extension at failure of the narrow fabrics.

Table 16: Tensile results of the different narrow fabrics

Weave pattern	Yarns in the weft	Breaking force (N)	Extension at failure (%)
Plain	PES 1	667.0 ± 8.4	36.1 ± 0.7
	PES 2	684.0 ± 2.0	38.2 ± 0.7
	PP1	675.0 ± 0.7	40.9 ± 0.9
Satin	PES 1	665.2 ± 0.7	35.9 ± 1.9
	PES 2	664.0 ± 7.3	36.4 ± 1.8
	PP1	676.0 ± 1.7	39.2 ± 0.4
Jacquard	PES 1	667.0 ± 7.1	33.9 ± 1.6
	PES 2	676.0 ± 5.4	35.8 ± 1.2
	PP1	673.5 ± 2.2	44.1 ± 1.1

Representative force – extension curves of the different weave patterns are presented in Figure 70.

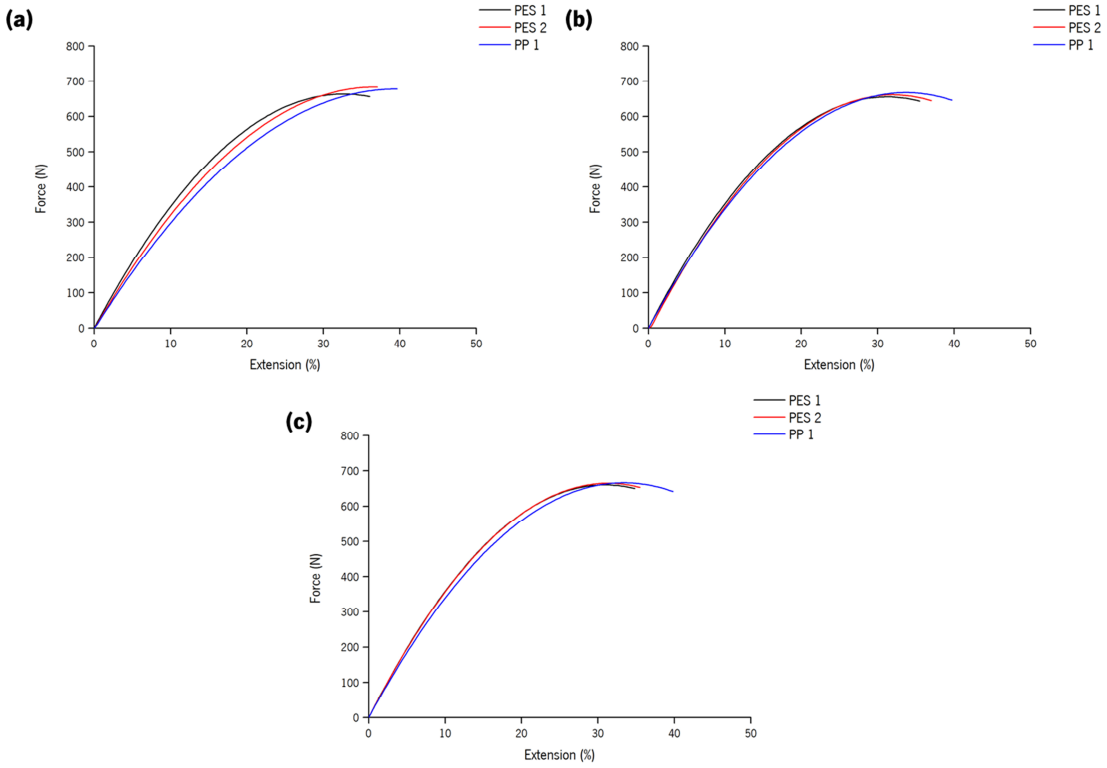


Figure 70: Load – extension curves of: (a) plain; (b) satin; (c) jacquard.

According to literature, the type of weave has a greater influence on the breaking force of fabrics in warp direction than different types of yarns [216]. Analyzing Figure 70 and Table 16, there were no significant differences in the breaking force and extension at failure values between the different patterns. Moreover, narrow fabrics presented response almost linear elastic to fracture.

Elastic deformation region occurred until, approximately, 25% of the extension for all narrow fabrics produced in this study (Figure 70). In the plastic deformation region, which occurred after of these 25% of the extension, the deformations tend to be localized, creating non-uniformity in the yarns, as explained before. Similarly to what was said for the braided structures, it should be taken into account that specifically for the application on brain phantoms, narrow fabrics will not be subjected to such high forces that lead to the rupture.

It is possible to confirm from the results provided in Figure 71 that, in general, and as expected, plain presented higher values due to the maximum number of interlacing points resulting in higher tensile strength in warp direction [216].

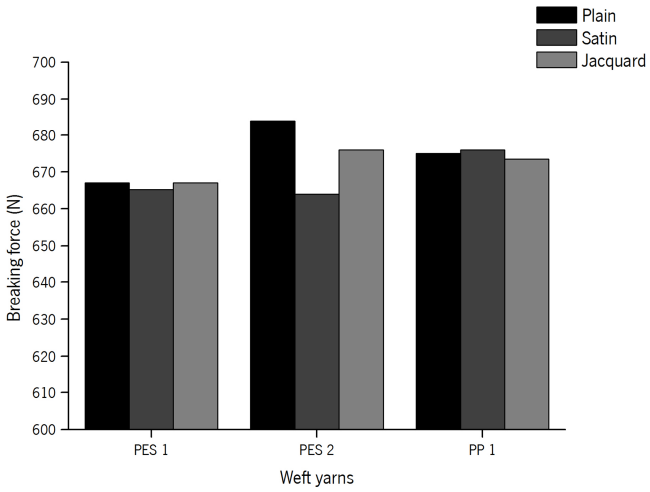


Figure 71: Breaking force of narrow fabrics.

3.2.3. Vertical wicking

Wicking curves for narrow fabrics, according with weave patterns are presented in Figure 72.

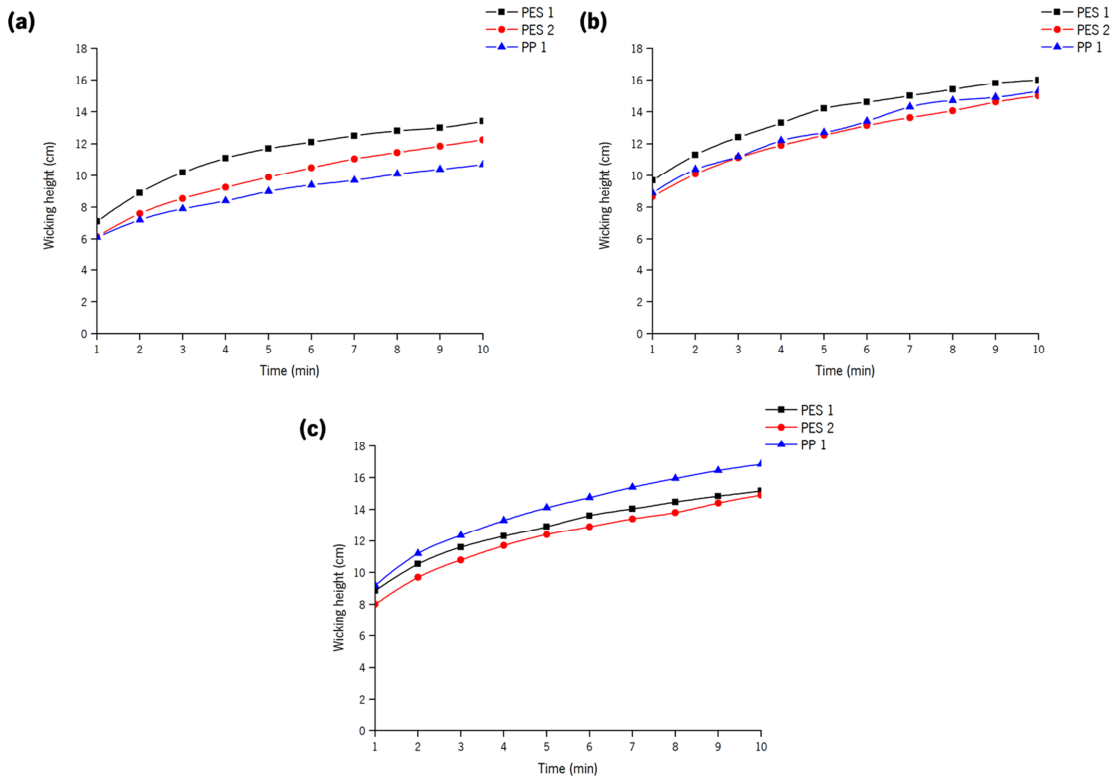


Figure 72: Wicking height of: (a) plain; (b) satin; (c) jacquard.

It is possible to see that plain reached a lower height when compared to satin and jacquard since it has a more closed structure. Additionally, there were no significant differences inside each type of narrow fabric, due the fact that vertical wicking is done in warp direction and warp is equal for all narrow fabrics.

As the curves presented almost linear behavior when compared, for example, to the curves of yarns presented in Chapter III, the linear fit for each braided structure during the 10 minutes of the wicking test was calculated. Table 17 shows the regression values and the correlation coefficient of linear fit. The correlation was found to be good.

Table 17: Regression values and correlation coefficient of the narrow fabrics

Weave pattern	Yarns in the weft	Slope (cm/min)	Intercept (cm)	Coefficient of correlation
Plain	PES 1	0.624	7.85	0.868
	PES 2	0.637	6.35	0.952
	PP1	0.479	6.25	0.952
Satin	PES 1	0.659	10.15	0.910
	PES 2	0.660	8.84	0.955
	PP1	0.688	9.01	0.954
Jacquard	PES 1	0.649	9.26	0.931
	PES 2	0.701	8.35	0.940
	PP1	0.791	9.60	0.940

Based on these results, satin and jacquard fabrics presented higher values of slope and intercept comparatively with plain. As higher the slope and intercept, better the wickability [134], satin and jacquard presented a better wickability since that they have more space between warp and weft yarns when compared to the plain structure. The influence of weave pattern in vertical wicking is demonstrated in literature [217,218].

3.3. Embroidered structures

Figure 73 shows the desired layout that was embroidered and the embroidered textile coatings.

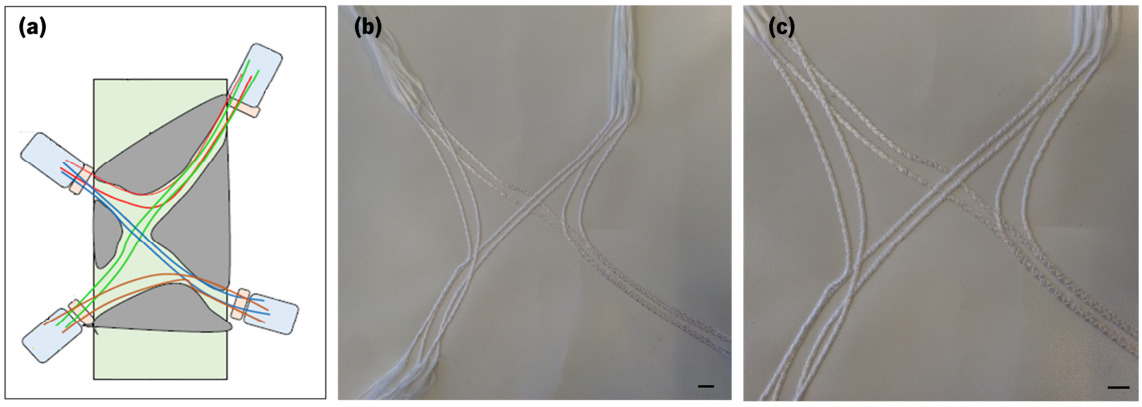


Figure 73: (a) Top view of optic chiasm layout; (b) embroidered textile coating mimicking the optic chiasm; (c) magnification of embroidered optic chiasm. Scale bars represent 1 cm.

10 PP hollow multifilament yarns were used in each colored line of the layout. A design file according to the layout of optic chiasm was created and the fabric was stabilized and placed in the machine. The PP multifilament yarns were placed in one of the machine heads that move along x and y-directions, in accordance to the programmed pattern, creating the desired embroidered structure. PP hollow multifilament yarns were then deposited on the substrate and hold by the stitches. All embroidery process was automatic. Both thicker (570 ± 50 gr/m^2) as thinner (300 ± 30 gr/m^2) substrates worked on the embroidery machine. Substrates with high thicknesses can cause false stitches, leading to production fails. The substrates are hydrophobic in order to make no influence on the water flow through the yarns. Hydrophilic substrates promote non-oriented water flow, which will be negative in the case of anisotropic brain phantom application.

Although it has only been applied in pilot production context, it is possible to see that embroidery showed to be a suitable technique able to mimic some crossing patterns of the human brain, since this procedure is computer-controlled, allowing to create complex pattern. Moreover, it is an accurate and reproducible process.

4. Conclusions

This chapter presented the development and characterization of fibrous structures based on PP hollow multifilament yarns. As in the previous chapter, this is a new study since in literature there are no studies concerning the use of textile technologies to help in the development of brain phantoms. Other research works about development of anisotropic brain phantoms, rather report the use of fibrous materials arranged according to the required architecture by intensive handwork.

Braiding, narrow weaving and embroidery technologies showed to be appropriate to mimic human axon configurations. The application of these technologies allowed positioning PP hollow multifilament yarns in unidirectional, bidirectional and multidirectional orientations, mimicking the configurations of white matter human axons. Similarly, fibrous structures allowed holding several yarns, simulating the large number of axons that exists in brain white matter. Furthermore, by application of textile technologies the production time and reproducibility of the phantom could be improved.

The development of fibrous structures using textile technologies as well as the characterization of the produced fibrous structures is a novel approach to be taken in consideration in the brain phantom development area. The results presented in this chapter, although not yet applied, can be useful for the development of a brain phantom in the future.

CHAPTER V: Development and validation of the brain phantom

1. Introduction

As referred in Chapter I, a gold standard for the validation and subsequent quality control of neuroimaging techniques based on water motion in human brain is crucial for clinical purposes. For instance, it is of major importance to know in what extent the images obtained by the same equipment at different time points or taken by multiple different MRI machines are comparable.

In last years, several brain phantoms have been developed, with a range of materials, where synthetic fibrous materials applied in anisotropic phantoms have shown better results when compared to other materials. Ideally, an anisotropic diffusion phantom should yield similar FA and also MD values to those found in brain. However, to date physical phantoms based on synthetic fibrous materials have shown discrepancies between the microscopic geometry and configuration and the characteristics of real tissue [15] and thus this type of phantoms have been barely used.

In an attempt to circumvent the current limitations, and according the results obtained along this research work, it was possible to develop a novel brain tissue mimetic device that aims the achievement of a universal and accurate brain phantom. The purpose of the study described in this chapter is to evaluate the PP hollow multifilament yarns in order to mimic the human axons of brain white matter and, also, to validate both existing and new MRI methodologies via providing calibration objects for MRI scanners, in particular to prove the accuracy of the novel HDFT neuroimaging technique with the first phantom developed to validate this technique [219].

PP hollow multifilament yarns (specifically PP 1) were used as axon-mimicking structures for brain white matter in the development/validation of an anisotropic brain phantom. An important parameter of materials used to mimic human axons is to accurately simulate hindered and restricted water diffusion (Figure 4). Having this purpose in mind, fluorescence microscopy was used to prove that PP hollow multifilament yarns exhibit these two types of diffusion.

The development and assessment of the anisotropic brain phantom was done at the Learning Research Development Center, from the University of Pittsburgh, and Psychology Software Tools Inc.

2. Material and methods

2.1. Water diffusion in hollow multifilament yarns

To check the inner flow, i.e. water flows through the yarn through hollow passage, PP hollow yarns were embedded into an epoxy resin to ensure that the interfilament spaces would be filled, allowing that water to flow only by the hollow spaces. An apparatus was created to allow the filaments filling with a fluorescent dye (Rhodamine B R6626, supplied by Sigma-Aldrich®, previously dissolved in water) under vacuum, using a Eurovacuum pump under -1bar, during 15 minutes (Figure 74). The fluorescent dye allows visualize the existence of inner flow by fluorescence microscopy.

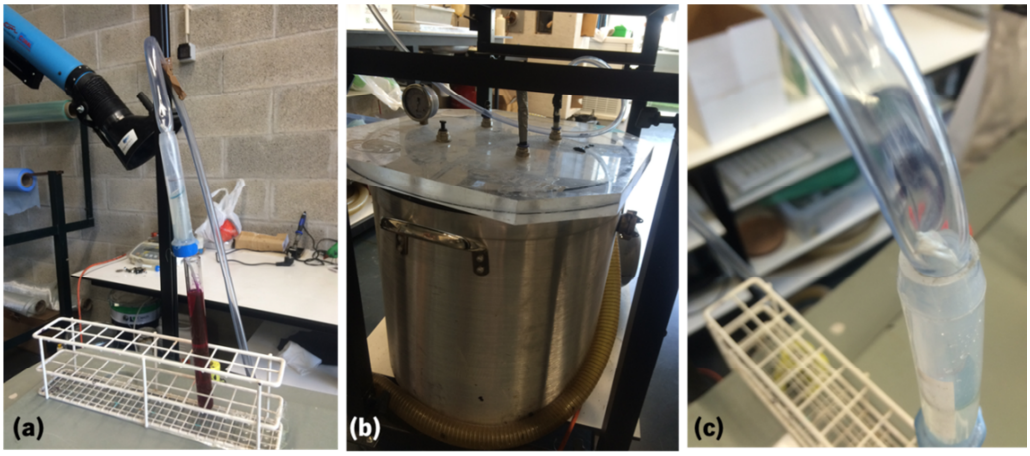


Figure 74: Filling process apparatus: (a) filling hollow yarns with fluorescent dye (Rhodamine B R6626); (b) vacuum pump; (c) detail of PP hollow multifilament yarns.

Transversal cuts of the PP hollow yarns were prepared using a microtome (Microtome Leitz). Filaments cross-sections were analyzed using an epifluorescence microscope (Olympus BX51) coupled with a DP71 digital camera and three sets of filters (DAPI – λ_{exc} 365-370/420; FITC – λ_{exc} 470-490/520; and TRITC – λ_{exc} 530-550/590). All images were acquired using the Olympus cellSens software.

Additionally, to observe the outer flow, i.e., water diffusion in the interfilament spaces, the yarns were placed vertically in contact with the same fluorescent dye to allow its capillary rise, using the experimental setup to measure vertical wicking, as shown in Figure 35. Filaments cross-sections were then made, which were further visualized under fluorescence microscope, the same way as explained above.

2.2. Phantom development

PP hollow multifilament yarns (specifically PP 1) were used to create the textile brain phantom. Briefly, the modular phantom for calibrated anisotropic imaging was developed by 3D printing and the materials used were selected according to properties such as: non-reactivity to MRI, stability in water, and ease of handling.

The phantom was formed by different layers that can be fixed according the desired configuration, so providing a modular aspect to the phantom. An outer shell comprised by a foam was created for insulation purposes and an inner shell to mimic the brain fat layer was included using a space filled with oil. The hollow filaments were placed in frames in fascicle and combined into tracks that were supported in fixed frames within the phantom. The temperature is controlled by a heating layer and the frusto-spherical shape allows for easy mounting within an MRI (Figure 75 (a)).

To correctly resolve the complex geometrical patterns of white matter pathways in the human brain, the yarns were placed in frames with different crossing patterns, namely with 30°, 45°, and 90° by assembling ribbons of yarns with dimensions of 2.5 mm by 10 mm (Figure 75 (c)). In order to simulate different densities of axons, an area with five equal volume chambers was created with yarns density of 20 %, 40 %, 60 %, 80 % and 100 %, with unidirectional orientation to 0° (Figure 75 (b)).

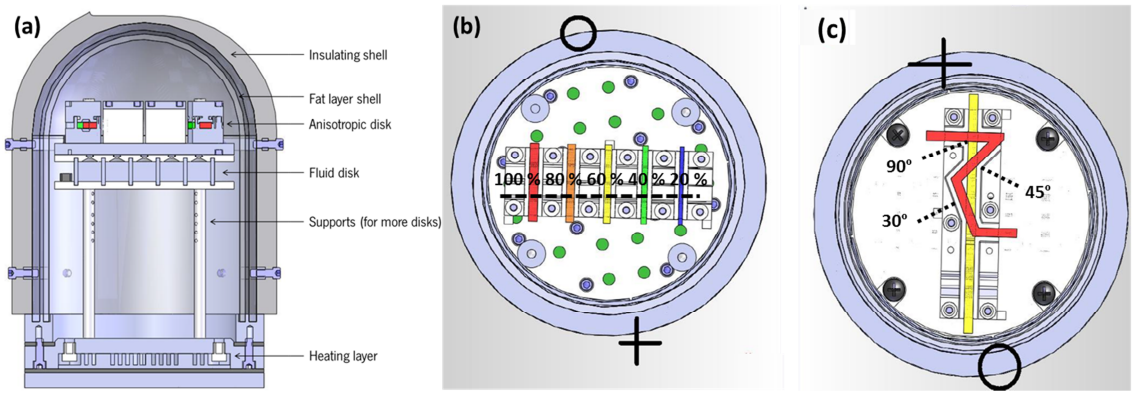


Figure 75: Schematic representation of the developed brain phantom (a) constituents of brain phantom; (b) frames with different yarn density areas where yarns are oriented to 0°; (c) frame with yarns assembled with different crossing angles (Images provided by Walt Schneider Lab).

The filling process of the hollow multifilament yarns, internally and externally, was performed with distilled water by pressure filling as shown in Figure 76, where is possible to see a frame with PP

hollow yarns (red circle). Moreover, phantom is filled with distilled water to simulate the water existing in the human brain.

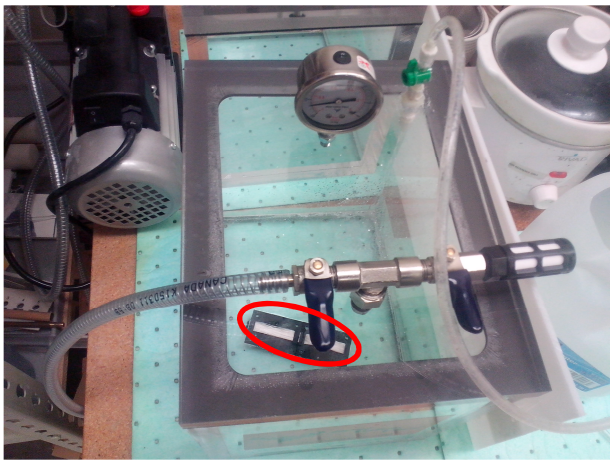


Figure 76: Filling process of the PP hollow multifilament yarns. Red circle highlighted the frame with yarns.

Figure 77 presents the brain phantom developed, as well as the scanning system of an MRI machine. Figure 77 (a) shows the two zones of the anisotropic brain phantom, identified by (1) the zone of the crossing yarns, where yarns are assembled with different crossing angles; and (2) the zone of the fiber density, where there are frames with different yarn density areas and yarns are oriented to 0°. For the scanning, by MRI machine, the brain phantom is placed inside a head coil as possible to see in Figure 77 (b).

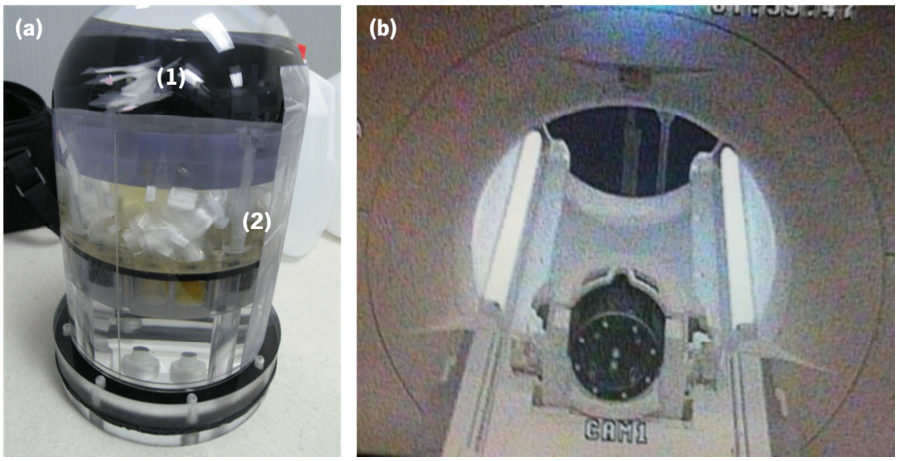


Figure 77: (a) Brain phantom with different areas – (1) crossing yarns and (2) fiber density; and (b) brain phantom inside of a head coil prepared to be scanned in a MRI equipment (Images provided by Walt Schneider Lab).

2.3. HDFT phantom validation

Scanning was done on 3T MRI scanners: 3T Trio MR Siemens system and 3T Connectome scanner with simultaneous multi-slice diffusion acquisition. The MR signal comes from the water that diffuses within the filaments. Fiber tracking, as well as FA and MD values, are performed using principle diffusion directions, which were calculated using reconstruction method proposed by Pathak [220].

3. Results and discussion

3.1. Water diffusion in hollow multifilament yarns

Figure 78 presents the cross-sections visualized under fluorescence microscopy after filling process to prove that PP hollow multifilament yarns allow hindered (outer flow) and restricted (inner flow) diffusion.

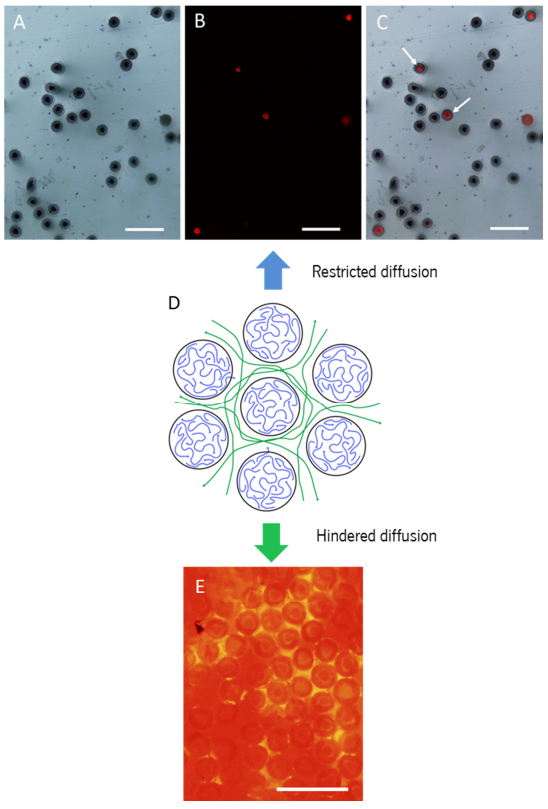


Figure 78: Fluorescence images of PP yarns cross-sections (A, B, C, E). D) represents the model of water motion in the human axons already presented in Chapter I. In C) arrows indicate water marked with fluorescent dye inside filaments (restricted diffusion) that can be easily tracked on the overlap channel. In E) it is possible to observe fluorescent dye between filaments, representing hindered diffusion. Scale bar represents 100 µm.

The restricted diffusion behavior was confirmed via the observation of a fluorescence spot in the internal area of the yarns (Figure 78 A, B and C), proving that water passes inside hollow part of filaments. Only around 15 % of the filaments were filled with water probably due to the short test time (15 minutes). Nevertheless, this is a sufficient exposure time to prove the concept of the restricted water movement, according to Zuccolotto *et al.* [219]. The hindered diffusion behavior was observed by the presence of fluorescent marker in the surrounding environment of the yarns obtained by capillarity (Figure 78 E).

These findings about restricted and hindered diffusions visually corroborate the theoretical literature findings about wicking in hollow multifilament yarns, proving that there is an inner and outer water flow through the hollow and interfilament spaces, respectively [153].

Based on the above, the PP hollow multifilament yarns promoted both restricted and hindered movement of water, which makes them suitable for phantom development.

3.2. HDFT phantom validation

PP hollow multifilament yarns were further used to validate HDFT imaging. Figure 79 presents the results of the fiber tracking.

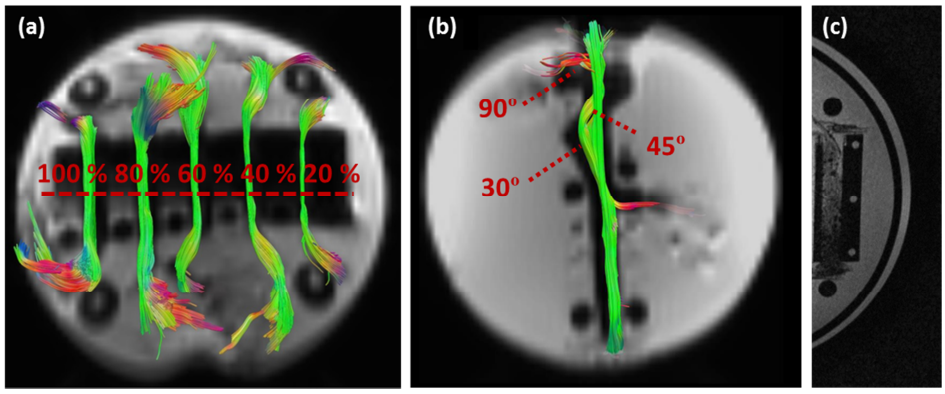


Figure 79: Fiber tracking: yarn density areas (a); yarn crossing areas (b); and, yarns without water inside of the hollow part (c). Colors on the map according to their orientation: red, lateral-medial (x – axis); green, anterior-posterior (y - axis); blue, inferior-superior (z - axis). Other colors indicate mixed orientation of the yarns (Images provided by Walt Schneider Lab).

The effect of different yarn density areas (Figure 79 (a)), different yarn crossing areas (Figure 79 (b)) and, also, the yarns without water inside (Figure 79 (c)) can be observed.

Figure 79 (a) and Figure 79 (b) show that HDFT can successfully locate the filament bundles. It is worth noting that the fiber tracts are clearly visible: the reduction of PP yarns in Figure 79 (a)

(from left to right), extremely important for investigation of some diseases, e.g. Alzheimer's, characterized with the loss of axons, was accurately solved as observed by the green colored fiber bundles. Moreover, the crossing zones are also clearly visible in Figure 79 (b). The red fiber bundle showed a 90° crossing angle and yellow refered to a 45° crossing angle. 30° crossing angle was not clearly visible in comparison with those of 45° and 90°, presenting a green fiber bundle. There was no difference in color of the bundle with the change of direction due to the angle. Possibly, this is a limitation caused by the model or a limitation of the current diffusion imaging acquisition technology. Nevertheless, the HDFT do not create artifacts on these crossing areas of the human axons of the white matter, allowing for better representation of this brain area. Regarding yarns that did not have water inside (Figure 79 (c)), it would be expected some signal related with water that exists between filaments (hindered diffusion). Again, this could be due to a limitation of the current diffusion imaging acquisition. However, this result proves, once more, that there is water motion inside of the hollow filaments that were exposed to pressure filling as shown in Figure 79 (a) and Figure 79 (b).

These images support the conclusion that PP hollow multifilament yarns are appropriate to mimic the white matter axons and, once again, prove that there is an appropriate water movement inside of the hollow filaments.

Besides the visualization of the fiber bundles, the evaluation of the FA and MD parameters, related with water movement, is extremely important to validate an anisotropic brain phantom. Table 18 summarizes the FA and MD values, measured in accordance with the mathematical algorithms described by Pathak [220].

Table 18: Fractional anisotropy and mean diffusivity values for different five density zones and for fiber crossing

		Fractional anisotropy (FA)	**Mean diffusivity ($x10^{-3}$) (MD)**
Density zones	**20 %**	0.81 ± 0.22	0.15 ± 0.09
	40 %	0.80 ± 0.21	0.19 ± 0.12
	60 %	0.77 ± 0.18	0.22 ± 0.09
	80 %	0.78 ± 0.23	0.16 ± 0.08
	100 %	0.85 ± 0.20	0.19 ± 0.09
Crossing zones		0.73 ± 0.24	0.23 ± 0.10

FA and MD values found in the PP hollow multifilament yarns assembled at different density areas and with different crossing zones are comparable to those values observed in white matter of the human brain. Indeed, fractional anisotropy values shown were very similar to the value observed in the corpus callosum in the human brain (0.7) [221]. Comparing the results with the average MD and FA values observed by Richardson *et al.* [222] in the ex vivo optic nerve of a rat (MD = 0.148 x 10-3 mm2s-1; FA = 0.86) it should be noted that the brain phantom presented in this work obtained analogous values to those found in literature.

4. Conclusions

In this chapter, the development and validation of brain phantom based in PP hollow multifilament yarns studied before was presented.

It was proved, by fluorescence microscopy that PP hollow yarns allow the two type of diffusion that occurs in the human axons: hindered and restricted diffusion, visually showing the theoretical findings found in literature about capillarity in hollow multifilament yarns.

Fiber tracking results showed that FA as well as MD values were similar to the healthy human brain. Furthermore, HDFT seems to be an excellent option in the diffusion magnetic resonance modalities since it showed clearly visible fiber tracts, crossing zones, and is capable of differentiating different densities of material.

In conclusion, the PP hollow multifilament yarns studied in this work allowed for the generation of structures with suitable properties for the development of anisotropic phantoms with the following properties: i) hollow configuration that simulate the human axons shape, ii) diameters comparable to axon fibers found in brain white matter, iii) hydrophobic nature to mimic proper environment of the brain anisotropy and iv) capacity to promote diffusion of water in its structure with a restricted and hindered motion. Altogether, these properties established the PP hollow multifilament yarns as appropriate for the generation of axon-mimicking phantoms, allowing development a ground truth standard that can be used to validate current and new algorithms for fiber tracking.

CHAPTER VI: Conclusions and work perspectives

1. Final conclusions

The main objective of this research work was to develop fibrous structures adequate to develop anisotropic brain phantoms in order to validate and evaluate neuroimaging techniques, specifically the novel MRI imaging tool: High-Definition Fiber Tractography, developed by Learning Research Development Center of the University of Pittsburgh (USA). In this final chapter, the main contributions of this work are summarized and some aspects for future work are also highlighted.

The first chapter presented an overview of the brain neuroimaging techniques, emphasizing the neuroimaging techniques based on the diffusion of water molecules in the brain since HDFT is based on water motion through brain tissue. The validation and quality control of these techniques was referred as a key issue to be used in brain phantoms development, showing that anisotropic brain phantoms based on synthetic fibrous materials are promising candidates for the validation of diffusion neuroimaging techniques. Introduction showed the importance of developing an anisotropic brain phantom that mimics the human axons and the complex regions of brain such as the crossing areas, since a true calibration of diffusion measurement in the MRI is necessary. It is mandatory to be sure that what is observed by these diffusion neuroimaging techniques corresponds to reality. Moreover, it is crucial to know to what extent the images obtained by the same equipment at different time points or taken by multiple different MRI machines are comparable. Size, geometry and configurations are some current limitations of the anisotropic brain phantoms described in the literature.

Chapter II showed a briefly review about synthetic fibrous materials that can be used in the development of brain phantoms taking into account some characteristics such as the diameter of the yarns; the tubular geometry; to have an hydrophobic behavior to permit simulating the anisotropic values of the white matter that is around 0.7. In order to attend these requirements, hollow multifilament yarns were chosen to mimic human axons and three approaches in order to obtain the desired dimensions were evaluated: PP and PA hollow multifilament commercial yarns obtained by melt spinning technique; post-production stretching of the previously mentioned hollow yarns, using a laboratorial filament extrusion line; and, production of coaxial electrospinning polycaprolactone fibers using the electrospinning technique. Filament cross-section analysis was done using SEM. It was concluded that the three approaches allowed obtaining the desired dimensions of human axons, between 1 – 25 μm. However, electrospun

fibrous structures were found to be more difficult to engineer and consequently hard to be the basis for brain phantom development. Therefore, PP and PA hollow multifilament yarns continued in the study.

In Chapter III a physical, chemical and mechanical characterization of PP and PA hollow multifilament yarns was presented, important to help understanding the scanning results of the brain phantoms which, sometimes, cannot be fully explained. Both hollow multifilament yarns showed to be appropriate for the development of anisotropic brain phantom. However, PP hollow multifilament yarns presented some advantages when compared to PA hollow multifilament yarns: 1) a range of diameters obtained by PP after post-production stretching that mimics the different human axons dimensions; 2) less susceptibility to wettability, proved by the contact angle, showing a hydrophobic behavior, which is desired in the development of anisotropic brain phantoms; 3) higher wickability, useful to mimic the types of diffusion processes in brain white matter. Therefore, it was decided to move forward with PP hollow multifilament yarns, more specifically PP 1 since a MRI scan is an expensive analysis and PP 1 showed the higher capillary rise when compared to the other PP hollow multifilament yarns.

In order to create structures that replicate the large number of human axons as well as decrease the production time of the brain phantom, assuring high levels of reproducibility, Chapter IV presented the development of possible fibrous structures, using braiding, weaving and embroidery technologies. The results obtained in the characterization of these structures were also provided. It was concluded that braided and embroidered structures and narrow fabrics showed to be appropriate to mimic the human axons orientation in the brain white matter.

The development of the anisotropic brain phantom with density and crossing yarns zones as well as its scanning to study the behavior of PP hollow multifilament yarns in mimicking the human axons was presented in Chapter V. It was also shown, by fluorescence microscopy, that PP hollow yarns allowed an inner and outer water flow, mimicking the hindered and restricted diffusion that occurs in human axons. Scanning and posterior analysis of data with HDFT showed that PP hollow multifilament yarns are indeed able to mimic the human axons, promoting high fractional anisotropy values similar to the ones of healthy white matter. Moreover, HDFT showed detailed images of the yarns, both in the different density zones and crossing zones.

Despite the difficulties encountered during the progress of this work mainly due to its novelty and scarce related literature, this study efficiently contributed for the development of the first phantom used to validate the new neuroimaging technique, HDFT. PP hollow multifilament yarns were found to possess outstanding properties able to mimic the human brain axons. The development of this anisotropic brain phantom allowed for the validation of the HDFT that when applied to the human brain may help on the detection of several brain damages such as traumatic brain injuries, gliomas or Alzheimer disease, advancing on the detection efficacy when compared to current neuroimaging techniques that sometimes fail due to resolution issues.

2. Work perspectives

With this study, it was showed that hollow multifilament fibrous materials are an excellent option to mimic the human axons in the development of anisotropic brain phantoms.

With the aim to complete the study about the fibrous materials presented in this work, the development of brain phantoms with all PP hollow multifilament yarns studied should be carried out in order to investigate the influence of diameter in HDFT results. Furthermore, it would also be interesting to compare HDFT results of PP and PA hollow multifilament yarns, studying the influence of different synthetic materials. Similarly, electrospun hollow fibers should also be studied in more detail in the future, allowing the study of the influence of diameters and different synthetic materials and further validate its applicability to the human brain phantoms.

Other interesting topic to be developed in a future work would be the creation of an anisotropic brain phantom with the fibrous structures proposed in this work: braided structures, narrow and embroidery fabrics. This is expected to reduce the manufacture time and, consequently, the development costs. Moreover, since they are based in semi-automated processes the reproducibility of the manufactured brain phantoms would be higher. Still, related with fibrous structures, an interesting future study would be using fibrous materials based on water-soluble polymers to apply, for example, in the outside part of the braided structures, replacing the PA monofilaments. These soluble fibrous materials in water could maintain the integrity of the structure just before getting in contact with water, being subsequently dissolved. Consequently, only the hollow multifilaments would be scanned by the imaging technique.

References

[1] S. Koskinen, H. Alaranta, Traumatic brain injury in Finland 1991–2005: A nationwide register study of hospitalized and fatal TBI, Brain Inj. 22 (2008) 205–214.

[2] B. Roozenbeek, A.I.R. Maas, D.K. Menon, Changing patterns in the epidemiology of traumatic brain injury, Nat. Rev. Neurol. 9 (2013) 231–236.

[3] J. Fernandez-Miranda, S. Pathak, W. Schneider, High-Definition Fiber Tractography: Unraveling the connections of the human brain, Neurosurg. News - Univ. Pittsburgh. 13 (2012).

[4] H.G. Belanger, R.D. Vanderploeg, G. Curtiss, D.L. Warden, Recent Neuroimaging Techniques in Mild Traumatic Brain Injury, J. Neuropsychiatry Clin. Neurosci. 19 (2007) 5–20.

[5] J.M. Provenzale, Imaging of traumatic brain injury: a review of the recent medical literature, Am. J. Roentgenol. 194 (2010) 16–9.

[6] S.S. Shin, T. Verstynen, S. Pathak, K. Jarbo, A.J. Hricik, M. Maserati, et al., High-definition fiber tracking for assessment of neurological deficit in a case of traumatic brain injury: finding, visualizing, and interpreting small sites of damage, J. Neurosurg. 116 (2012) 1062–9.

[7] J.C. Fernandez-Miranda, S. Pathak, J. Engh, K. Jarbo, T. Verstynen, F.-C. Yeh, et al., High-definition fiber tractography of the human brain: neuroanatomical validation and neurosurgical applications, Neurosurgery. 71 (2012) 430–53.

[8] C. Nimsky, M. Bauer, B. Carl, Merits and Limits of Tractography Techniques for the Uninitiated, in: Johannes Schramm (Ed.), Adv. Tech. Stand. Neurosurgery, Vol. 43, Springer, 2016.

[9] N. Presson, D. Krishnaswamy, L. Wagener, W. Bird, K. Jarbo, S. Pathak, et al., Quantifying White Matter Structural Integrity With High-Definition Fiber Tracking in Traumatic Brain Injury, Mil. Med. 180 (2015) 109–121.

[10] K. Abhinav, F.-C. Yeh, A. Mansouri, G. Zadeh, J.C. Fernandez-Miranda, High-definition fiber tractography for the evaluation of perilesional white matter tracts in high-grade

glioma surgery, Neuro. Oncol. 17 (2015) 1199–209.

[11] D.T. Fernandes-Cabral, G.A. Zenonos, R.L. Hamilton, S.S. Panesar, J.C. Fernandez-Miranda, High-Definition Fiber Tractography in the Evaluation and Surgical Planning of Lhermitte-Duclos Disease: A Case Report, World Neurosurg. (2016).

[12] S.S. Shin, S. Pathak, N. Presson, W. Bird, L. Wagener, W. Schneider, et al., Detection of white matter injury in concussion using high-definition fiber tractography, Prog. Neurol. Surg. 28 (2014) 86–93.

[13] J.C. Fernandez-Miranda, J. a Engh, S.K. Pathak, R. Madhok, F.E. Boada, W. Schneider, et al., High-definition fiber tracking guidance for intraparenchymal endoscopic port surgery, J. Neurosurg. 113 (2010) 990–9.

[14] M.V.R. Gonçalves, Processamento de Dados em Aquisição Simultânea de EEG/IFRM, Dissertação de mestrado, Universidade Nova de Lisboa, 2009.

[15] E. Fieremans, Validation Methods for Diffusion Weighted Magnetic Resonance Imaging in Brain White Matter, PhD Thesis, University Gent, 2009.

[16] L. Freberg, Discovering Biological Psychology, 2nd Ed., Wadsworth, 2010.

[17] L. Haider, T. Zrzavy, S. Hametner, R. Hö, F. Bagnato, G.N. Grabner, et al., The topograpy of demyelination and neurodegeneration in the multiple sclerosis brain, Brain. 139 (2016) 807–815.

[18] D.-M. Koh, D.J. Collins, Diffusion-weighted MRI in the body: applications and challenges in oncology, Am. J. Roentgenol. 188 (2007) 1622–35.

[19] Y. Assaf, Y. Cohen, Inferring microstructural information of white matter form diffusion MRI, in: H. Johansen-Berg, T.E.J. Behrens (Eds.), Diffus. MRI From Quant. Meas. to Vivo Neuroanat., 2nd Ed., Academic Press, 2014: pp. 185–208.

[20] S. Bano, M. Afzal, M.M. Waraich, Physical Principles, Use of High b-Values And Clinical Applications of Diffusion-Weighted Imaging of Ischemic Stroke, Int. J. Sci. Eng. Res. 4 (2013) 260–276.

[21] T.L. Chenevert, Principles of Diffusion-Weighted Imaging (DW-MRI) as Applied to Body

Imaging, in: D.-M. Koh, H.C. Thoeny (Eds.), Diffus. MR Imaging Appl. Body, Springer Science & Business Media, 2010: pp. 3–17.

[22] B. Jeurissen, Improved analysis of brain connectivity using high angular resolution diffusion MRI., PhD Thesis, University of Antwerpen, 2012.

[23] L.J. O'Donnell, C.-F. Westin, An introduction to diffusion tensor image analysis, Neurosurg. Clin. N. Am. 22 (2011) 185–96.

[24] H.M. Feldman, J.D. Yeatman, E.S. Lee, L.H.F. Barde, S. Gaman-Bean, Diffusion tensor imaging: a review for pediatric researchers and clinicians, J. Dev. Behav. Pediatr. 31 (2010) 346–56.

[25] M.E. Thomason, P.M. Thompson, Diffusion imaging, white matter, and psychopathology, Annu. Rev. Clin. Psychol. 7 (2011) 63–85.

[26] A. Petraglia, J. Bailes, D. Arthur, Handbook of neurological sports medicine concussion and other nervous system injuries in the athlete, Medknow Publications, 2015.

[27] E. Fieremans, Y. De Deene, S. Delputte, M.S. Ozdemir, E. Achten, I. Lemahieu, The design of anisotropic diffusion phantoms for the validation of diffusion weighted magnetic resonance imaging, Phys. Med. Biol. 53 (2008) 5405–5419.

[28] P. Kochunov, P.M. Thompson, J.L. Lancaster, G. Bartzokis, S. Smith, T. Coyle, et al., Relationship between white matter fractional anisotropy and other indices of cerebral health in normal aging: Tract-based spatial statistics study of aging, Neuroimage. 35 (2007) 478–487.

[29] P.L. Hubbard, F.-L. Zhou, S.J. Eichhorn, G.J.M. Parker, Biomimetic phantom for the validation of diffusion magnetic resonance imaging, Magn. Reson. Med. 73 (2015) 299–305.

[30] N. Dowell, P. Tofts, Quality Assurance for Diffusion MRI, in: D.K. Jones (Ed.), Diffus. MRI Theory, Methods, Appl., Oxford University Press, USA, 2010.

[31] D.W. McRobbie, E.A. Moore, M.J. Graves, M.R. Prince, MRI from Picture to Proton, Cambridge University Press, 2006.

[32] M.O. Culjat, D. Goldenberg, P. Tewari, R.S. Singh, A review of tissue substitutes for ultrasound imaging, Ultrasound Med. Biol. 36 (2010) 861–873.

[33] P.L. Hubbard, G.J.M. Parker, Validation of Tractography, in: H. Johansen-Berg, T.E.J. Behrens (Eds.), Diffus. MRI From Quant. Meas. to in-Vivo Neuroanat., Academic Press, 2009: pp. 353–375.

[34] T.G. Close, J.D. Tournier, F. Calamante, L. a. Johnston, I. Mareels, A. Connelly, A software tool to generate simulated white matter structures for the assessment of fibre-tracking algorithms, Neuroimage. 47 (2009) 1288–1300.

[35] P. Pullens, C. Goebel, Anisotropic Phantom, Maastricht, The Netherlands, 2011.

[36] Y. Assaf, T. Blumenfeld-Katzir, Y. Yovel, P.J. Basser, Axcaliber: A method for measuring axon diameter distribution from diffusion MRI, Magn. Reson. Med. 59 (2008) 1347–1354.

[37] E. Fieremans, A. Pires, J.H. Jensen, A simple isotropic phantom for diffusional kurtosis imaging, Magn. Reson. Med. 68 (2012) 537–42.

[38] G. Steidle, F. Schick, Echoplanar diffusion tensor imaging of the lower leg musculature using eddy current nulled stimulated echo preparation, Magn. Reson. Med. 55 (2006) 541–8.

[39] K.M. Hasan, A.L. Alexander, P.A. Narayana, Does fractional anisotropy have better noise immunity characteristics than relative anisotropy in diffusion tensor MRI? An analytical approach, Magn. Reson. Med. 51 (2004) 413–7.

[40] M.E. Bastin, P.A. Armitage, On the use of water phantom images to calibrate and correct eddy current induced artefacts in MR diffusion tensor imaging, Magn. Reson. Imaging. 18 (2000) 681–7.

[41] Y. Zhou, G.B. Tefera, P.A. Narayana, Diffusion Imaging - Basic Principles, in: R.K. Gupta, S. Kumar (Eds.), Magn. Reson. Imaging Neurol. Dis. Trop., 1st Ed., JP Medical Ltd, 2014: pp. 58–79.

[42] T.L. Chenevert, C.J. Galbán, M.K. Ivancevic, S.E. Rohrer, F.J. Londy, T.C. Kwee, et al., Diffusion coefficient measurement using a temperature-controlled fluid for quality control

in multicenter studies, J. Magn. Reson. Imaging. 34 (2011) 983–987.

[43] P.S. Tofts, D. Lloyd, C. a Clark, G.J. Barker, G.J. Parker, P. McConville, et al., Test liquids for quantitative MRI measurements of self-diffusion coefficient in vivo, Magn. Reson. Med. 43 (2000) 368–374.

[44] C. Pierpaoli, J. Sarlls, U. Nevo, Polyvinylpyrrolidone (PVP) water solutions as isotropic phantoms for diffusion MRI studies, in: Proc. Intl. Soc. Mag. Reson Med., 2009: p. 1414.

[45] P. Pullens, P. Bladt, P.M. Parizel, A highly standardized, easy to produce and cost-effective isotropic PVP diffusion phantom for quality assessment and multicenter studies, in: Proc. Intl. Soc. Mag. Reson. Med., 2015: p. 2760.

[46] M.A. Boss, T.L. Chenevert, M.A. Rosen, E.F. Jackson, A.R. Guimaraes, T. Persigehl, et al., QIBA PDF MRI Technical Committee: Activities in Diffusion MRI, 2014. Poster. Quantitative Imaging Biomarkers Alliance.

[47] M. Neeman, J.P. Freyer, L.O. Sillerud, A Simple Method for Obtaining Cross-Term-Free Images for Diffusion Anisotropy Studies in NMR Microimaging, Magn. Ressonance Med. 21 (1991) 138–143.

[48] J.D. Trudeau, W.T. Dixon, J. Hawkins, The Effect of inhomogeneous sample susceptibility on measured diffusion anysotropy using MRI, J. Magn. Reson. 108 (1995) 22–30.

[49] S. Boujraf, R. Luypaert, H. Eisendrath, M. Osteaux, Echo planar magnetic resonance imaging of anisotropic diffusion in asparagus stems, Magn. Reson. Mater. Physics, Biol. Med. 13 (2001) 82–90.

[50] X. Tang, E.E. Sigmund, Y. Song, Simultaneous Measurement of Diffusion along Multiple Directions, J Am Chem Soc. 126 (2004) 16336–16337.

[51] E.E. Sigmund, Y. Song, Multiple echo diffusion tensor acquisition technique, Magn. Ressonance Imaging. 24 (2006) 7–18.

[52] A. Rydhög, Using q-space Diffusion MRI for Structural Studies of a Biological Phantom at a 3T Clinical Scanner., Master of Science Thesis, Lund University, 2007.

[53] J. Lätt, M. Nilsson, A. Rydhög, R. Wirestam, F. Ståhlberg, S. Brockstedt, Effects of

restricted diffusion in a biological phantom: a q-space diffusion MRI study of asparagus stems at a 3T clinical scanner, Mag Reson Mater Phy. 20 (2007) 213–22.

[54] K.-J. Jung, An Osage Orange As a Diffusion Imaging Phantom For The Evaluation Of Slice-Accelerated Diffusion Imaging Sequence, Proc. Intl. Soc. Mag. Reson Med. 23 (2015) 3038.

[55] V. Juneja, Novel Phantoms and Post- Processing for Diffusion Spectrum Imaging, PhD thesis, University of Texas, 2012.

[56] J.C. Ford, D.B. Hackney, D.C. Alsop, H. Jara, P.M. Joseph, C.M. Hand, et al., MRI characterization of diffusion coefficients in a rat spinal cord injury model, Magn. Reson. Med. 31 (1994) 488–94.

[57] S.C. Partridge, W.B. DeMartini, B.F. Kurland, P.R. Eby, S.W. White, C.D. Lehman, Quantitative diffusion-weighted imaging as an adjunct to conventional breast MRI for improved positive predictive value, Am. J. Roentgenol. 193 (2009) 1716–22.

[58] Y. Guo, Y.-Q. Cai, Z.-L. Cai, Y.-G. Gao, N.-Y. An, L. Ma, et al., Differentiation of clinically benign and malignant breast lesions using diffusion-weighted imaging, J. Magn. Reson. Imaging. 16 (2002) 172–8.

[59] E. Rubesova, A.-S. Grell, V. De Maertelaer, T. Metens, S.-L. Chao, M. Lemort, Quantitative diffusion imaging in breast cancer: a clinical prospective study, J. Magn. Reson. Imaging. 24 (2006) 319–24.

[60] V. Gulani, A.G. Webb, I.D. Duncan, P.C. Lauterbur, Apparent Diffusion Tensor Measurements in Myelin- Deficient Rat Spinal Cords, Magn. Ressonance Med. 45 (2001) 191–195.

[61] S. Madi, K.M. Hasan, P. a. Narayana, Diffusion tensor imaging of in vivo and excised rat spinal cord at 7 T with an icosahedral encoding scheme, Magn. Reson. Med. 53 (2005) 118–125.

[62] J.S.W. Campbell, K. Siddiqi, V. V. Rymar, A.F. Sadikot, G.B. Pike, Flow-based fiber tracking with diffusion tensor and q-ball data: Validation and comparison to principal diffusion direction techniques, Neuroimage. 27 (2005) 725–736.

[63] R.Z. Freidlin, E. Ozarslan, M.E. Komlosh, L.-C. Chang, C.G. Koay, D.K. Jones, et al., Parsimonious model selection for tissue segmentation and classification applications: a study using simulated and experimental DTI data, IEEE Trans. Med. Imaging. 26 (2007) 1576–84.

[64] T. Numano, K. Hyodo, N. Nitta, J. Hata, N. Iwasaki, Apparent Diffusion Coefficient Mapping Using a Multi-Shot Spiral MRI Sequence of the Rat Brain, Open J. Radiol. 4 (2014) 13–24.

[65] E.A.H. von dem Hagen, R.M. Henkelman, Orientational diffusion reflects fiber structure within a voxel, Magn. Reson. Med. 48 (2002) 454–9.

[66] C.-P. Lin, V.J. Wedeen, J.-H. Chen, C. Yao, W.-Y.I. Tseng, Validation of diffusion spectrum magnetic resonance imaging with manganese-enhanced rat optic tracts and ex vivo phantoms, Neuroimage. 19 (2003) 482–495.

[67] N. Yanasak, J. Allison, Use of capillaries in the construction of an MRI phantom for the assessment of diffusion tensor imaging: demonstration of performance, Magn. Reson. Imaging. 24 (2006) 1349–61.

[68] L.G. Raguin, D. Hernando, D. Karampinos, L. Ciobanu, B.P. Sutton, Z. Liang, Quantitative Analsys of Q-Space MRI Data, 3rd Eur. Med. Biol. Eng. Conf. 11 (2005) 3–8.

[69] K. Cho, C. Yeh, Y. Chao, J. Chen, C. Lin, Accuracy Assessment of q-ball Imaging with Phantom Models, in: Proc. Intl. Soc. Mag. Reson. Med., 2006: p. 2752.

[70] J.-D. Tournier, C.-H. Yeh, F. Calamante, K.-H. Cho, A. Connelly, C.-P. Lin, Resolving crossing fibres using constrained spherical deconvolution: Validation using diffusion-weighted imaging phantom data, Neuroimage. 42 (2008) 617–625.

[71] A. V Avram, M.E. Komlosh, A.S. Barnett, E. Hutchinson, D. Benjamini, P.J. Basser, A processing pipeline and anisotropic diffusion phantom to calibrate DTI experiments, in: Proc. Intl. Soc. Mag. Reson Med., 2015: p. 158.

[72] M.E. Komlosh, D. Benjamini, A.S. Barnett, F. Horkay, P.J. Basser, Calibrating high q-value diffusion MRI methods wit a novel anisotropic phantom, in: Proc. Intl. Soc. Mag. Reson Med., 2015: p. 2759.

[73] M. Perrin, C. Poupon, B. Rieul, P. Leroux, A. Constantinesco, J.-F. Mangin, et al., Validation of q-ball imaging with a diffusion fibre-crossing phantom on a clinical scanner, Philos. Trans. R. Soc. Lond. B. Biol. Sci. 360 (2005) 881–91.

[74] E. Fieremans, S. Delputte, K. Deblaere, Y. De Deene, B. Truyens, Y. D'Asseler, et al., A flexible hardware phantom for validation of diffusion imaging sequences, in: Proc. Intl. Soc. Mag. Reson. Med., 2005: p. 1301.

[75] R. Lorenz, B.W. Kreher, J. Hennig, M.E. Bellemann, K.A. II, Anisotropic Fiber Phantom for DTI validation on a clinical scanner, in: Proc. Intl. Soc. Mag. Reson. Med., 2006: p. 2738.

[76] R. Lorenz, M.E. Bellemann, J. Hennig, K.A. Il'Yasov, Anisotropic phantoms for quantitative diffusion tensor imaging and fiber-tracking validation, Appl. Magn. Reson. 33 (2008) 419–429.

[77] C. Reischauer, P. Staempli, T. Jaermann, S. Kollias, P. Boesiger, Development of a Temperature Controlled Anisotropic Diffusion Phantom, in: Proc. Intl. Soc. Mag. Reson Med., 2007: p. 3535.

[78] J. Lindemeyer, E. Farrher, F. Grinberg, A.-M. Oros-Peusquens, N.J. Shah, Reduction of Susceptibility-Induced Field Gradients in Anisotropic Diffusion Fibre Phantoms Using Susceptibility Matching, in: Proc. Intl. Soc. Mag. Reson Med., 2015: p. 157.

[79] F.B. Laun, B. Stieltjes, S. Huff, L.R. Schad, INVESTIGATIONS OF A DTI-PHANTOM WITH PROPERTIES SIMILAR TO IN VIVO NEURONAL TISSUE, in: Proc. Intl. Soc. Mag. Reson Med., 2007: p. 1526.

[80] P. Pullens, A. Roebroeck, R. Goebel, Ground truth hardware phantoms for validation of diffusion-weighted MRI applications, J. Magn. Reson. Imaging. 32 (2010) 482–488.

[81] C. Poupon, B. Rieul, I. Kezele, M. Perrin, F. Poupon, J.F. Mangin, New diffusion phantoms dedicated to the study and validation of high-angular-resolution diffusion imaging (HARDI) models, Magn. Reson. Med. 60 (2008) 1276–1283.

[82] E. Farrher, J. Kaffanke, A.A. Celik, T. Stöcker, F. Grinberg, N.J. Shah, Novel multisection design of anisotropic diffusion phantoms, Magn. Reson. Imaging. 30 (2012) 518–526.

[83] M. Bach, B. Stieltjes, K. Fritzsche, W. Semmler, F.B. Laun, A Diffusion Tensor Resolution

Phantom, in: Proc. Intl. Soc. Mag. Reson Med., 2011: p. 3975.

[84] P. Pullens, M. Bach, B. Stieltjes, D. Smeets, P.M. Parizel, Diffusion tensor imaging of thirty-five anisotropic DTI phantoms for CENTER-TBI, in: Proc. Intl. Soc. Mag. Reson Med., 2015: p. 2761.

[85] M. Cann, E. Farrher, J. Cole, D. Poot, F. Grinberg, N.J. Shah, Diffusivity in crossing and diverging fibers: a multi-site phantom experiment, in: Proc. Intl. Soc. Mag. Reson Med., 2015: p. 152.

[86] P.L. Hubbard, F. Zhou, S.J. Eichhorn, T.B. Dyrby, G.J. Parker, A biomimetic phantom of white matter for application in diffusion MRI, in: Proc. Intl. Soc. Mag. Reson Med., 2012: p. 1939.

[87] F. Zhou, P.L. Hubbard, S.J. Eichhorn, Coaxially Electrospun Axon-Mimicking Fibers for Diffusion Magnetic Resonance Imaging, Appl. Mater. Interfaces. 4 (2012) 6311–6316.

[88] H. Lundell, T.B. Dyrby, P.L.H. Cristinacce, F.-L. Zhou, G.J.M. Parker, S.N. Jespersen, Validation of double diffusion schemes of microscopic fractional anisotropy, in: Proc. Intl. Soc. Mag. Reson. Med., 2015: p. 155.

[89] F. Elahi, W. Lu, G. Guoping, F. Khan, Core-shell Fibers for Biomedical Applications-A Review, Bioeng. Biomed. Sci. J. 3 (2013) 1–14.

[90] M. Denton, P. Daniels, Textile terms and definitions, 11th Ed., The Textile Institute, Manchester, 2002.

[91] K.K. Chawla, Fibrous Materials, 2nd Ed., Cambridge University Press, 2016.

[92] M. de J. da S. Carvalho, Tramas que o design tece : Têxteis do novo milénio - Têxteis técnicos e inteligentes., Dissertação de mestrado, Faculdade de Engenharia da Universidade do Porto, 2004.

[93] T. Hongu, G.O. Phillips, M. Takigami, New millenmium fibres, Woodhead Publishing Ltd, 2005.

[94] J. McIntyre, Historical background, in: J E McIntyre (Ed.), Synth. Fibres Nylon, Polyester, Acrylic, Polyolefin, Woodhead Publishing Ltd, 2005: pp. 1–19.

[95] R. Chattopadhyay, Introduction: types of technical textile yarn, in: R. Alagirusamy, A. Das (Eds.), Tech. Text. Yarns, Woodhead Publishing, 2010: pp. 3–55.

[96] X. Chen, Modelling and simulation of fibrous yarn materials, in: J. Hu (Ed.), Comput. Technol. Text. Appar., 2011: pp. 93–121.

[97] A. Rawal, S. Mukhopadhyay, Melt spinning of synthetic polymeric filaments, in: D. Zhang (Ed.), Adv. Filam. Yarn Spinn. Text. Polym., Woodhead Publishing Ltd, 2014: pp. 75–99.

[98] R.D. Goswami, Bhuvenesh C. Anandjiwala, D. Hall, Textile Sizing, Marcel Dekker, 2004.

[99] B.L. Deopura, A. Chatterjee, N.V. Padaki, Process control in the manufacturing of synthetic textile fibers, in: A. Majumdar, A. Das, R. Alagirusamy, V.K. Kothari (Eds.), Process Control Text. Manuf., Woodhead Publishing Ltd, 2013.

[100] A.V. Shenoy, Rheology of Filled Polymer Systems, Springer Science & Business Media, 1999.

[101] R.K. Gupta, S.N. Bhattacharya, THE EFFECT OF DIE GEOMETRIES AND EXTRUSION RATES ON MELT STRENGTH OF HIGH MELT STRENGTH POLYPROPYLENE, J. Polym. Eng. 27 (2007) 89–106.

[102] P.F. Antonietti, N.A. Fadel, M. Verani, Modelling and numerical simulation of the polymeric extrusion process in textile products, Commun. Appl. Ind. Math. 1 (2011) 1–13.

[103] H. Wook Jung, J. Chun Hyun, INSTABILITIES IN EXTENSIONAL DEFORMATION POLYMER PROCESSING, Rheol. Rev. (2006) 131–164.

[104] J. Down, Design and Technology: Textiles Technology Through Diagrams, Oxford University Press, 2001.

[105] M. Araújo, Natural and man-made fibres: Physical and mechanical properties, in: R. Fangueiro (Ed.), Fibrous Compos. Mater. Civ. Eng. Appl., Woodhead Publishing Ltd, 2011: pp. 3–28.

[106] J.W. Nicholson, The chemistry of polymers, RSC Pub, 2012.

[107] A.K.R. Choudhury, Textile preparation and dyeing, Science Publishers, 2006.

[108] A. Haji, R.S. Rahbar, B. Kalantari, The effect of hot multistage drawing on molecular structure and optical properties of polyethylene terephthalate fibers, Mater. Res. 15 (2012) 554–560.

[109] W.E. Morton, J.W.S. Hearle, Physical properties of textile fibres, 4th Ed., Woodhead Publishing Ltd, 2008.

[110] J.W.S. Hearle, Fibre structure: its formation and relation to performance, in: S. Eichhorn, J.W.S. Hearle, M. Jaffe, T. Kikutani (Eds.), Handb. Text. Fibre Struct., Woodhead Publishing Ltd, 2009: pp. 3–21.

[111] M. Biron, Material selection for thermoplastic parts : practical and advanced information for plastics engineers, Elsevier, 2016.

[112] N. Peng, N. Widjojo, P. Sukitpaneenit, M.M. Teoh, G.G. Lipscomb, T.-S. Chung, et al., Evolution of polymeric hollow fibers as sustainable technologies: Past, present, and future, Prog. Polym. Sci. 37 (2012) 1401–1424.

[113] T.H. Oh, M.S. Lee, S.Y. Kim, H.J. Shim, Studies on Melt-Spinning Process of Hollow Fibers, J. Appl. Polym. Sci. 68 (1998) 1209–1217.

[114] S. Omeroglu, E. Karaca, B. Becerir, Comparison of Bending, Drapability and Crease Recovery Behaviors of Woven Fabrics Produced from Polyester Fibers Having Different Cross-sectional Shapes, Text. Res. J. 80 (2010) 1180–1190.

[115] Y. Su, Theoretical studies of hollow fiber spinning, PhD Thesis, The University of Toledo, 2007.

[116] C. Prahsarn, N. Roungpaisan, W. Klinsukhon, N. Srisawat, Study on melt spinning of shaped hollow polypropylene fibers, Int. Polym. Process. 26 (2011) 30–39.

[117] A. De Rovere, B.P. Grady, R.L. Shambaugh, The influence of processing parameters on the properties of melt-spun polypropylene hollow fibers, J. Appl. Polym. Sci. 83 (2002) 1759–1772.

[118] Vishnu T. Marla, Robert L. Shambaugh, D. V. Papavassiliou, Modeling the Melt Blowing of Hollow Fibers, Ind. Eng. Chem. Res. 45 (2006) 407–415.

[119] H.F. Giles Jr, J.R. Wagner Jr, E.M. Mount, Extrusion: The Definitive Processing Guide and Handbook, 2nd Ed., Elsevier, 2014.

[120] A.F. Richards, Nylon fibres, in: J.. McIntyre (Ed.), Synth. Fibres Nylon, Polyester, Acrylic, Polyolefin, Woodhead Publishing Ltd, 2005: pp. 20–94.

[121] C. Maier, T. Calafut, Polypropylene: The Definitive User's Guide and Databook, CRC Press, 1998.

[122] R.R. Mather, Polyolefin fibres, in: J.E. McIntyre (Ed.), Synth. Fibres Nylon, Polyester, Acrylic, Polyolefin, Woodhead Publishing Limited, 2005: pp. 235–292.

[123] S. Kalpakjian, S.R. Schmid, Manufacturing Processes for Engineering Materials, 5th Ed., Pearson Education, 2008.

[124] A.J. East, Polyester fibres, in: J.E. McIntyre (Ed.), Synth. Fibres Nylon, Polyester, Acrylic, Polyolefin, Woodhead Publishing Ltd, 2005: pp. 95–166.

[125] S.-P. Rwei, Formation of hollow fibers in the melt-spinning process, J. Appl. Polym. Sci. 82 (2001) 2896–2902.

[126] Z.M. Huang, Y.Z. Zhang, M. Kotaki, S. Ramakrishna, A review on polymer nanofibers by electrospinning and their applications in nanocomposites, Compos. Sci. Technol. 63 (2003) 2223–2253.

[127] N. Khan, Applications of electrospun nanofibers in the biomedical field, Stud. by Undergrad. Res. Guelph. 5 (2012) 63–73.

[128] B. Caratão, Desenvolvimento e fabrico de estruturas para aplicações biomédicas por electrospinning, Dissertação de mestrado, Universidade do minho, 2014.

[129] NP EN ISO 2060: 1996 - Determinação da massa linear (massa por unidade de comprimento). Método da meada, (1996).

[130] C.A. Lawrence, Fundamentals of spun yarn technology, CRC Press, 2003.

[131] R. Fangueiro, Optimização do desenvolvimento de preformas em malha de trama para materiais compósitos, PhD Thesis, Universidade do Minho, 2002.

[132] V. Carvalho, R.M. Vasconcelos, F.O. Soares, M. Belsley, Yarn Diameter and Linear Mass Correlation, J. Nondestruct. Eval. 28 (2009) 49–54.

[133] S.M. Ishtiaque, A. Das, A new approach of prediction of yarn diameter, Fibers Polym. 14 (2013) 838–843.

[134] B.K. Parveen, Wicking behaviour of fibres, yarns and fabrics, PhD thesis, Mother Teresa Womens University, 2013.

[135] S. Subashini, Characteristics of Spun Silk Fabrics Produced From Hollow Yarns, Anna University, 2008.

[136] Zulkifli Mohamad Ariff, Azlan Ariffin, Suzi Salwah Jikan, Nor Azura Abdul Rahim, Rheological Behaviour of Polypropylene Through Extrusion and Capillary Rheometry, in: F. Dogan (Ed.), Polypropylene, InTech, 2012: pp. 29–48.

[137] T. FitzGibbon, Z. Nestorovski, Human intraretinal myelination: axon diameters and axon/myelin thickness ratios, Indian J. Ophthalmol. 61 (2013) 567–75.

[138] D. Petrulis, Fundamental study of the effect of the fiber wall thickness and inner diameter on the structure of polyamide and polypropylene hollow fibers, J. Appl. Polym. Sci. 92 (2004) 2017–2022.

[139] R.R. Ogle, M.J. Fox, Atlas of human hair microscopic characteristics, CRC Press, 1999.

[140] M.C. Murphy, J. Huston, C.R. Jack, K.J. Glaser, M.L. Senjem, J. Chen, et al., Measuring the characteristic topography of brain stiffness with magnetic resonance elastography, PLoS One. 8 (2013) 1–14.

[141] C. Rua, Analysis in Magnetic Resonance Elastography: Study and Development of Image Processing Techniques, Dissertação de mestrado, Universidade de Lisboa, 2012.

[142] R. Muthupillai, D.J. Lomas, P.J. Rossman, J.F. Greenleaf, A. Manduca, R.L. Ehman, Magnetic resonance elastography by direct visualization of propagating acoustic strain waves, Science (80-.). 269 (1995) 1854–7.

[143] S. Kruse, G. Rose, K. Glaser, A. Manduca, J. Felmlee, C.J. Jack, et al., Magnetic resonance elastography of the brain, Neuroimage. 39 (2008) 231–7.

[144] Y.K. Mariappan, K.J. Glaser, R.L. Ehman, Magnetic resonance elastography: a review, Clin. Anat. 23 (2010) 497–511.

[145] S.K. Venkatesh, M. Yin, R.L. Ehman, Magnetic resonance elastography of liver: technique, analysis, and clinical applications, J. Magn. Reson. Imaging. 37 (2013) 544–55.

[146] E. Clayton, Magnetic Resonance Elastography of the Brain: from Phantom to Mouse to Man, PhD thesis, Washington University in St. Louis, 2012.

[147] E.C. Qin, R. Sinkus, G. Geng, S. Cheng, M. Green, C.D. Rae, et al., Combining MR elastography and diffusion tensor imaging for the assessment of anisotropic mechanical properties: A phantom study, J. Magn. Reson. Imaging. 37 (2013) 217–226.

[148] E.C. Qin, R. Sinkus, C. Rae, L.E. Bilston, Investigating anisotropic elasticity using MR-Elastography combined with Diffusion Tensor Imaging: Validation using anisotropic and viscoelastic phantoms, in: Proc. Intl. Soc. Mag. Reson. Med. 19, 2011: p. 39.

[149] A. Perwuelz, M. Casetta, C. Caze, Liquid organisation during capillary rise in yarns—influence of yarn torsion, Polym. Test. 20 (2001) 553–561.

[150] M.K. Ozturk, B. Nergis, C. Candan, A study of wicking properties of cotton-acrylic yarns and knitted fabrics, Text. Res. J. 81 (2011) 324–328.

[151] X. Chen, K.G. Kornev, Y.K. Kamath, A. V. Neimark, The Wicking Kinetics of Liquid Droplets into Yarns, Text. Res. J. 71 (2001) 862–869.

[152] N. Wang, A. Zha, J. Wang, Study on the wicking property of polyester filament yarns, Fibers Polym. 9 (2008) 97–100.

[153] M.D. Roy, S.K. Sinha, Performance of Wicking through Yarn and Fabric Made from Polyester Fibres of Different Cross-sections, Int. J. Text. Sci. 3 (2014) 44–50.

[154] S.A.H. Ravandi, R.H. Sanatgar, F. Dabirian, Wicking Phenomenon in Nanofiber-Coated Filament Yarns, J. Eng. Fiber. Fabr. 8 (2013) 10–18.

[155] C.-H. Zhu, M. Takatera, M. Takatera, Effect of Fabric Structure and Yarn on Capillary Liquid Flow within Fabrics, J. Fiber Bioeng. Informatics. 6 (2013) 205–215.

[156] A. Das, A. Jain, A. Pant, Study on the liquid flow behaviour of cotton wick, Fibers Polym. 9

(2008) 176–186.

[157] K.P. Banu, P.M. Tharani, V. Subramaniam, Wicking Behaviour of Viscose Staple Yarns Differing in Linear Densities, J. Environ. Nanotechnol. 2 (2013) 01–05.

[158] B. Das, A. Das, V.K. Kothari, R. Fangueiro, Development of mathematical model to predict vertical wicking behaviour. Part I: flow through yarn, J. Text. Inst. 102 (2011) 957–970.

[159] R. Fangueiro, P. Gonçalves, F. Soutinho, C. Freitas, Moisture Management Performance of Multifunctional Yarns Based on Wool Fibers, Indian J. Fibre Text. Res. 34 (2009) 315–320.

[160] D. Saihi, A. El-Achari, A. Ghenaim, Claude Cazé, Wettability of grafted poly(ethylene terephthalate) fibers, Polym. Test. 21 (2002) 615–618.

[161] S. Mhetre, EFFECT OF FABRIC STRUCTURE ON LIQUID TRANSPORT, INK JET DROP SPREADING AND PRINTING QUALITY, PhD Thesis, Georgia Institute of Technology, 2009.

[162] S. Sahin, P. Yayla, Effects of processing parameters on the mechanical properties of polypropylene random copolymer, Polym. Test. 24 (2005) 1012–1021.

[163] E. Richardson, G. Martin, P. Wyeth, Effects of heat on new and aged polyamide 6,6 textiles during pest eradication, Polym. Degrad. Stab. 107 (2014) 262–269.

[164] Q.F. Wei, R.R. Mather, A.F. Fotheringham, R.D. Yang, ESEM Study of Wetting of Untreated and Plasma Treated Polypropylene Fibers, J. Ind. Text. 32 (2002) 59–66.

[165] ASTM D 629 - Standard Test Methods for Quantitative Analysis of Textiles. Section 9: Moisture Content or Moisture Regain, (2015).

[166] ASTM D3108 / D3108M - 13 - Standard Test Method for Coefficient of Friction, Yarn to Solid Material, (2013).

[167] NP EN ISO 2062:1997 - Fios sob a forma de enrolamento - determinação da força de rotura e alongamento de rotura, (1997).

[168] L. Hes, J. Williams, Laboratory measurement of thermo-physiological comfort, in: G. Song (Ed.), Improv. Comf. Cloth., Woodhead Publishing Ltd., 2011: pp. 114–137.

[169] A. Das, V.K. Kothari, S. Makhija, Development of a High-Absorbent Sanitary Napkin, in: S. Anand, J. Kennedy, M. M, S. Rajendran (Eds.), Med. Healthc. Text., Woodhead Publishing Ltd., 2010: pp. 148–155.

[170] S. Komaragounder, Comparison of Biological Activity Transistion Metal 12 Hydroxy oleate on Photodegradation of Plastics, J. Bioremediation Biodegrad. 1 (2010) 1–8.

[171] S. S. Bhattacharya & S. B. Chaudhari, Study on Structural and Thermal Properties of Polypropylene Silica Nanocomposite Filaments, Int. J. Text. Fash. Technol. 5 (2015) 15–22.

[172] J. Charles, G.R. Ramkumaar, S. Azhagiri, S. Gunasekaran, FTIR and Thermal Studies on Nylon-66 and 30% Glass Fibre Reinforced Nylon-66, E-Journal Chem. 6 (2009) 23–33.

[173] H.A. Mahdi, An FTIR Study of Characterization of Neat and UV Stabilized Nylon 6,6 Polymer Films, J. Pure Appl. Sci. 24 (2011) 86–90.

[174] S. Bandla, M. Allahkarami, J.C. Hanan, Thermal Cristallinity and Mechanical Behavior of Polyethylene Terephthalate, in: H. Jerry Qi, Bonnie Antoun, Richard Hall, Hongbing Lu, Alex Arzoumanidis, Meredith Silberstein, et al. (Eds.), Challenges Mech. Time-Dependent Mater. Vol. 2 Proc. Soc. Exp. Mech. Ser., Springer, 2015: pp. 141–146.

[175] R.R. Mather, R.H. Wardman, The chemistry of textile fibres, 2nd Ed., The Royal Society of Chemistry, 2015.

[176] Y. Seki, A. Akşit, U.H. Erdoğan, Construction of polypropylene composite multifilaments filled with sodium perborate trihydrate-treated jute microparticles, Sci. Eng. Compos. Mater. (2015) 1–10.

[177] B. Popovic, R. Jovanovic, E. Dzunuzovic, I. Popovic, D. Jocic, Structural Changes in the Fabrication and Ageing of PA66 Textured Yarn, Macromol. Mater. Eng. 290 (2005) 143–148.

[178] Y. Yuan, T.R. Lee, Contact Angle and Wetting Properties, in: G. Bracco, B. Holst (Eds.), Surf. Sci. Tech., Volume 51, Springer, 2013.

[179] M. Broudin, V. Le Saux, P.Y. Le Gac, C. Champy, G. Robert, P. Charrier, et al., Moisture sorption in polyamide 6.6: Experimental investigation and comparison to four physical-

based models, Polym. Test. 43 (2015) 10–20.

[180] C. Guise, R. Fangueiro, J.M. Nóbrega, W. Schneider, Study on fibrous materials for brain phantoms, Stud. Health Technol. Inform. 207 (2014) 163–72.

[181] M. Wishman, G.E. Hagler, Polypropylene Fibers, in: M. Lewin, E. Pearce (Eds.), Handb. Fiber Chem., 2nd Ed., CRC Press, 1998: pp. 161–278.

[182] A. V. Galanti, C.L. Mantell, Polypropylene Fibers and Films, Springer, Boston, MA, 1965.

[183] I.B. Page, Polyamides as Engineering Thermoplastic Materials, RAPRA Technology Ltd., 2000.

[184] S.K. Mukhopadhyay, Manufacturing, properties and tensile failure of nylon fibres, in: A.R. Bunsell (Ed.), Handb. Tensile Prop. Text. Tech. Fibres, Woodhead Publishing Ltd., 2009: pp. 197–222.

[185] B.S. Gupta, Friction in textile materials, CRC Press, Woodhead Publishing Limited, 2008.

[186] S. Adanur, Hanbook of Weaving, CRC Press, 2000.

[187] C. Stern, On the performance of polypropylene : between synthesis and end-use properties, PhD thesis, University of Twente, 2005.

[188] S. Mukhopadhyay, B.L. Deopura, R. Alagirusamy, Drawing of polypropylene filaments on a gradient heater, J. Text. Inst. 96 (2005) 349–354.

[189] A. Vitkauskas, R. Miglinaitė, P. Vesa, A. Puolakka, Mechanical Properties of Polypropylene Multifilament Yarns in Dependence of their Drawing Ratio, Mater. Sci. 11 (2005) 407–410.

[190] K.O. Fashola, A. Giwa, E.B. Iliya, J.G. Onemano, Studies on the Properties of Some Selected Polyester Textured Yarns, Middle-East J. Sci. Res. 11 (2012) 498–502.

[191] V.K. Kothari, Testing of manufactured fibres, in: V.B. Gupta, V.K. Kothari (Eds.), Manuf. Fibre Technol., 1st Ed., Springer Science & Business Media, 1997: pp. 248–270.

[192] S. Doakhan, A. Ravandi, S. Abdolkarim Hosseini Gharehaghaji, S.M. Mortazavi, Capillary Rise in Core-spun Yarn, Iran. Polym. J. 16 (2007) 397–408.

[193] U.P. Shinde, S.S. Chougule, C.G. Dighavkar, B.S. Jagadale, D.K. Halwar, Surface Tension as a Function of Temperature and Concentration of Liquids, Int. J. Chem. Phys. Sci. 4 (2015) 1–7.

[194] D.B. Pettigrew, K.A. Crutcher, Myelin contributes to the parallel orientation of axonal growth on white matter in vitro, BMC Neurosci. 2 (2001) Article: 9.

[195] P. Potluri, S. Nawaz, Developments in braided fabrics, in: R.H. Gong (Ed.), Spec. Yarn Fabr. Struct., Woodhead Publishing Ltd., 2011: pp. 333–353.

[196] R. Alagirusamy, N.V. Padaki, Introduction to Braiding, in: S. Rana, R. Fangueiro (Eds.), Braided Struct. Compos. Prod. Prop. Mech. Tech. Appl., CRC Press, 2016.

[197] R. Fangueiro, F.E.M. Cunha, G. Vasconcelos, S. Abreu, A brief overview on the retrofitting possibilities of masonry infill walls, Int. Conf. Eng. – ICEUB2011. (2011).

[198] F. Cunha, Desenvolvimento de uma estrutura com materiais fibrosos para ser utilizada como reforço em paredes de alvenaria, Dissertação de mestrado, Universidade do Minho, 2012.

[199] C. Gonilho Pereira, R. Fangueiro, S. Jalali, M. Araújo, P. Pina Marques, Tensile Performance of Braided Composite Rods for Concrete Reinforcement, Challenges Civ. Constr. (2008) 1–11. Torres Marques et al. (Eds).

[200] A. Martins, Soluções de Reforço Sísmico de Paredes de Alvenaria de Enchimento, Dissertação de mestrado, Universidade do Minho, 2013.

[201] V. V. Choogin, P. Bandara, E. V. Chepelyuk, Introduction: classification and mechanisms of weaving machines, in: V. V. Choogin, P. Bandara, E. V. Chepelyuk (Eds.), Mech. Flat Weav. Technol., Woodhead Publishing Ltd., 2013: pp. 1–18.

[202] G.J. da Silva, Design 3D em tecelagem jacquard como ferramenta para a concepção de novos produtos : aplicação em acessórios de moda, Dissertação de mestrado, Universidade do Minho, 2005.

[203] B. Behera, P. Hari, The basics of woven fabric structure, in: B. Behera, P. Hari (Eds.), Woven Text. Struct. Theory Appl., Woodhead Publishing Ltd, 2010.

[204] J. Wilson, Handbook of Textile Design: Principles, Processes, and Practice, CRC Press, 2001.

[205] V. Mecnika, K. Scheulen, C.F. Anderson, M. Hörr, C. Breckenfelder, Joining technologies for electronic textiles, in: T. Dias (Ed.), Electron. Text. Smart Fabr. Wearable Technol., Woodhead Publishing Ltd., 2015: pp. 133–153.

[206] J. Eichhoff, A. Hehl, S. Jockenhoevel, T. Gries, Textile fabrication technologies for embedding electronic functions into fibres, yarns and fabrics, in: T. Kirstein (Ed.), Multidiscip. Know-How Smart-Textiles Dev., Woodhead Publishing Ltd., 2013: pp. 191–226.

[207] R. Rebelo, N. Vila, R. Fangueiro, S. Carvalho, S. Rana, Influence of design parameters on the mechanical behavior and porosity of braided fibrous stents, Mater. Des. 86 (2015) 237–247.

[208] NP EN 1049-2: 1995 - Tecidos: Construção-Métodos de análise. Parte 2: Determinação do número de fios por unidade de comprimento, (1995).

[209] J. Hayavadana, Woven Fabric Structure Design and Product Planning, Woodhead Publishing India Ltd, 2015.

[210] ASTM D 3776-96 : Standard Test Method for Mass Per Unit Area (Weight) of Fabric, (2002).

[211] P.K. Hari, Types and properties of fibres and yarns used in weaving, in: K.L. Gandhi (Ed.), Woven Text. Princ. Technol. Appl., Woodhead Publishing Limited, 2012: pp. 3–34.

[212] M. Akgun, B. Becerir, H.R. Alpay, Assessing the relationship among fabric constructional parameters, fractional reflectances and cover factors of polyester fabrics by experimental and mathematical methods, Fibers Polym. 11 (2010) 291–302.

[213] NP EN ISO 5084: 1996 - Determinação da espessura de têxteis e produtos têxteis, (1999).

[214] NP EN ISO 13934-1: 2001 - Propriedades de tração dos tecidos. Parte 1: Determinação da força máxima e do alongamento à força máxima pelo método da tira, (2001).

[215] J. Cruz, S. Rana, R. Fangueiro, R. Guedes, Designing artificial anterior cruciate ligaments based on novel fibrous structures, Fibers Polym. 15 (2014) 181–186.

[216] Z. Zupin, K. Dimitrovski, Mechanical Properties of Fabrics Made from Cotton and Biodegradable Yarns Bamboo, SPF, PLA in Weft, in: Woven Fabr. Eng., Sciyo, 2010: pp. 25–46.

[217] B. Das, A. Das, V.K. Kothari, R. Fangueiro, Mathematical model to predict vertical wicking behaviour. Part II: flow through woven fabric, J. Text. Inst. 102 (2011) 971–981.

[218] T. Sharabaty, F. Biguenet, D. Dupuis, P. Viallier, Investigation on moisture transport through polyester/cotton fabrics, Indian J. Fibre Text. Res. 33 (2008) 419–425.

[219] P. Zuccolotto, Anthony, K. Basler, Leroy, J. Dzikiy, W. Schneider, A. Shaffer, Richard, Universal, modular temperature controlled MRI phantom for calibrated anisotropic and isotropic Imaging including hollow fluid filled tubular textiles for calibrated anisotropic imaging, WO/2016/007939, 2016.

[220] S.K. Pathak, IMPROVED QUANTIFICATION OF CONNECTIVITY IN HUMAN BRAIN MAPPING, PhD Thesis, University of Pittsburgh, 2015.

[221] E.Y. Kim, H.-J. Park, D.-H. Kim, S.-K. Lee, J. Kim, Measuring fractional anisotropy of the corpus callosum using diffusion tensor imaging: mid-sagittal versus axial imaging planes., Korean J. Radiol. 9 (2008) 391–5.

[222] S. Richardson, B. Siow, A.M. Batchelor, M.F. Lythgoe, D.C. Alexander, A viable isolated tissue system: a tool for detailed MR measurements and controlled perturbation in physiologically stable tissue, Magn. Reson. Med. 69 (2013) 1603–10.

Publications and Communications

1) Publications

Guise, C., Fernandes, M.M., Nóbrega, J.M., Sudhir, P., Schneider, W., Fangueiro, R. (2016). "Hollow polypropylene yarns as a biomimetic brain phantom for the validation of High-Definition Fiber Tractography imaging" ACS Applied Materials & Interfaces DOI: 10.1021/acsami.6b09809

Guise, C., Fangueiro, R., Nóbrega, J.M, Schneider, W. (2014). "Study on fibrous materials for brain phantoms" In: Studies in health technology and informatics. Vol. 207. ISBN 978-1-61499-473-2.

Guise, C., Fernandes, M.M., Nóbrega, J.M., Schneider, W., Fangueiro, R. "A novel approach for brain phantom development based on fibrous materials: a study of mechanical properties" (to be submitted)

Guise, C., Fernandes, M.M., Nóbrega, J.M., Schneider, W., Fangueiro, R. "A review on brain phantoms: materials and design" (to be submitted)

Guise, C., Sampaio, S., Parveen, S., Cruz, J., Fernandes, M.M., Rana, S., Fangueiro, R. "Electrospun nanofibres-based materials for advanced applications: a review" (to be submitted)

2) Communications

Guise, C., Fangueiro, R., Schneider, W., Nóbrega, J.M. (2015). "Assessing the application of polypropylene multifilament yarns in brain phantoms" Proceedings in VII International Materiais Symposium. Faculdade de Engenharia da Universidade do Porto, Portugal.

Guise, C., Fangueiro, R., Schneider, W., Nóbrega, J.M. (2015). "Estudo de materiais fibrosos para aplicação em modelos cerebrais" 6º Congresso Nacional de Biomecânica.

Guise, C., Fangueiro, R., Nóbrega, J.M., Schneider, W. (2014). "Study on fibrous materials for brain phantoms" KES International Conference on Innovation in Medicine and Healthcare, San Sebastian, Spain.